

Carbon Sequestration Technology

DOE Award No.: DE-FE0002041

Final Report

Modeling and Risk Assessment of CO₂ Sequestration at the Geologic-basin Scale

Submitted by:
Massachusetts Institute of Technology
77 Massachusetts Ave, Bldg. 48-319
Cambridge, MA 02139

Prepared by:
Prof. Ruben Juanes
Tel: (617)253-7191
Email: juanes@mit.edu

Prepared for:
United States Department of Energy
National Energy Technology Laboratory

November 30, 2013



Office of Fossil Energy

Disclaimer - This report was prepared as an account of work sponsored by an agency of the United States Government. Neither the United States Government nor any agency thereof, nor any of their employees, makes any warranty, express or implied, or assumes any legal liability or responsibility for the accuracy, completeness, or usefulness of any information, apparatus, product, or process disclosed, or represents that its use would not infringe privately owned rights. Reference herein to any specific commercial product, process, or service by trade name, trademark, manufacturer, or otherwise does not necessarily constitute or imply its endorsement, recommendation, or favoring by the United States Government or any agency thereof. The views and opinions of authors expressed herein do not necessarily state or reflect those of the United States Government or any agency thereof.

Contents

1	Executive summary	2
2	Mathematical models of CO₂ migration at the basin scale	3
2.1	Model of pressure evolution	3
2.2	Model of capillary trapping	9
2.3	Model of capillary and solubility trapping	14
3	Application of mathematical models to basins in the continental United States	37
3.1	Methodology for application of the models	37
3.2	Aquifer data	41
4	Estimation of CO₂ storage capacity and injectivity	82
4.1	Sensitivity analysis on model parameters	82
4.2	Probability distributions for parameters with greatest impact	85
4.3	Uncertainty analysis	87
4.4	Synopsis of aquifer data and storage capacities	94
5	Technology transfer activities	96
5.1	Peer-reviewed journal publications	96
5.2	Conference contributions	97
5.3	Talks, seminars and presentations	98
5.4	Educational activities and outreach	99
5.5	Scientific collaborations	100
5.6	Editor/reviewer tasks	100
	References	101

1 Executive summary

Objectives. The overall objective of this proposal was to develop tools for better understanding, modeling and risk assessment of CO₂ permanence in geologic formations at the geologic basin scale. The main motivation was that carbon capture and storage (CCS) will play an important role as a climate change mitigation technology only if it is deployed at scale of gigatonne per year injections over a period of decades. Continuous injection of this magnitude must be understood at the scale of a geologic basin. Specifically, the technical objectives of this project were: (1) to develop mathematical models of capacity and injectivity at the basin scale; (2) to apply quantitative risk assessment methodologies that will inform on CO₂ permanence; (3) to apply the models to geologic basins across the continental United States.

These technical objectives go hand-in-hand with the overarching goals of: (1) advancing the science for deployment of CCS at scale; and (2) contributing to training the next generation of scientists and engineers that will implement and deploy CCS in the United States and elsewhere.

Methods. The differentiating factor of this proposal was to perform fundamental research on migration and fate of CO₂ and displaced brine at the *geologic basin scale*. We developed *analytical* sharp-interface models of the evolution of CO₂ plumes over the duration of injection (decades) and after injection (centuries). We applied the analytical solutions of CO₂ plume migration and pressure evolution to specific geologic basins, to estimate the maximum footprint of the plume, and the maximum injection rate that can be sustained during a certain injection period without fracturing the caprock. These results have led to more accurate capacity estimates, based on fluid flow dynamics, rather than ad hoc assumptions of an overall “efficiency factor.” We also applied risk assessment methodologies to evaluate the uncertainty in our predictions of storage capacity and leakage rates. This was possible because the analytical mathematical models provide ultrafast forward simulation and they contain few parameters.

Impact. The project has been enormously successful both in terms of its scientific output (journal publications) as well as impact in the government and industry. The mathematical models and uncertainty quantification methodologies developed here offer a physically-based approach for estimating capacity and leakage risk at the basin scale. Our approach may also facilitate deployment of CCS by providing the basis for a simpler and more coherent regulatory structure than an “individual-point-of-injection” permitting approach. It may also lead to better science-based policy for post-closure design and transfer of responsibility to the State.

2 Mathematical models of CO₂ migration at the basin scale

2.1 Model of pressure evolution

We developed a new model to calculate storage capacity under pressure limitations because existing models apply to geologic settings that are not appropriate for our study. For example, one such model calculates pressure-limited storage capacity in aquifers that are bounded laterally by impermeable boundaries [Zhou et al., 2008b; Ehlig-Economides and Economides, 2010]. This model is inappropriate for our study because we consider mostly open aquifers, since they will have larger storage capacities and will therefore contribute more strongly to the nationwide capacity estimate. Another available model calculates the pressure-limited capacity in an open aquifer, but this model applies to a single injection well [van der Meer and Egberts, 2008]. To simply calculate the pressure-limited capacity at the basin scale, we consider injection from a line-drive array of wells, as in the trapping model.

Mathematical model

We have previously derived a one-dimensional version of our pressure model [Szulczewski et al., 2010b]. Here, we extend the model to two dimensions. All variables in the model are defined in Table 1. The major assumptions in the model are:

1. We assume that the vertical stress in an aquifer is constant.
2. We assume that the boundaries of the aquifer do not undergo lateral strain.
3. We assume that the aquifer, the overburden, and the underburden are homogeneous.
4. We assume that the initial pressure is hydrostatic.
5. We assume that the aquifer properties and fluid properties are constant.
6. We assume that the pressure distribution along the line-drive array of wells is uniform.

The geologic setting of our system is the same as the setting of the trapping model, but now includes the entire thickness of the basin that contains the target aquifer, as shown in Figure 1. In this system, the model for pressure, p , as a function of spatial coordinates x and z and time, t , can be derived starting from conservation of mass:

$$c\partial_t p + \partial_x u_x + \partial_z u_z = I(z), \quad (1)$$

where c is the compressibility, I is a function that represents injection into the aquifer, and u_x and u_z are the Darcy velocities in the x and z directions, respectively. In this system, Darcy's law for single-phase flow is:

$$u_x = -\frac{k_x(z)}{\mu_w} \partial_x p, \quad u_z = -\frac{k_z(z)}{\mu_w} (\partial_z p - \rho_w g), \quad (2)$$

where k_x and k_z are given by:

$$k_x(z) = \begin{cases} k_{aq} & D \leq z < D + H, \\ \overline{k_x} = k_{aq}/2 & \text{otherwise,} \end{cases}$$

$$k_z(z) = \begin{cases} k_{aq} & D \leq z < D + H, \\ \overline{k_z} = 2k_{cap} & \text{otherwise.} \end{cases}$$

These expressions are conditional because we assign different properties to the aquifer and the regions outside of the aquifer. Within the aquifer, the intrinsic permeability is k_{aq} . Above and below the aquifer, we set the permeability to average values ($\overline{k_x}$ and $\overline{k_z}$) derived from the aquifer permeability and the caprock permeability, k_{cap} , as shown in Figure 2. The source term I is conditional since it accounts for a ramping-up of the injection rate, a ramping-down of the injection rate, and then no injection:

$$I(z, t) = \begin{cases} \delta(x)\mathcal{U}(z; D, D + H) \frac{2Q_{max}}{WH} \frac{t}{T_i} & 0 \leq t < T_i/2, \\ \delta(x)\mathcal{U}(z; D, D + H) \frac{2Q_{max}}{WH} \left(1 - \frac{t}{T_i}\right) & T_i/2 \leq t < T_i, \\ 0 & T_i \leq t, \end{cases}$$

where T_i is the injection time (Figure from main paper) and \mathcal{U} is the rectangular function, which allows injection only within the aquifer:

$$\mathcal{U}(z) = \begin{cases} 1 & D \leq z < D + H, \\ 0 & \text{otherwise.} \end{cases}$$

With these expressions, the model for pressure becomes:

$$c\partial_t p - \frac{k_x(z)}{\mu_w} \partial_{xx} p - \partial_z \left(\frac{k_z(z)}{\mu_w} (\partial_z p - \rho_w g) \right) = I(z, t) \quad (3)$$

$$X_l < x < X_r, \quad 0 < z < D + H + U, \quad t > 0. \quad (4)$$

The initial condition is hydrostatic pressure:

$$p(x, z, t = 0) = p_o + \rho_w g z, \quad (5)$$

where p_o is atmospheric pressure. The boundary condition at the top of the basin is a constant-pressure condition, and the boundary condition at the bottom of the basin is a no-flow condition:

$$p(x, z = 0, t) = p_o, \quad (6)$$

$$\partial_z p(x, z = D + H + U, t) = 0. \quad (7)$$

The boundary conditions at the sides of the basin may be either no-flow conditions or constant-pressure conditions depending on the geology. A no-flow condition on the left boundary would be written:

$$\partial_z p(x = X_l, z, t) = 0. \quad (8)$$

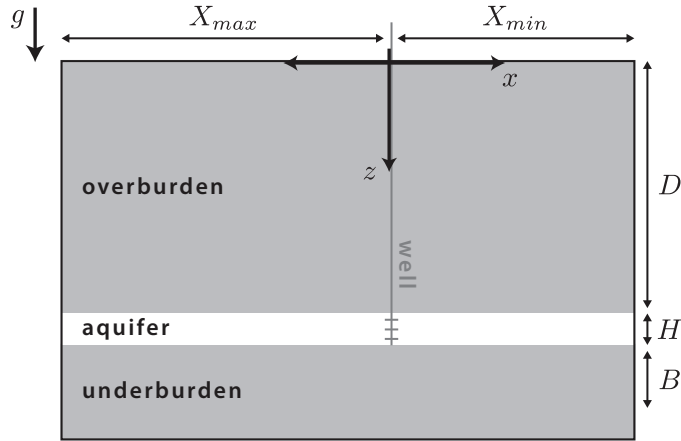


Figure 1: Since we consider injection from a line-drive array of wells, our pressure model is two dimensional: it captures behavior in a plane perpendicular to the line-drive array that extends from the ground surface to the basement. We position the center of the coordinate system where the line-drive array intersects the surface.

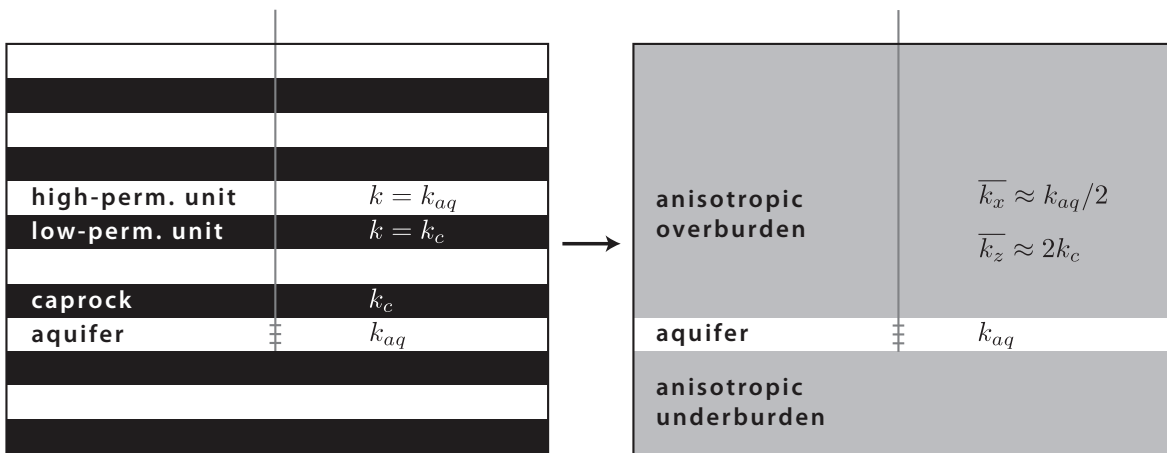


Figure 2: To model the entire thickness of a basin, we assume that it consists of multiple layers of high-permeability and low-permeability rock. We assume that each layer of high-permeability rock has the same permeability as the aquifer, and that each layer of low-permeability rock has the same permeability as the caprock. Under these assumptions, we average the permeabilities of all the layers above and below the aquifer to get homogeneous, but anisotropic permeabilities of the overburden and underburden.

A constant-pressure condition at the right boundary would be written:

$$p(x = X_r, z, t) = p_o + \rho_w g z. \quad (9)$$

For simplicity, we assume that the same boundary condition applies over an entire side of the basin.

Dimensionless form of the equations. We choose the following non-dimensional variables:

$$\tilde{p} = \frac{p - (p_o + \rho_w g z)}{\bar{P}}, \quad \tau = \frac{t}{T_i}, \quad \xi = \frac{x}{L}, \quad \zeta = \frac{z}{H}, \quad (10)$$

where T_i is the injection time. We define the characteristic pressure and the characteristic length in the x-direction as:

$$L = \sqrt{\frac{k_{aq} T_i}{\mu_w c}}, \quad \bar{P} = \frac{2Q_{max}}{HW} \sqrt{\frac{\mu_w T_i}{k_{aq} c}}.$$

The non-dimensional form of the pressure model is:

$$\partial_\tau \tilde{p} - \lambda_\xi(\zeta) \partial_{\xi\xi} \tilde{p} - \partial_\zeta (\lambda(\zeta) \partial_\zeta \tilde{p}) = \tilde{I}(\zeta), \quad (11)$$

$$\Xi_l < \xi < \Xi_r, \quad 0 < \zeta < 1 + \Omega + \beta, \quad \tau > 0,$$

where the dimensionless lengths in the basin are given by:

$$\Xi_l = \frac{X_l}{L}, \quad \Xi_r = \frac{X_r}{L}, \quad \Omega = \frac{D}{H}, \quad \beta = \frac{B}{H}.$$

λ_ξ and λ_ζ are dimensionless diffusion coefficients given by:

$$\lambda_\xi(\zeta) = \begin{cases} 1 & \Omega \leq \zeta < \Omega + 1, \\ 1/2 & \text{otherwise,} \end{cases}$$

and

$$\lambda_\zeta(\zeta) = \begin{cases} \frac{k_{aq} T_i}{\mu_w c H^2} & \Omega \leq \zeta < \Omega + 1, \\ \frac{2k_{cap} T_i}{\mu_w c H^2} & \text{otherwise.} \end{cases}$$

The dimensionless injection function is:

$$\tilde{I}(\zeta, \tau) = \begin{cases} \delta(\xi) \mathcal{U}(\zeta; \Omega, \Omega + 1) \tau & 0 \leq \tau < 1/2, \\ \delta(\xi) \mathcal{U}(\zeta; \Omega, \Omega + 1) (1 - \tau) & 1/2 \leq \tau < 1, \\ 0 & 1 \leq \tau. \end{cases}$$

Pressure-limited capacity

For a given injection period T_i , a particular injection scenario characterized by Q_{max} will lead to a particular maximum pressure in the aquifer. For small values of Q_{max} , the maximum pressure will be small, but for increasingly larger values the pressure will become larger, until at a particular Q_{max} the maximum pressure will reach the fracture pressure of the aquifer. We define the volume injected in this scenario to be the pressure-limited storage capacity. To calculate it, we first note that the volume injected is the area under the injection curve (Figure from main paper):

$$V_p = \frac{1}{2} Q_{max} T_i. \quad (12)$$

We determine the maximum injection rate Q_{max} by rearranging the expression for the non-dimensional pressure \tilde{p} (Eq. 10):

$$Q_{max} = HW \sqrt{\frac{k_{aq} c}{\mu_w T_i} \frac{p - (p_o + \rho_w g z)}{2\tilde{p}}}.$$

Now we set the pressure p to the fracture pressure P_{frac} and the dimensionless pressure \tilde{p} to the maximum dimensionless pressure \tilde{p}_{max} . Substituting into the equation for injection volume (Eq. 12) and multiplying by the density of CO₂ yields the storage capacity in terms of mass, \mathcal{C}_p :

$$\mathcal{C}_p = \rho_g HW \sqrt{\frac{k_{aq} c T_i}{\mu_w} \frac{P_{frac} - (p_o + \rho_w g z)}{4\tilde{p}_{max}}}. \quad (13)$$

We determine the maximum dimensionless pressure \tilde{p}_{max} by solving the pressure model (Eq. 11) numerically. We use the finite-volume method in space and the Crank-Nicolson method to solve the equation in time.

We define the fracture pressure, P_{frac} , to be the pressure required to create a tensile fracture in an aquifer. We calculate it using the effective stress principle,

$$\sigma' = \sigma_T - p,$$

where σ' is the effective stress, σ_T is the total stress, and p is the pore-fluid pressure Zoback [2007]. Ignoring the cohesive strength of the aquifer rock, a tensile fracture occurs when the least principle effective stress is zero. When this stress is vertical, we calculate it to be the weight of the overburden:

$$P_{frac} = \rho_o g D, \quad (14)$$

where ρ_o is the density of the overburden, which we approximate to be 2300 kg/m³. When it is horizontal, we approximate it by [Zoback, 2007, p.281]:

$$P_{frac} = \frac{\nu}{1 - \nu} \rho_o g D, \quad (15)$$

where ν is Poisson's ratio. We determine whether the least principle stress is horizontal or vertical by using a stress map for the United States Zoback and Zoback [1980b].

Table 1: The parameters used in our models and their symbols.

Parameter	Symbol
Residual CO ₂ saturation	S_{gr}
Connate water saturation	S_{wc}
Endpoint relative permeability to CO ₂	k_{gr}^*
Coefficient of CO ₂ -saturated-brine flux	α
Compressibility	c
Undrained Poisson ratio	ν
Geothermal gradient	G_T
Surface temperature	T_s
Depth to top of aquifer	D
Depth from aquifer to bedrock	B
Net aquifer thickness	H
Length of model domain	L_t
Width of well array	W
Porosity	ϕ
Caprock slope	ϑ
Darcy velocity	U
Aquifer permeability	k_{aq}
Caprock permeability	k_c
Lateral overburden permeability	$\overline{k_x}$
Vertical overburden permeability	$\overline{k_z}$
Salinity	s
CO ₂ solubility	χ_v
Brine density	ρ_w
CO ₂ density	ρ_g
CO ₂ -saturated-brine density	ρ_d
Brine viscosity	μ_w
CO ₂ viscosity	μ_g
Fracture Overpressure	P_{frac}

2.2 Model of capillary trapping

Development of the mathematical model

We are interested in large CO₂ storage projects, and therefore in the evolution of the CO₂ plume at the geologic-basin scale—a schematic of the basin scale geologic setting is shown in figure 3. We assume that the CO₂ is injected simultaneously through a linear arrangement of a large number of wells. The plumes from neighboring wells will merge as the radius of the plumes around wells approaches the inter-well spacing. We model the single resulting plume as two-dimensional in the x - z plane, with some width W in the y -direction equal to the length of the well array.

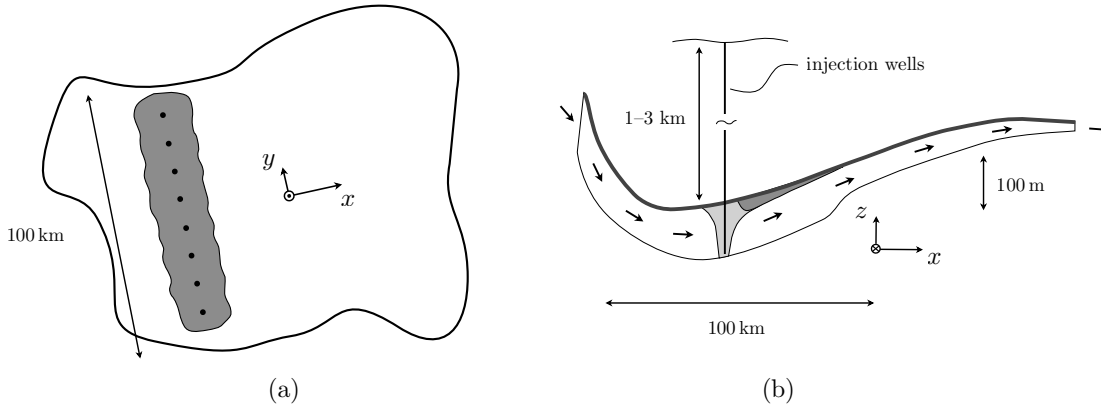


Figure 3: Injection of CO₂ into a saline aquifer at the basin scale. (a) In cross-section, the CO₂ is shown in gray, the groundwater in white, and the caprock as a thick line. Arrows indicate the direction of groundwater flow. Typical horizontal and vertical scales are indicated—note that the vertical scale of the aquifer is greatly exaggerated. (b) From a bird’s-eye view, the plumes from the individual wells merge together as the CO₂ spreads away from the well array (black dots).

We take the aquifer to be homogeneous, with an arbitrary tilt angle relative to the horizontal and a net groundwater flow to the right. We take the fluids to be incompressible and Newtonian, with constant and uniform properties within the aquifer. The fraction of pore space occupied by trapped or residual CO₂ after the bulk is displaced is the residual gas saturation, S_{gr} . Similarly, some fraction of pore space may be occupied by immobile groundwater; this is known as the connate water saturation, S_{wc} .

We employ a sharp-interface approximation, neglecting the width of typical gradients in saturation (*i.e.*, the capillary transition zone or “fringe”) compared to typical length scales in the horizontal and vertical directions, and we further neglect the capillary pressure compared to typical hydrostatic and viscous pressure drops [Bear, 1972; Yortsos, 1995]. We divide the domain into three regions of uniform CO₂ and groundwater saturation with sharp interfaces corresponding to saturation discontinuities. As illustrated in figure 4, Region 1 is the mobile plume of CO₂, containing mobile CO₂ with a saturation S_{wc} of connate groundwater; Region 2 is the region from which the plume has receded, containing mobile groundwater with a saturation S_{gr} of trapped CO₂; and Region 3 contains mobile groundwater with no CO₂.

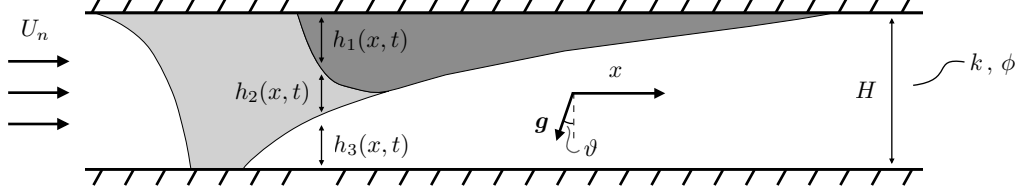


Figure 4: A schematic of the plume during post-injection migration, as the mobile CO_2 is pushed to the right by a combination of groundwater flow and aquifer slope, leaving trapped CO_2 in its wake. We divide the domain into three regions of uniform CO_2 and groundwater saturation, separated by sharp interfaces corresponding to saturation discontinuities. Region 1 (dark gray) has a saturation $1 - S_{wc}$ of mobile CO_2 with a saturation S_{wc} of connate groundwater; Region 2 (light gray) has a saturation S_{gr} of trapped CO_2 and a saturation $1 - S_{gr}$ of mobile groundwater; Region 3 (white) contains only groundwater. The aquifer has a total thickness H , and the thickness of Region i , $i = 1, 2, 3$, is denoted $h_i(x, t)$. Groundwater flows naturally through the aquifer from left to right with velocity U_n ; the aquifer has permeability k and porosity ϕ , as well as an arbitrary angle of tilt ϑ measured counterclockwise from the direction of gravity.

We make the Dupuit or “vertical equilibrium” approximation and neglect the vertical flow velocity compared to the horizontal flow velocity. This is justified when the characteristic vertical length scale is much smaller than the characteristic horizontal one, as is generally the case for aquifers.

The complete derivation of the model under these assumptions is given elsewhere [Hesse et al., 2008; MacMinn et al., 2010]. The plume migration equation, in dimensionless form, is:

$$\tilde{\mathcal{R}} \frac{\partial \eta}{\partial \tau} + N_f \frac{\partial f}{\partial \xi} + N_s \frac{\partial}{\partial \xi} \left[(1 - f)\eta \right] - N_g \frac{\partial}{\partial \xi} \left[(1 - f)\eta \frac{\partial \eta}{\partial \xi} \right] = 0, \quad (16)$$

where $\eta = h_1/H$ is the dimensionless plume height (normalized by the aquifer thickness H), $\tau = t/T_c$ is the dimensionless time (normalized by the duration of the injection period, $T_c = T_i$), and $\xi = x/L_c$ is the dimensionless distance (normalized by the characteristic length $L_c = Q_i T_i / 2(1 - S_{wc})\phi H$, where Q_i is the integrated volumetric injection flow rate [L^2T^{-1}]). The accumulation coefficient is discontinuous,

$$\tilde{\mathcal{R}} = \begin{cases} 1 & \text{if } \partial \eta / \partial \tau > 0, \\ 1 - \Gamma & \text{if } \partial \eta / \partial \tau < 0, \end{cases} \quad (17)$$

where $\Gamma = S_{gr}/(1 - S_{wc})$ is the capillary trapping number, which measures the fraction of CO_2 that is left behind at the trail of the plume. The fractional flow function is

$$f(\eta) = \frac{\mathcal{M}\eta}{\mathcal{M}\eta + (1 - \eta)}, \quad (18)$$

where $\mathcal{M} = \lambda_1/\lambda_3$ is the mobility ratio between Regions 1 and 3 (usually much larger than one, due to the high viscosity contrast between brine and CO_2 at reservoir conditions).

The flux terms in equation (16) have the following physical interpretations: the first is advective in nature, capturing the motion of the CO_2 due to groundwater flow through the

aquifer; the second is also advective, capturing the motion of the CO₂ due to the tilt of the aquifer; and the third is diffusive, capturing the upward spreading of the CO₂ against the caprock due to buoyancy. The constants N_f (flow number), N_s (slope number), and N_g (gravity number) are given by

$$N_f = \frac{T_c}{T_i} \frac{Q}{Q_i/2}, \quad N_s = \frac{T_c}{L_c} \kappa \sin \vartheta, \quad N_g = \frac{T_c}{L_c} \kappa \cos \vartheta \frac{H}{L_c}. \quad (19)$$

where $Q = U_n H$ is the integrated groundwater flow velocity [$L^2 T^{-1}$], $\kappa = \Delta \rho g k \lambda_1 / [(1 - S_{wc}) \phi]$ is the intrinsic velocity of buoyancy-driven flow, $\Delta \rho = \rho_w - \rho_g$ is the density difference between the groundwater and the CO₂, g is the force per unit mass due to gravity, and k and ϕ are the intrinsic permeability and porosity of the aquifer, respectively.

Without loss of generality, we choose $N_f \geq 0$ —thus groundwater flow is always *to the right* by convention. Aquifer slope can be either positive ($N_s > 0$) for counterclockwise aquifer tilt or negative ($N_s < 0$) for clockwise aquifer tilt.

Numerical simulations of equation (16) show that the essential features of the plume shape and migration are dominated by advective effects and capillary trapping, even for non-negligible values of N_g compared to N_f and N_s [Juanes and MacMinn, 2008; Hesse et al., 2008; Juanes et al., 2010; MacMinn et al., 2010]. Therefore, we neglect the spreading term, which leads to a first-order hyperbolic conservation law.

Summary of analytical results: storage efficiency

The hyperbolic model can be solved analytically for all combinations of groundwater flow and aquifer slope, accounting fully for the shape of the CO₂ plume at the end of the injection period [MacMinn and Juanes, 2009]. A detailed derivation of the analytical solution is given elsewhere [MacMinn et al., 2010]; here, we simply summarize the results.

We are primarily interested in the storage efficiency, that is, the volume of CO₂ stored per unit volume of aquifer “used.” [Bachu et al., 2007] We define the storage efficiency ε as

$$\varepsilon = \frac{V_{\text{CO}_2}}{V_T} = \frac{Q_i T_i}{H L_T (1 - S_{wc}) \phi}, \quad (20)$$

where V_{CO_2} is the volume of CO₂ injected and V_T is the total volume of aquifer used; we define V_T to be the total pore volume available for CO₂ storage in a rectangle of thickness H and length L_T , where L_T total extent in the x -direction of the fully trapped CO₂ [Juanes et al., 2010]. Taking $\xi_T = L_T/L_c$ and using L_c as defined above, we have that $\varepsilon = 2/\xi_T$. The storage efficiency takes a value between 0 and Γ , and is inversely proportional to the dimensionless plume footprint.

The storage efficiency can be readily evaluated from the solution to the migration equation as a function of N_s/N_f , \mathcal{M} , and Γ , and this can be done quickly and at high resolution over a large range of parameters owing to the analytical nature of the solution. In figure 5 below, we plot the storage efficiency as a function of N_s/N_f for a typical value $\mathcal{M} = 15$, and several values of Γ .

The storage efficiency always decreases with \mathcal{M} —this is because increasing \mathcal{M} strengthens the “tonguing” of the plume during both injection and post-injection migration. Similarly, the storage efficiency always increases with Γ —this is because more CO₂ is left behind

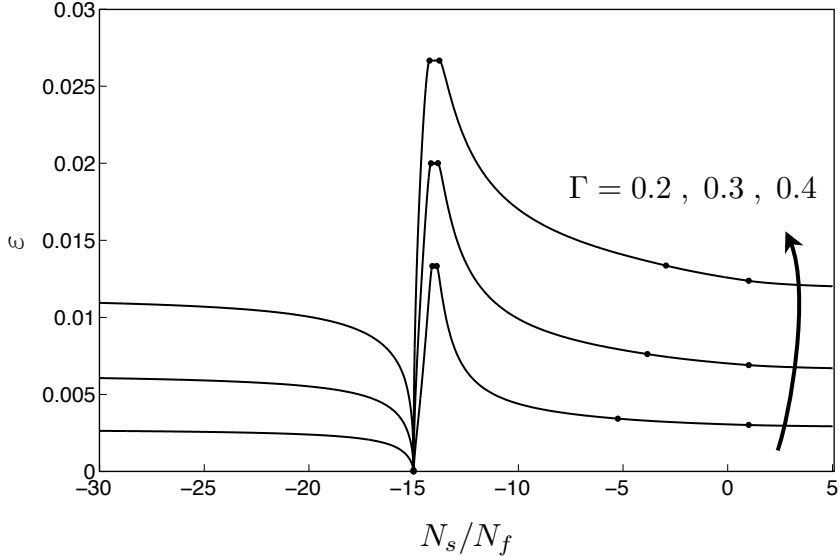


Figure 5: Storage efficiency, ε , as a function of N_s/N_f for several values of Γ , as indicated, at $\mathcal{M} = 15$.

upon imbibition, and so the plume becomes fully trapped over a shorter migration distance. Particularly relevant is the fact that the maximum efficiency (which can be obtained analytically and is equal to $\varepsilon_{\max} = \Gamma/\mathcal{M}$) is achieved for a large negative value of $N_s/N_f \approx -\mathcal{M} + 1$, that is, when slope dominates over groundwater flow, and the flow direction is down dip. This is a nontrivial result: figure 5 shows that while the storage efficiency is essentially the same for slope-only ($N_s/N_f = 0$) and flow-only ($N_s/N_f \rightarrow \pm\infty$), a gentle down-dip flow can provide a multiple-fold increase in storage efficiency, up to a factor $1/\Gamma$.

Conclusions

We have developed a complete solution to a hyperbolic gravity-current model for CO_2 migration in a saline aquifer due to groundwater flow and aquifer slope, subject to residual trapping and accounting for the tongued end-of-injection plume shape. We have shown how the solution changes with N_s/N_f , \mathcal{M} , and Γ , and also explored the effect of these parameters on the overall storage efficiency. While the main contribution of this model is the insight it provides into the physics of CO_2 migration and trapping, we illustrate in Juanes et al. [2010] and Szulczewski and Juanes [2009] how it can be used to develop basin-specific capacity estimates.

We find that the maximum storage efficiency is achieved for a relatively large negative value of the parameter N_s/N_f —that is, when there is a gentle down-dip groundwater flow. This is a nontrivial result: figure 5 shows that while the storage efficiency is essentially the same for the slope-only and flow-only cases, and when flow is up-dip, a gentle down-dip flow can provide a multiple-fold increase in storage efficiency. Hydrogeological conditions leading to this interplay between slope and groundwater flow are known to occur in many continental sedimentary basins [Garven, 1995].

While we have not included the effect of CO_2 dissolution here, it is well-known that

CO₂ is weakly soluble in groundwater, and therefore that both residual CO₂ and CO₂ from the mobile plume will dissolve slowly into the nearby groundwater as the plume migrates. Because the density of groundwater increases with dissolved CO₂ content, the boundary layer of CO₂-saturated groundwater near the mobile plume is unstable. This instability eventually results in so-called convective mixing, where plumes of dense, CO₂-saturated groundwater sink away from the interface as plumes of “fresh” groundwater rise upward. It has been shown that for a stationary plume of CO₂, convective mixing is triggered on time scales that are short relative to required storage times, and that it dramatically increases the rate of CO₂ dissolution compared to diffusive transport alone [Ennis-King and Paterson, 2005; Riaz et al., 2006b]. We expect that dissolution will have a non-negligible contribution to overall trapping. In future work, we will incorporate dissolution into the migration equation and study the importance of dissolution relative to capillary trapping and the impact of dissolution on the storage efficiency.

2.3 Model of capillary and solubility trapping

Introduction

In work reported in previous reports, we obtained a complete solution to a theoretical model for the subsurface migration of a plume of CO_2 due to natural groundwater flow and aquifer slope, and subject to residual trapping. Here, we consider the importance of CO_2 dissolution. We first incorporate dissolution into the migration model, and we then identify three regimes in migration with dissolution depending on how quickly the water beneath the plume saturates with dissolved CO_2 . We develop some semi-analytical solutions to the migration equation when the water beneath the plume saturates very slowly or very quickly relative to plume motion, and we solve the migration equation numerically otherwise.

It is well-known that CO_2 is weakly soluble in groundwater, and therefore that both residual CO_2 and CO_2 from the mobile plume will dissolve slowly into the nearby groundwater as the plume migrates. Because the density of groundwater increases with dissolved CO_2 content, the boundary layer of CO_2 -saturated groundwater near the mobile plume is unstable. This unstable density stratification eventually results in a Rayleigh–Bénard-type flow referred to as convective mixing, where fingers of “heavy”, CO_2 -saturated groundwater sink away from the interface as fingers of “fresh” groundwater rise upward [Lindeberg and Wesselberg, 1997; Ennis-King and Paterson, 2005; Riaz et al., 2006b].

Ennis-King and Paterson [2005] showed by simple scaling analysis that convective mixing dramatically increases the rate of CO_2 dissolution compared to diffusive transport alone, and noted that the small-scale features of convective mixing would likely necessitate an appropriate upscaled dissolution model at the basin scale. Pau et al. [2010] used high-resolution numerical simulations to study macroscopic features of the convective-mixing process, showing that the time-averaged rate of CO_2 dissolution due to convective mixing is approximately constant. Kneafsey and Pruess [2010b] confirmed this experimentally. Here, we take advantage of these results and incorporate a simple upscaled model for dissolution due to convective mixing into the migration equation.

Model for CO_2 migration at the basin scale

We are interested in large CO_2 storage projects, and therefore in the evolution of the CO_2 plume at the geologic-basin scale as proposed by Nicot [2008]—a schematic of the basin scale geologic setting is shown in figure 3.

We take the aquifer to be homogeneous, with an arbitrary tilt relative to the horizontal and a net groundwater through-flow to the right. We take the fluids to be incompressible and Newtonian, with constant and uniform properties within the aquifer. We employ a sharp-interface approximation, neglecting saturation gradients as well as the capillary pressure. We further assume vertical equilibrium, neglecting the vertical component of the fluid velocity relative to the horizontal one. We divide the domain into three regions of uniform fluid saturation with sharp interfaces corresponding to saturation discontinuities, as illustrated in figure 6. Region 1 is the plume of mobile CO_2 , containing free-phase CO_2 and a saturation S_{wc} of connate groundwater; Region 2 is the region from which the plume has receded, containing mobile groundwater and a saturation S_{gr} of trapped, free-phase CO_2 ; and Region 3 contains mobile groundwater, here also with some dissolved CO_2 , and no free-phase CO_2 .

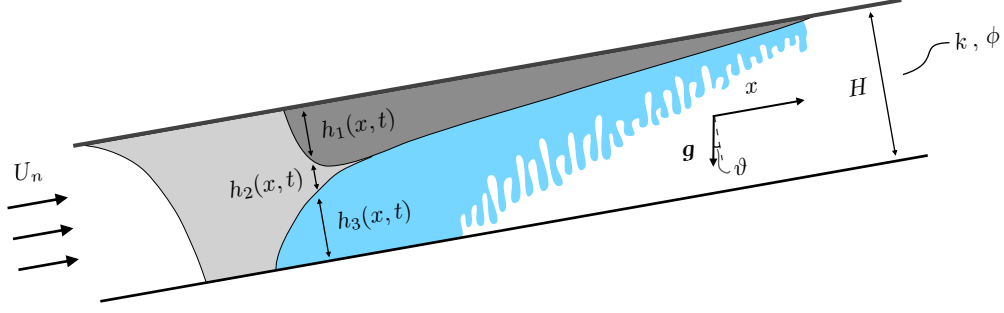


Figure 6: A schematic of the plume during post-injection migration, as the mobile CO_2 is pushed to the right by a combination of groundwater flow and aquifer slope, leaving trapped CO_2 in its wake. CO_2 dissolves from the plume by convective mixing, as indicated by the fingers of “heavy” groundwater (blue) falling away from the plume. We divide the domain into three regions of uniform CO_2 and groundwater saturation, separated by sharp interfaces corresponding to saturation discontinuities. Region 1 (dark gray) contains mobile CO_2 and a saturation S_{wc} of connate groundwater; Region 2 (light gray) contains mobile groundwater and a saturation S_{gr} of residual CO_2 ; Region 3 (white, blue) contains mobile groundwater with some dissolved CO_2 . The aquifer has a total thickness H , and the thickness of Region i , $i = 1, 2, 3$, is denoted $h_i(x, t)$. Groundwater flows naturally through the aquifer from left to right with velocity U_n ; the aquifer has permeability k and porosity ϕ , as well as an arbitrary angle of tilt ϑ measured counterclockwise from the direction of gravity.

With the assumptions above, and neglecting dissolution, we can write the Darcy velocity for each phase in each region and relate them through conservation of mass, accounting carefully for the residual fluid that crosses each interface [Hesse et al., 2006, 2008]. The resulting migration equation is

$$\begin{aligned} \tilde{\mathcal{R}} \frac{\partial h_1}{\partial t} + \left[\frac{Q}{(1 - S_{wc})\phi} \right] \frac{\partial f}{\partial x} + \kappa \sin \vartheta \frac{\partial}{\partial x} \left[(1 - f) h_1 \right] \\ - \kappa \cos \vartheta \frac{\partial}{\partial x} \left[(1 - f) h_1 \frac{\partial h_1}{\partial x} \right] = 0. \end{aligned} \quad (21)$$

The discontinuous accumulation coefficient $\tilde{\mathcal{R}}$ captures the volume loss due to capillary trapping by taking different values for drainage and imbibition,

$$\tilde{\mathcal{R}} = \begin{cases} 1 & \text{if } \partial h_1 / \partial t > 0 \text{ and } h_2 = 0, \\ 1 - \Gamma & \text{otherwise.} \end{cases} \quad (22)$$

The parameter $\Gamma = S_{gr}/(1 - S_{wc})$ is the capillary trapping number, which measures the fraction of CO_2 that is left behind at the imbibition front and takes a constant value between zero (no trapping) and one. A net volume rate Q of fluid flows through the aquifer from left to right. We denote the mobility of the mobile phase in Region i , $i = 1, 2, 3$, by $\lambda_i = k_{ri}/\mu_i$, where k_{ri} and μ_i are the relative permeability to that phase and the viscosity of that phase, respectively. For simplicity, we neglect the reduction of water mobility due to the presence

of trapped CO₂ in region 2, taking $\lambda_2 = \lambda_3$. The nonlinear function $f(h_1)$ is then given by

$$f(h_1) = \frac{\lambda_1 h_1}{\lambda_1 h_1 + \lambda_3 (H - h_1)}. \quad (23)$$

The characteristic interstitial velocity of immiscible buoyancy-driven flow in this system is

$$\kappa = \frac{\Delta \rho g k \lambda_1}{(1 - S_{wc}) \phi}, \quad (24)$$

where $\Delta \rho = \rho_w - \rho_g$ is the density difference between the groundwater and the CO₂, g is the force per unit mass due to gravity, and k and ϕ are the intrinsic permeability and porosity of the aquifer, respectively.

The conservation law for the layer of water beneath the plume, which has total thickness $h_w = h_2 + h_3 = H - h_1$, is readily derived from conservation of mass, or by rewriting Eq. (21) in terms of h_w . It can be written,

$$\begin{aligned} \tilde{\mathcal{R}} \frac{\partial h_w}{\partial t} + \left[\frac{Q}{(1 - S_{wc}) \phi} \right] \frac{\partial f_w}{\partial x} - \kappa \sin \vartheta \frac{\partial}{\partial x} \left[f_w h_1 \right] \\ + \kappa \cos \vartheta \frac{\partial}{\partial x} \left[f_w h_1 \frac{\partial h_1}{\partial x} \right] = 0 \end{aligned} \quad (25)$$

where

$$f_w = 1 - f = \frac{\lambda_3 (H - h_1)}{\lambda_1 h_1 + \lambda_3 (H - h_1)}. \quad (26)$$

This conservation law is redundant when there is no dissolution—since $h_w = H - h_1$, we need only solve Eq. (21). However, Eq. (25) will be useful when dissolution is included.

Model for Dissolution

We now consider dissolution of CO₂ from the mobile plume due to convective mixing.

Onset time for convective mixing It has been shown from linear stability analysis [Ennis-King and Paterson, 2005; Riaz et al., 2006b; Pau et al., 2010] that the onset time for convective mixing can be written

$$t_{\text{onset}} = \mathcal{C}_0 D_{\text{eff}} \left(\frac{\phi}{\Delta \rho_d g k \lambda_3} \right)^2 \quad (27)$$

where D_{eff} is the effective diffusivity of CO₂ in brine in the aquifer rock. We compare this time to the time it would take the leading edge of the CO₂ plume to travel one characteristic length in the horizontal direction during migration due to groundwater flow or formation slope,

$$t_{\text{flow}} = \frac{Q_i T_i / 2}{\mathcal{M} U_n H}, \quad t_{\text{slope}} = \frac{Q_i T_i / 2}{\Delta \rho g k \lambda_1 H \sin \vartheta}. \quad (28)$$

For typical but conservative values, we see that $t_{\text{onset}} \ll t_{\text{flow}}, t_{\text{slope}}$, and it is reasonable to assume that convective mixing begins instantaneously along the entire plume in post-injection migration.

Rate of dissolution due to convective mixing We take the upscaled volume flux of CO_2 dissolution due to convective mixing to be q_d , in principle a function of the details of the complex convective flow beneath the plume. It is natural to expect that the dissolution flux should scale with the saturated volume concentration of dissolved CO_2 in formation groundwater, which we denote c_s (volume of CO_2 per unit volume solution), and with the characteristic interstitial velocity of miscible density-driven flow in the formation,

$$\kappa_d = \frac{\Delta\rho_d g k \lambda_3}{\phi}, \quad (29)$$

where $\Delta\rho_d$ is the density increase of groundwater on becoming saturated with dissolved CO_2 . The simplest possible assumption is then

$$q_d = \mathcal{C} c_s \phi \kappa_d, \quad (30)$$

where \mathcal{C} is a dimensionless constant [see, *e.g.*, Ennis-King and Paterson, 2005]. The results of Pau et al. [2010] confirm this scaling, showing that the time-average of the dissolution flux is essentially constant and proportional to $c_s \phi \kappa_d$ with constant of proportionality $\mathcal{C} \approx 0.017$ after some relatively short onset time.

The layer of water with dissolved CO_2 We expect this expression for the dissolution rate to be valid only until the water beneath the plume begins to saturate with dissolved CO_2 , at which time the dissolution rate should decrease gradually to zero. For simplicity, we account for this saturating effect by setting the dissolution rate to zero at each position x when the water at that position becomes completely saturated with CO_2 . For this purpose, we define the degree of saturation $h_d(x, t)$ as

$$h_d(x, t) = \frac{1}{\phi c_s} \int_0^t q_d dt'. \quad (31)$$

This is the amount of dissolved CO_2 in the column of water at position x and time t , written as the effective thickness of a layer of dissolved CO_2 . We can then write

$$q_d = \begin{cases} \mathcal{C} c_s \phi \kappa_d & \text{if } h_1(x, t) > 0 \text{ and } h_d(x, t) < (H - h_1(x, t)), \\ 0 & \text{otherwise,} \end{cases} \quad (32)$$

where, again, the constant $\mathcal{C} \approx 0.017$ [Pau et al., 2010].

Dissolution and residual trapping Dissolution now enters the mass balance as a loss term \mathcal{L} on the right-hand side of Eq. (21), which we write as

$$\mathcal{L} = -\tilde{\mathcal{R}} \left[\frac{q_d}{(1 - S_{wc})\phi} \right]. \quad (33)$$

Note that the loss term \mathcal{L} includes the discontinuous accumulation coefficient $\tilde{\mathcal{R}}$. We define \mathcal{L} in this way so that interface displacements due to dissolution do not contribute to capillary trapping, and for this purpose we also modify the definition of $\tilde{\mathcal{R}}$,

$$\tilde{\mathcal{R}} = \begin{cases} 1 & \text{if } \partial h_1 / \partial t > -q_d / (1 - S_{wc})\phi \text{ and } h_2 = 0, \\ 1 - \Gamma & \text{otherwise.} \end{cases} \quad (34)$$

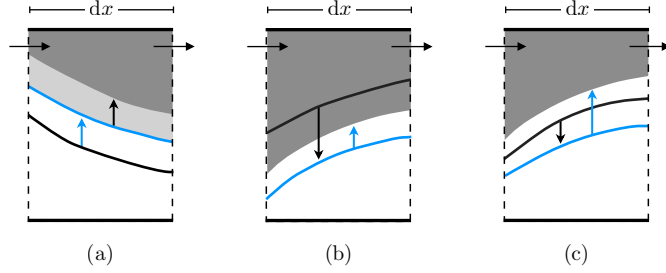


Figure 7: There are three possible scenarios for local interface displacement. The local shape and position of the CO_2 plume is shown here (shaded dark gray) after displacement of the original CO_2 -water interface (solid black line) due to flow of CO_2 (black arrow) and dissolution (blue arrow). A hypothetical intermediate position of the CO_2 -water interface is also shown (solid blue line). We model dissolution so that interface displacements due to dissolution do not contribute to capillary trapping. This means that (a) when dissolution enhances imbibition, only the component of interface motion that is driven by flow of CO_2 contributes to capillary trapping (shaded light gray); (b) when dissolution attenuates drainage, the interface still experiences net drainage and no capillary trapping occurs; and (c) when dissolution drives drainage into imbibition, no capillary trapping occurs because any residual CO_2 would dissolve as the water imbibes. Dissolution and capillary trapping are then effectively decoupled.

This is physically motivated by the expectation that residual CO_2 would dissolve as the interface is displaced unless the interface moves faster than by dissolution alone, as illustrated in Figure 7. Effectively, this decouples the processes of capillary trapping and dissolution.

We emphasize that this model for dissolution features several key simplifications. First, we have neglected transport of dissolved CO_2 within the water—this is motivated by the fact that the CO_2 plume typically travels much faster than the water because of its substantially higher mobility. Second, we have assumed that dissolution ends abruptly when the water becomes saturated, rather than decreasing gradually. This assumption is reasonable if the rate of dissolution decreases quickly to zero as the water saturates; we adopt it here for simplicity, and because we believe it captures the essential dissolution-limiting feature of the finite amount of water underneath the plume. Third, we have not accounted for dissolution of the residual CO_2 —this is motivated by the fact that residual CO_2 is located primarily in the wake of the plume rather than under it, so we do not expect it to impact the migration or dissolution of the mobile plume. Fourth, for simplicity, we do not account for dissolved CO_2 in the connate water. The importance of these effects has not yet been studied, but our emphasis here is on deriving physical insight from a simple but physically reasonable model and we do not expect these effects to have a leading-order impact on our results.

Migration equation with dissolution

We recall the migration equations for the gravity current of free-phase CO_2 and the curtain of dissolved CO_2 , which we presented in a previous progress report. They read, in dimensionless

form,

$$\tilde{\mathcal{R}} \frac{\partial \eta}{\partial \tau} + N_f \frac{\partial f}{\partial \xi} + N_s \frac{\partial}{\partial \xi} \left[(1-f) \eta \right] - N_g \frac{\partial}{\partial \xi} \left[(1-f) \eta \frac{\partial \eta}{\partial \xi} \right] = -\tilde{\mathcal{R}} N_d, \quad (35)$$

and

$$\begin{aligned} \frac{\partial \eta_d}{\partial \tau} + (1-S_{wc}) N_f \frac{\partial f_d}{\partial \xi} - (1-S_{wc}) N_s \frac{\partial}{\partial \xi} \left[f_d \eta \right] \\ + (1-S_{wc}) N_g \frac{\partial}{\partial \xi} \left[f_d \eta \frac{\partial \eta}{\partial \xi} \right] = \frac{N_d}{\Gamma_d} - S_{wc} \frac{\partial \eta}{\partial \tau} - (1-\tilde{\mathcal{R}}) \left(\frac{\partial \eta}{\partial \tau} + N_d \right), \end{aligned} \quad (36)$$

where $\eta = h_1/H$, $\tau = t/T_c$, $\xi = x/L_c$, $\eta_d = h_d/H$, and with

$$\tilde{\mathcal{R}} = \begin{cases} 1 & \text{if } \partial \eta / \partial \tau > -N_d, \\ 1 - \Gamma & \text{otherwise,} \end{cases} \quad (37)$$

and

$$f(\eta) = \frac{\mathcal{M}\eta}{\mathcal{M}\eta + (1-\eta)} \quad , \quad f_d(\eta, \eta_d) = \frac{\eta_d}{\mathcal{M}\eta + (1-\eta)}, \quad (38)$$

where $\mathcal{M} = \lambda_1/\lambda_3$ is the mobility ratio. We choose the characteristic length scale to be the length of a rectangle of aquifer of height H and containing a volume $Q_i T_i/2$ of CO_2 , $L_c = Q_i T_i/2(1-S_{wc})\phi H$, where Q_i is the volume rate of injection per unit length of well-array during the injection period and T_i is the duration of the injection period. The characteristic time scale T_c is arbitrary. The constants N_f , N_s , and N_g are given by

$$N_f = \frac{T_c}{T_i} \frac{Q}{Q_i/2} \quad , \quad N_s = \frac{T_c}{L_c} \kappa \sin \vartheta \quad , \quad N_g = \frac{T_c}{L_c} \kappa \cos \vartheta \frac{H}{L_c}, \quad (39)$$

and N_d is given by

$$N_d = \begin{cases} \alpha \chi_v \kappa_d \frac{T_c}{H} & \text{if } \eta(\xi, \tau) > 0 \quad \text{and} \quad \eta_d(\xi, \tau) < (1-\eta(\xi, \tau)), \\ 0 & \text{otherwise,} \end{cases} \quad (40)$$

The constant $\Gamma_d = \chi_v/(1-S_{wc})$ is defined such that one unit volume of the mobile CO_2 plume becomes $1/\Gamma_d$ units of volume of the curtain upon dissolving. Without loss of generality, we choose $N_f \geq 0$ —thus groundwater flow is always *to the right* by convention. Aquifer slope can be either positive ($N_s > 0$) for counterclockwise aquifer tilt or negative ($N_s < 0$) for clockwise aquifer tilt.

The model for CO_2 migration now consists of a system of two coupled migration equations. Equation (35) is a model for the migration of the mobile plume of CO_2 , consisting of a conditional accumulation term balanced by three nonlinear flux terms and a conditional loss term. The discontinuous nature of the accumulation term captures the effect of capillary trapping. The flux terms have the following physical interpretations: the first is advective in nature, capturing the motion of the CO_2 due to groundwater flow through the aquifer; the second is also advective, capturing the motion of the CO_2 due to the tilt of the aquifer; and the third is diffusive, capturing the upward spreading of the CO_2 against the caprock due to buoyancy. The loss term captures the loss of CO_2 from the plume due to dissolution. Equation (36) is a model for the migration of the curtain of water saturated with dissolved CO_2 , and the physical interpretation of the terms is similar.

The injection period

During injection, we assume that a constant volume flow rate Q_i of CO₂ per unit length of the line-drive well array is pumped into the aquifer. Injection typically dominates the flow, and we therefore neglect natural groundwater flow and slope relative to injection, $Q = U_n H + Q_i/2 \approx Q_i/2$ and $N_s/N_f \ll 1$. We then assume that the flow rate Q_i is split evenly between the left and right sides of the injection well, and therefore that the plume shape is symmetric across the injection well. We take the characteristic timescale T_c to be the duration of injection T_i so that $\tau = 1$ is the end of the injection period and $N_f \equiv 1$.

To understand the impact of dissolution on the plume shape during injection, we compare the rate of CO₂ injection, Q_i , to an estimate of the rate of CO₂ dissolution, Q_d . The upscaled rate of CO₂ dissolution per unit length of CO₂-water interface is $(1 - S_{wc})q_d$, as discussed above. Without dissolution, the extent of the plume at the end of injection is $2\mathcal{M}Q_iT_i/(1 - S_{wc})\phi H$, from Part 1. We then estimate

$$\frac{Q_d}{Q_i} \sim \frac{q_d \mathcal{M} Q_i T_i}{\phi H Q_i} = \mathcal{M} N_d. \quad (41)$$

Taking typical but conservative values, $\mu_w = 5.5 \times 10^{-4}$ Pa s, $\mu_g = 6 \times 10^{-5}$ Pa s, $\chi_v = 0.1$, $S_{wc} = 0.4$, $\phi = 0.15$, $\Delta\rho_d = 10 \text{ kg/m}^3$, $k = 100 \text{ md} = 10^{-13} \text{ m}^2$, $T_c = T_i = 30$ years, $H = 100 \text{ m}$, we find that $Q_d/Q_i \sim 10^{-2} \ll 1$, implying that the fraction of the CO₂ that dissolves during injection is negligible. Note that we have neglected the onset time for convective mixing as well as the finite supply of water, both of which would decrease the amount of CO₂ that would dissolve during injection. We have also used the length of the plume at the end of injection, again giving an overestimate of the amount of CO₂ that would dissolve during injection. We therefore conclude that dissolution is negligible during injection and we use the injection solution of Nordbotten et al. [2006].

Post-injection migration

Once injection has ended, the plume migrates due to both slope and groundwater flow. The characteristic timescale in post-injection is arbitrary, but in order to maintain a continuous time variable we redefine τ in post-injection as

$$\tau = 1 + \frac{t - T_i}{T_c} \quad (42)$$

so that the end of injection, $t = T_i$, always corresponds to $\tau = 1$. For convenience, we choose the characteristic time T_c such that $N_f \equiv 1$,

$$T_c = \frac{Q_i T_i / 2}{U_n H}, \quad (43)$$

in which case N_s gives the importance of advection due to slope relative to that due to groundwater flow; N_g gives the importance of diffusive spreading due to buoyancy relative to advection due to groundwater flow, analogous to the inverse of a Peclet number in mass transfer; and N_d gives the importance of loss due to dissolution relative to advection due to groundwater flow, analogous to a Damköhler number in reactive transport.

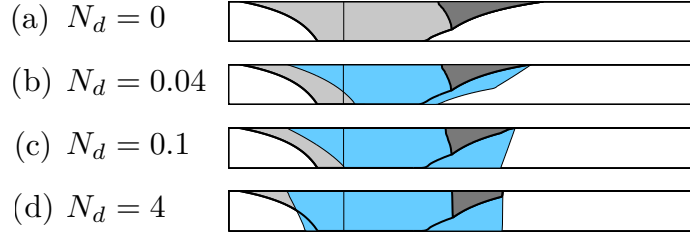


Figure 8: Numerical solutions to (35) and (36) for the shape of the plume (dark gray) and the curtain (blue) at $\tau = 2.5$ during post-injection migration, with $\mathcal{M} = 2$, $\Gamma = 0.5$, $\Gamma_d = 0.1$, $N_f = 1$, $N_s = -0.75$, $N_g = 0$, and $N_d = 0, 0.04, 0.1$, and 4 , as indicated. Where the curtain reaches the bottom of the aquifer, dissolution has stopped because the water is saturated. We identify two limits: (b) when the water saturates *slowly* relative to plume migration, dissolution is not limited by the amount of water beneath the plume, and (d) when the water saturates very quickly (*instantaneously*) relative to plume migration, the water beneath the plume is completely saturated with dissolved CO_2 and only the leading edge of the plume dissolves as it migrates.

While Equations (35) and (36) must be solved numerically in general, we identify two limits in which analytical progress is possible (figure 8). When the water beneath the mobile plume saturates with dissolved CO_2 slowly relative to plume migration, the curtain does not interact with the bottom of the aquifer. In this *slow-saturation* limit, Equation (35) can be solved independently of Eq. (36). When the water beneath the mobile plume saturates with dissolved CO_2 very quickly relative to plume migration, the water beneath the plume will be completely saturated except at the leading edge. In this *instantaneous-saturation* limit, the majority of the plume will not experience dissolution as it migrates and Equation (35) can again be solved independently of Eq. (36). Below, we develop semi-analytical solutions to Equation (35) in these two limits.

The slow-saturation limit

When the water beneath the plume saturates with dissolved CO_2 slowly compared to plume motion, dissolution from the plume is not limited by the supply of water and Eq. (35) can be solved independently of Eq. (36). In this limit, we develop semi-analytical solutions to Eq. (35) via the method of characteristics. Note that CO_2 migration becomes independent of Γ_d in this limit because the water does not saturate. All of the expressions and results for this limit simplify to those from the model with capillary trapping only when $N_d = 0$.

As for the capillary-trapping-only model, the post-injection problem is more difficult than the injection problem because of the complex interactions between slope, groundwater flow, capillary trapping, and now dissolution—waves collide, and we divide the analysis into parts based on the types of collisions that occur.

Here we do not get into all the mathematical details on the derivation of the solutions to the hyperbolic equations. Based on the wave speeds of the leading and trailing edges of the moving plume, we can divide the flow-with-weak-slope interval into cases based on the order in which these collisions occur. We did so explicitly for the capillary-trapping-only model, finding five cases within this interval. The five possible cases here, and are as follows: in

case 1, an incipient shock forms on the left and consumes the entire left front before a peak forms; in case 2, an incipient shock forms on the left and a peak forms at the bottom of the plume, and then the left front compacts into a shock; in case 3, a peak forms at the bottom of the plume and no shock forms; in case 4, an incipient shock forms on the right and a peak forms at the bottom of the plume, and then the right front compacts into a shock; and in case 5, an incipient shock forms on the right and consumes the entire right front before a peak forms. The delineation between these cases now depends on N_d in addition to \mathcal{M} , Γ , and N_s/N_f and we are no longer able to delineate them explicitly because the collision times are defined implicitly. Instead, we implement a decision-tree algorithm to evaluate and compare these times, and evolve the plume accordingly. We describe in detail the remainder of the development for case 2.

Flow with weak slope, case 2, in the slow-saturation limit In case 2, the first two collisions are the development of an incipient shock at the left, which occurs at time τ_{LL}^σ , and the formation of a peak at the bottom, which occurs at time τ_{LR}^{RL} . The ordering of these two collisions is unimportant. The peak is formed by the intersection of the left and right fronts, and the initial thickness $g_{0,p}$ of the waves forming the peak at time τ is given implicitly by

$$\begin{aligned} \left[\frac{N_s}{\mathcal{M}-1}(\tau-1) \right] g_{0,p}^3 + \left[\frac{2\mathcal{M}(1-\Gamma)}{\Gamma} - \left(\mathcal{M}N_f + \frac{\mathcal{M}}{\mathcal{M}-1}N_s \right) (\tau-1) \right] g_{0,p} \\ + \left[N_s N_d (\tau-1)^2 \right] g_{0,p}^2 - \left[\frac{2\mathcal{M}(1-\Gamma)}{\Gamma} (\mathcal{M}-1) N_d (\tau-1) \right] = 0. \end{aligned} \quad (44)$$

The shock, once it has formed, collides continuously with waves of the left front as it grows. Construction of the differential equation describing the growth of the shock is straightforward—we begin by posing the collision of the shock at time τ^* with an arbitrary wave of the left front of initial thickness g_0^* and current thickness g^* . The position of the shock at time τ^* can be written

$$\xi_\sigma^* = \xi_\sigma(\tau^*) = \xi_{LL}^\sigma + \int_{\tau_{LL}^\sigma}^{\tau^*} \sigma \, d\tau. \quad (45)$$

The shock speed σ is evaluated from the Rankine–Hugoniot condition,

$$\sigma(g^*) = \frac{1}{1-\Gamma} \frac{[[G]]}{[[g]]} = \frac{1}{1-\Gamma} \frac{G(g^*)}{g^* - 1}, \quad (46)$$

where the notation $[[\circ]]$ indicates the difference or “jump” in the indicated quantity across the shock. Note that only the current thicknesses of the waves on either side of the shock influence the instantaneous shock speed. The position at time τ^* of the wave with initial thickness g_0^* is

$$\xi^* = \xi(g^*, \tau^*) = -\frac{\mathcal{M}}{g_0^{*2}} + \frac{1}{1-\Gamma} \int_1^{\tau^*} G'(g^*) \, d\tau. \quad (47)$$

Equating ξ_σ^* with ξ^* since these must be equal by the definition of g^* and τ^* , we differentiate the resulting expression with respect to τ^* and rearrange to find an ordinary differential

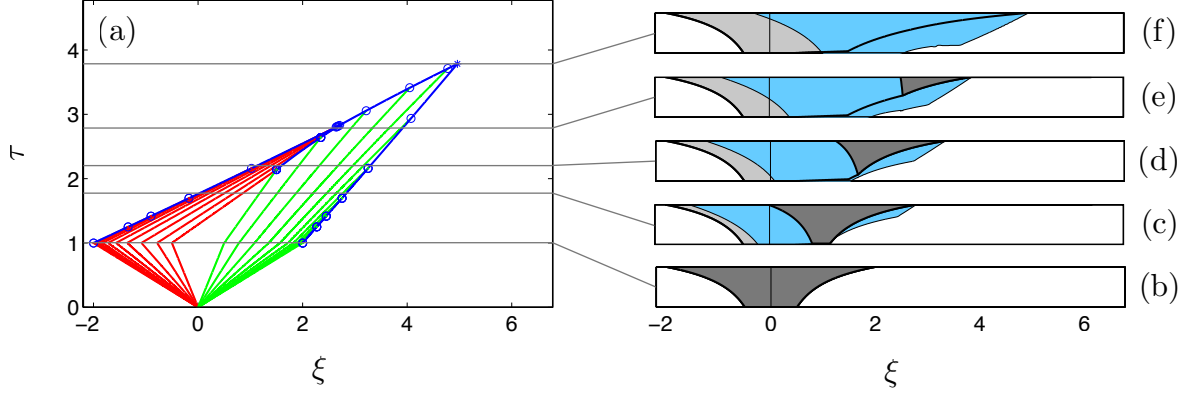


Figure 9: Post-injection migration in the slow-saturation limit for case 2 of the flow-with-weak-slope, with $\mathcal{M} = 2$, $\Gamma = 0.5$, $N_f = 1$, $N_s = -0.75$, $N_d = 0.04$, and $\Gamma_d = 0.1$: (a) the evolution of the plume in characteristic space with waves of the left and right fronts in red and green, respectively, and the paths of the peak, the shock, and the leading and trailing edges of the plume in blue; (b)–(f) the shape of the plume at several times during migration, with mobile CO_2 in dark gray, the region containing trapped CO_2 in light gray, the curtain of groundwater with dissolved CO_2 in blue, and groundwater in white. The curtain is approximate because we do not solve Eq. (36) in this limit. Note that the characteristics are not straight lines because the waves shrink and therefore change speed as they migrate, and also that the leading and trailing edges of the plume are not characteristics, but rather cut across characteristics.

equation for the shock height as a function of time,

$$\frac{dg^*}{d\tau^*} = \frac{\sigma(g^*) - \partial\xi^*/\partial\tau^*}{\partial\xi^*/\partial g^*}. \quad (48)$$

This ordinary differential equation (ODE) is not separable unless $N_d = 0$, so we integrate it numerically from time $\tau^* = \tau_{LL}^\sigma$ until it collides with the peak, at which time $g^*(\tau^*) = g_p(\tau^*)$. The shock then collides continuously with the right front until it vanishes—the development of the ODE for the shock height as a function of time during this period is analogous to that above. We plot the characteristics and plume shapes for case 2 in the slow-saturation limit in figure 9.

The instantaneous-saturation limit

When the water beneath the plume saturates with dissolved CO_2 very quickly relative to plume migration, the majority of the plume migrates over saturated water and is therefore not influenced by dissolution. Only the leading edge of the plume encounters unsaturated water as it migrates, and all of this water must saturate instantaneously as the leading edge travels over it. In this limit, we can again develop semi-analytical solutions via the method of characteristics. Note that CO_2 migration becomes independent of N_d in this limit because the water is assumed to saturate instantaneously. All of the expressions and results for this limit simplify to those from the capillary-trapping-only model when $\Gamma_d = 0$. Although the

procedure we use here is general, we again restrict our analysis to the flow-with-weak-slope interval, $-\mathcal{M} < N_s/N_f < 1$, for simplicity.

Initial condition in the instantaneous-saturation limit Because the water beneath the plume saturates instantaneously relative to plume migration, the initial condition for post-injection migration changes instantly from the end-of-injection plume shape to a modified shape as CO₂ from the plume dissolves to saturate the water beneath. Recall that the end-of-injection shape is assumed to be symmetric across $\xi = 0$. The right half of the end-of-injection shape is given by

$$\eta_i = \begin{cases} 1 & 0 < \xi < 1/\mathcal{M}, \\ (\sqrt{\mathcal{M}/\xi} - 1)/(\mathcal{M} - 1) & 1/\mathcal{M} < \xi < \mathcal{M}, \\ 0 & \mathcal{M} < \xi. \end{cases} \quad (49)$$

The dimensionless volume of the end-of-injection shape is 2. The volume of free-phase CO₂ within an infinitesimal section of the end-of-injection plume at some position ξ is $(1 - S_{wc})\phi\eta_i(\xi)d\xi$. The volume of CO₂ that can be dissolved in the water at the same position ξ is $\phi\chi_v(1 - \eta_0(\xi))d\xi$, where η_0 is the shape of the plume after saturating the water. Conserving the total mass of CO₂ at position ξ before and after the water saturates with dissolved CO₂, we have that

$$(1 - S_{wc})\phi\eta_i = (1 - S_{wc})\phi\eta_0 + \phi\chi_v(1 - \eta_0), \quad (50)$$

which can be rearranged to give

$$\eta_0 = \frac{\eta_i - \Gamma_d}{1 - \Gamma_d}. \quad (51)$$

The new initial thickness η_0 goes to 0 at $\eta_i = \Gamma_d$, which occurs at position

$$\xi^* = \frac{\mathcal{M}}{[(\mathcal{M} - 1)\Gamma_d + 1]^2}. \quad (52)$$

This is the position where the water column can dissolve exactly as much free-phase CO₂ as was present. For $\xi < \xi^*$, the water saturates completely before dissolving all of the free-phase CO₂; for $\xi > \xi^*$, the free-phase CO₂ dissolves completely but is not sufficient to saturate the water. We then have

$$\eta_0 = \begin{cases} 1 & 0 < \xi < 1/\mathcal{M}, \\ (\eta_i - \Gamma_d)/(1 - \Gamma_d) & 1/\mathcal{M} < \xi < \xi^*, \\ 0 & \xi^* < \xi. \end{cases} \quad (53)$$

We plot Eq. (53) in figure 10 for several values of Γ_d . The dimensionless volume of this new initial shape is $2/((\mathcal{M} - 1)\Gamma_d + 1)$, where a dimensionless volume $2(\mathcal{M} - 1)\Gamma_d/((\mathcal{M} - 1)\Gamma_d + 1)$ of free-phase CO₂ has dissolved. Rewriting Eq. (53) in terms of characteristics, we have

$$\xi_L^0(g) = -\frac{\mathcal{M}}{((1 - \Gamma_d)g + \mathcal{M}\Gamma_d)^2} \quad \xi_R^0(g) = \frac{\mathcal{M}}{((1 - \Gamma_d)g + \mathcal{M}\Gamma_d)^2}. \quad (54)$$

This will be the initial condition for post-injection migration in the instantaneous-saturation limit.

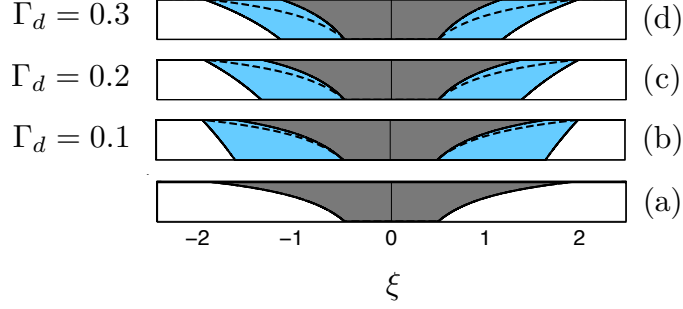


Figure 10: The initial condition for post-injection migration in the instantaneous-saturation limit for $\mathcal{M} = 2$ (a) at the end of injection (Eq. (49)) and (b)–(c) after saturating the water for $\Gamma_d = 0.1$ – 0.3 , as indicated (Eq. (53)). Free-phase CO_2 is shown in dark gray, water is shown in white, the curtain of water saturated with dissolved CO_2 is shown in blue, and the end-of-injection shape from (a) is indicated in (b)–(c) as a dashed black line.

Nose position in the instantaneous-saturation limit The leading edge of the plume dissolves rapidly in this limit, so we must handle its propagation separately. As the leading edge propagates to the right, it must lose enough mobile CO_2 to saturate the water that passes beneath. As a result, the plume is truncated at some moving position x^* where all of the CO_2 to the right of x^* has dissolved and all of the water to the left of x^* is saturated. By definition, then, x^* is the position across which there is no flux of CO_2 . The volume flow rate of mobile CO_2 to the right at x^* can be written

$$F_g^*(x^*, t) = F_g(x^*, t) - (1 - S_{wc})\phi h_1(x^*, t) s_d, \quad (55)$$

where F_g is the total horizontal flow of CO_2 and $s_d = dx^*/dt$. Similarly, the volume flow rate of water to the left at x^* can be written

$$F_w^*(x^*, t) = \phi h_w(x^*, t) s_d - F_w(x^*, t), \quad (56)$$

where F_w is the total horizontal flow of water. The water flowing to the left must dissolve and carry away the entire amount F_g^* of CO_2 so that no mobile CO_2 crosses ξ^* , and we therefore have that $F_g^* = \chi_v F_w^*$. Rearranging this expression gives

$$s_d = \frac{F_g + \chi_v F_w}{(1 - S_{wc})\phi h_1 + \chi_v \phi h_w}, \quad (57)$$

where the right-hand side is evaluated at x^* . This is the speed of the instantaneous-saturation shock at the leading edge of the plume, given by difference in the total flux of CO_2 across the shock divided by the difference in the total thickness of the CO_2 layer across the shock. Making s_d dimensionless and writing it in terms of g in the hyperbolic limit, we have

$$\sigma_d = \frac{\chi_v(\mathcal{M} - 1)N_f g + (1 - \chi_v)(\mathcal{M}N_f(g - 1) + N_s(\mathcal{M} - g)(g - 1)/(\mathcal{M} - 1))}{(1 - \Gamma_d)(g - 1)g + (\mathcal{M} - 1)\Gamma_d g}, \quad (58)$$

where σ_d is the dimensionless shock speed and the right-hand side is evaluated at ξ^* . We can then formulate an ODE for the height of the shock as a function of time. This ODE is not separable for $\Gamma_d \neq 0$, so we integrate it numerically.

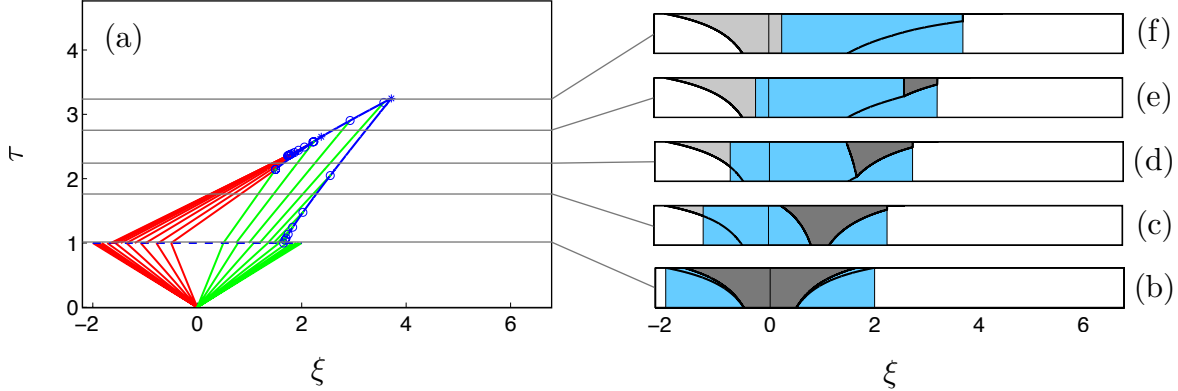


Figure 11: Post-injection migration in the instantaneous-saturation limit for case 2, with $\mathcal{M} = 2$, $\Gamma = 0.5$, $N_f = 1$, $N_s = -0.75$, $S_{wc} = 0.4$, and $\Gamma_d = 0.1$: (a) the evolution of the plume in characteristic space with waves of the left and right fronts in red and green, respectively, and the paths of the peak, the shock, and the leading and trailing edges of the plume in blue; (b)–(f) the shape of the plume at several times during migration, with mobile CO_2 in dark grey, the region containing trapped CO_2 in light gray, the curtain of groundwater with dissolved CO_2 in blue, and groundwater in white. The curtain is approximate because we do not solve Eq. (36) in this limit. Note that the characteristics contract instantaneously across $\tau = 1$, where the characteristic timescale changes from the injection timescale to the post-injection timescale—this is the transition from the end-of-injection shape as the water beneath the plume saturates with dissolved CO_2 . Unlike in the slow-saturation limit, the characteristics here are straight lines. The leading edge of the plume is the instantaneous-saturation shock, which truncates the plume by cutting across characteristics.

Flow with weak slope, case 2, in the instantaneous-saturation limit In case 2, the first two collisions are the development of an incipient shock at the left, which occurs at time τ_{LL}^σ , and the formation of a peak at the bottom, which occurs at time τ_{LR}^{RL} . The ordering of these two collisions is unimportant. The initial height of the peak is \mathcal{M} , and the height of the peak as a function of time is given by the value of g at which ξ_L and ξ_R intersect, which yields a fourth-order polynomial in g —the height of the peak is the smallest root of the polynomial on the interval $g \in [0, 1]$. Meanwhile, the right front is truncated as the instantaneous-saturation shock evolves. The shock on the left evolves according to an ODE constructed as in Eq. (48), but where $\partial\xi/\partial g$ and $\partial\xi/\partial\tau$ are calculated using the expression for the shape of the left front. The shock evolves until it collides with the peak, at which time the entire left front has become a shock. Thereafter, the shock collides continuously with the right front until it collides with the instantaneous-saturation shock at the leading edge of the plume. We plot the characteristics and plume shapes for case 2 in the instantaneous-saturation limit in figure 11.

Storage efficiency

Here, we interpret these results in the context of the storage efficiency, a macroscopic measure of CO_2 migration. The storage efficiency is the volume of CO_2 stored per unit pore volume of aquifer “used,” and is an important metric in capacity estimation [Bachu et al., 2007].

We again define the storage efficiency ε as

$$\varepsilon = \frac{V_{\text{CO}_2}}{V_T} = \frac{Q_i T_i}{H L_T (1 - S_{wc}) \phi} = \frac{2}{\xi_T}, \quad (59)$$

which is the ratio of the total volume of CO_2 injected, $Q_i T_i$, to the total pore volume available for CO_2 storage in a rectangle of thickness H and length L_T , where L_T is the total extent in the x -direction of the fully trapped CO_2 plume [Juanes and MacMinn, 2008; Juanes et al., 2010] and $\xi_T = L_T/L_c$. The storage efficiency is inversely proportional to the dimensionless footprint of residual CO_2 , *i.e.*, for a given volume of CO_2 injected, a larger footprint corresponds to less-efficient storage.

We also consider an additional parameter here, which is the fraction Φ_d of CO_2 that has been trapped by dissolution once all of the CO_2 has been trapped. The fraction dissolved is a measure of the importance of dissolution relative to capillary trapping since the remaining fraction $1 - \Phi_d$ must be trapped by capillarity.

Our focus in our study of storage efficiency from capillarity was the competition between flow and slope, as measured by the ratio N_s/N_f . Here, we focus on the interactions between migration, residual trapping, and dissolution. For this purpose, we fix N_s/N_f , Γ , Γ_d , and S_{wc} , and evaluate the storage efficiency and the fraction dissolved as a function of the ratio N_d/N_f for several values of \mathcal{M} .

Both the storage efficiency and the fraction dissolved increase monotonically with N_d/N_f (figure 12). However, storage efficiency decreases with \mathcal{M} whereas fraction dissolved increases with \mathcal{M} . This is because the plume becomes longer and thinner as \mathcal{M} increases, which slows residual trapping but increases the amount of dissolution. In this sense, residual trapping and dissolution are complementary trapping mechanisms.

Comparing storage efficiency to fraction dissolved at the same value of N_d , we find that the combination of residual trapping and dissolution can greatly increase storage efficiency even when the fraction dissolved is small (figure 13). This is a consequence of the complementary nature of dissolution and residual trapping: capillarity traps CO_2 at the short, trailing edge of the plume, while dissolution acts most strongly along the long, leading edge.

In particular, dissolution slows the speed at which the leading edge advances, decreasing total migration distance and increasing the storage efficiency (Eq. 59). Without dissolution, the dimensionless speed of the nose of the plume is constant MacMinn et al. [2010],

$$v_{\text{nose}} = d\xi_{RR}/d\tau = \mathcal{M}N_f + N_s. \quad (60)$$

With dissolution, the speed of the nose in the slow-saturation limit can be evaluated and is given by

$$v_{\text{nose}}(\tau) = \frac{\mathcal{M}N_f + \mathcal{M}N_s/(\mathcal{M} - 1)}{(1 + (\mathcal{M} - 1)N_d(\tau - 1))^2} - \frac{N_s}{\mathcal{M} - 1} - \frac{2\mathcal{M}(\mathcal{M} - 1)N_d}{(1 + (\mathcal{M} - 1)N_d(\tau - 1))^3}. \quad (61)$$

The speed of the nose is no longer constant in time, so the nose now traverses a curved path in space-time (figure 14a). In addition, the time-averaged speed of the nose decreases monotonically with N_d (figure 14b). Slowing the leading edge of the plume has a twofold impact on migration distance and therefore on storage efficiency: it decreases both migration

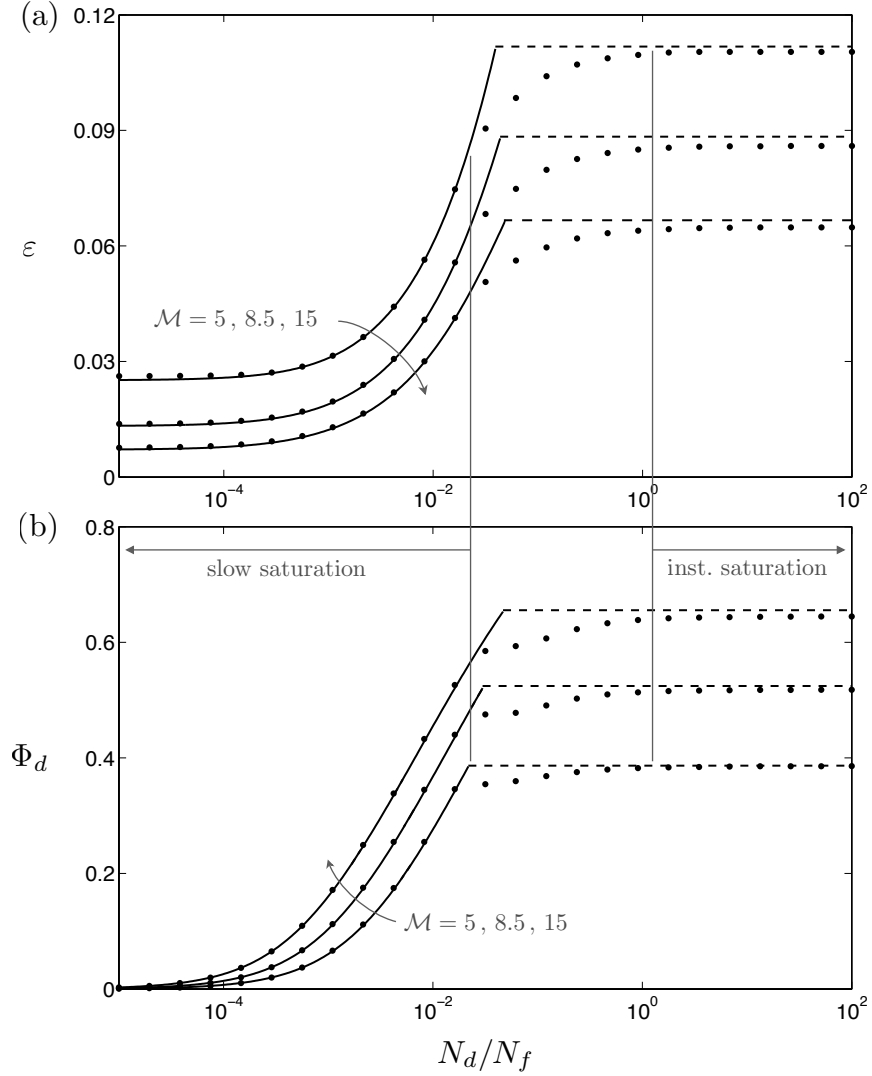


Figure 12: Both (a) the storage efficiency, ε , and (b) the fraction of CO_2 trapped by dissolution, Φ_d , increase monotonically with dimensionless dissolution rate, N_d/N_f . Here, we fix the values of $\Gamma = 0.3$, $N_f = 1$, $N_s = -0.75$, $S_{wc} = 0.4$, and $\Gamma_d = 0.06$, and show curves for three typical values of \mathcal{M} , as indicated. Storage efficiency decreases monotonically with \mathcal{M} , as in Part 1, because the plume becomes longer and thinner as \mathcal{M} increases; Φ_d increases monotonically with \mathcal{M} because the amount of dissolution is proportional to the length of the plume. The water beneath the plume saturates more quickly as N_d increases, and both ε and Φ_d approach a plateau in the instantaneous-saturation limit where the water is completely saturated. The height of this plateau depends on Γ_d , but not on N_d . The semi-analytical solutions in the slow-saturation limit (solid black line) and the instantaneous-saturation limit (dashed black line) agree with numerical solutions of the migration equations to within a few percent.

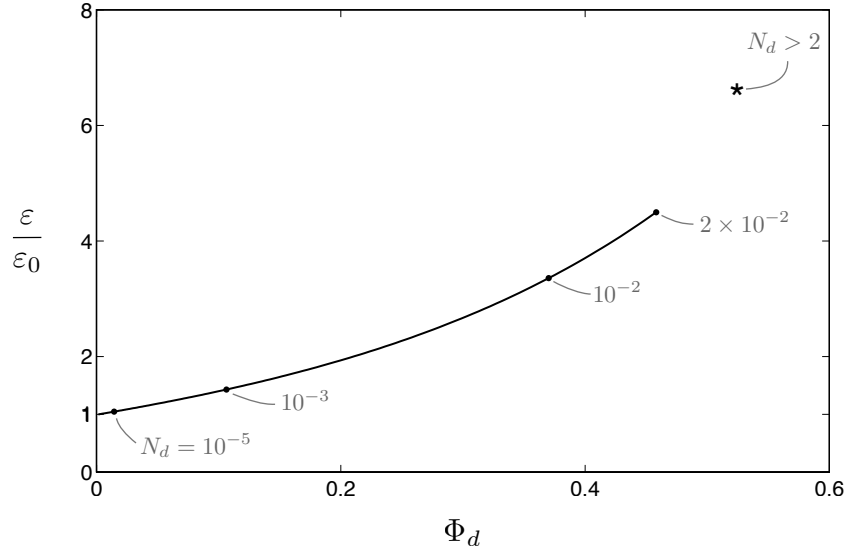


Figure 13: Dissolution can lead to a several-fold increase in storage efficiency even when the fraction dissolved is small. For $\mathcal{M} = 8.5$, we plot here the storage efficiency ε from figure 12(a), scaled by the storage efficiency without dissolution, ε_0 , against the corresponding fraction dissolved Φ_d from figure 12(b). Both quantities increase monotonically with N_d (figure 12). Several values of N_d are indicated for reference (black dots). Results shown here are from the semi-analytical solutions for the limiting cases of slow-saturation (solid black line) and instantaneous-saturation (black star). The transition from slow to instantaneous saturation is not shown. The storage efficiency is twice the no-dissolution value with only 20% of the CO_2 trapped by dissolution, increasing in the instantaneous-saturation limit to about 6.6 times the no-dissolution value with 52% of the CO_2 trapped by dissolution.

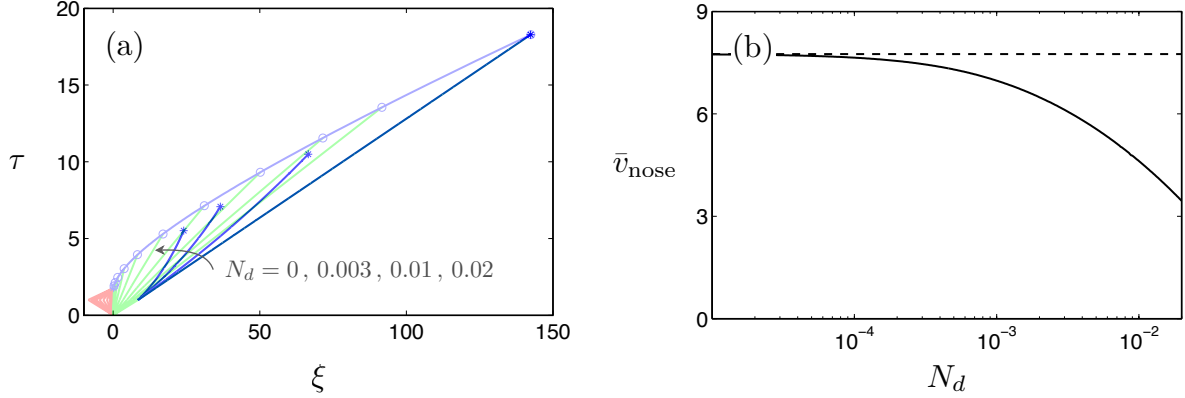


Figure 14: Dissolution reduces the speed at which the nose of the plume advances, as shown here in the slow-saturation regime for $\mathcal{M} = 8.5$, $\Gamma = 0.3$, $N_f = 1$, and $N_s = -0.75$. (a) In space-time, we superpose the path of the nose for several values of N_d (solid blue lines) onto the characteristics without dissolution (faded red, green, blue lines). Without dissolution ($N_d = 0$), the path of the nose is a straight line in space-time because the speed of the nose is constant. With dissolution, the nose travels more slowly and its path in space-time is curved because its speed is no longer constant. (b) The mean velocity of the nose (solid black line) decreases by more than a factor of 2 from its no-dissolution value (dashed black line) as N_d increases from 0 to 0.02. For $N_d > 0.02$, plume migration is no longer in the slow-saturation limit for these parameters.

speed and total migration time. Slowing the leading edge of the plume decreases total migration time because the plume of mobile CO_2 shrinks from the rear due to residual trapping, becoming fully trapped when the trailing edge catches the leading edge. This occurs more quickly when dissolution slows the leading edge (figure 14a). The advancement of the nose in the instantaneous-saturation regime is more complicated because the leading edge is a shock, but the behavior is qualitatively similar.

Because dissolution acts most strongly along the long, leading edge of the plume, residual trapping remains important even for large values of N_d . We illustrate the complementary nature of residual trapping and dissolution via the time-evolution of the volume fractions of mobile, residual, and dissolved CO_2 (figure 15). This provides a quantitative, physical understanding of the time-evolution of the role of trapping mechanisms in immobilizing the buoyant CO_2 , as recognized qualitatively in terms of perceived storage security in IPCC [2005, pg. 208, figure 5.9].

Summary of the mathematical model

The volume of CO_2 , V_g , that can be trapped in a deep saline aquifer is usually calculated as a fraction of the total available pore volume [Bachu et al., 2007]:

$$V_g = V\phi(1 - S_{wc})\varepsilon, \quad (62)$$

where V is the aquifer volume, ϕ is the porosity, S_{wc} is the connate water saturation, and ε is the efficiency factor. We calculate the efficiency factor using a model for how CO_2 migrates

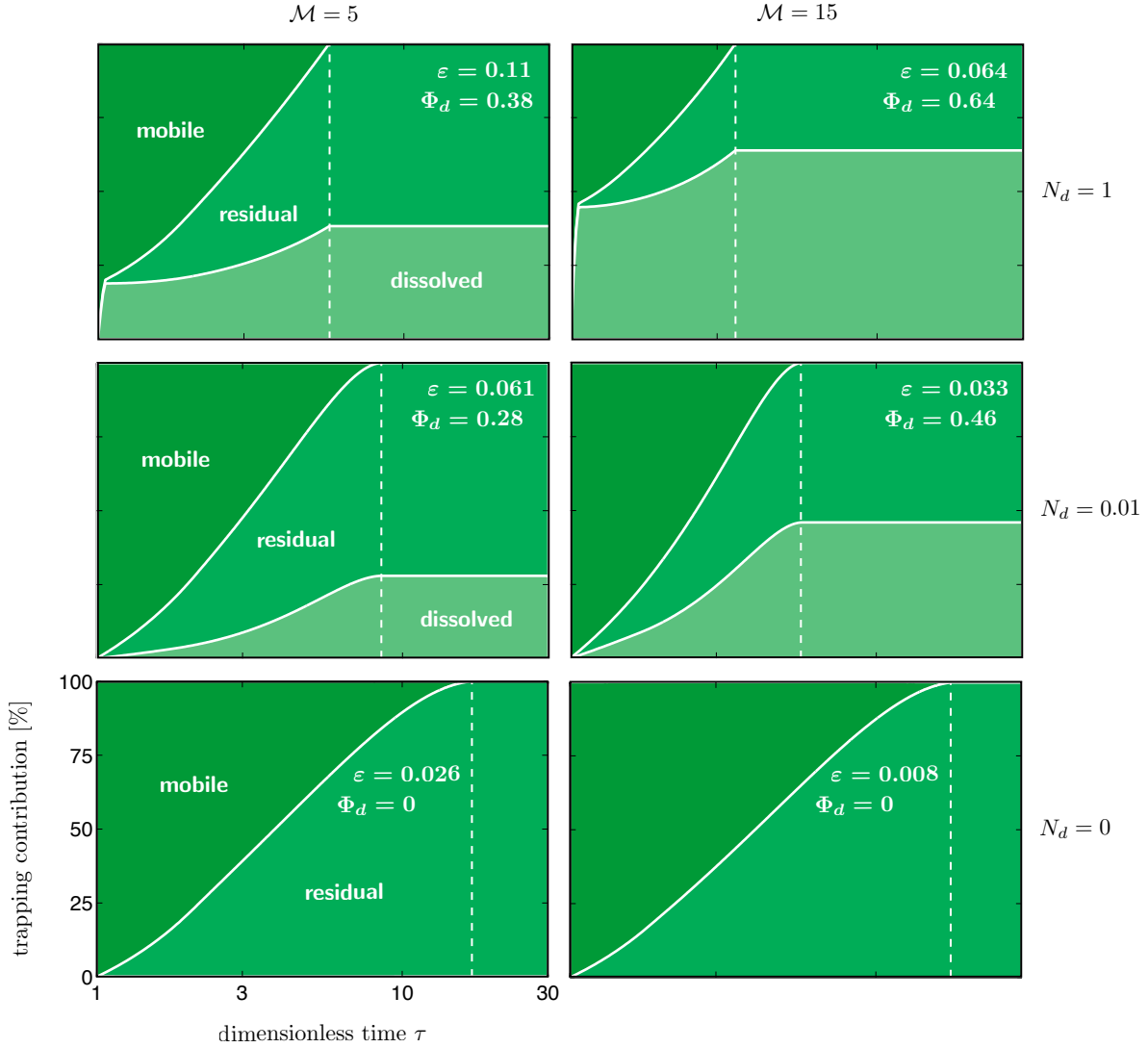


Figure 15: Dissolution is increasingly important as N_d increases, but residual trapping plays an important role even for large N_d . Here, we show the time-evolution of the volume fractions of mobile, residual, and dissolved CO_2 for $N_d = 0, 0.01$, and 1 from bottom to top, respectively, and for $\mathcal{M} = 5$ (left) and 15 (right). The three volume fractions must add to 100% at all times. Residual CO_2 does not dissolve in this model, so the fraction dissolved is constant once all of the CO_2 is trapped. We fix $\Gamma = 0.3$, $N_f = 1$, $N_s = -0.75$, $S_{wc} = 0.4$, $\Gamma_d = 0.06$. As N_d increases, the combination of residual trapping and dissolution traps the plume more quickly (total migration time decreases, as indicated here by the vertical, dashed, white lines), and over a shorter distance (storage efficiency increases). Note that in the instantaneous-saturation limit (top row), the amount of dissolved CO_2 increases sharply at $\tau = 1$ as the water beneath the end-of-injection plume saturates with dissolved CO_2 ; thereafter, dissolution occurs only at the leading edge.

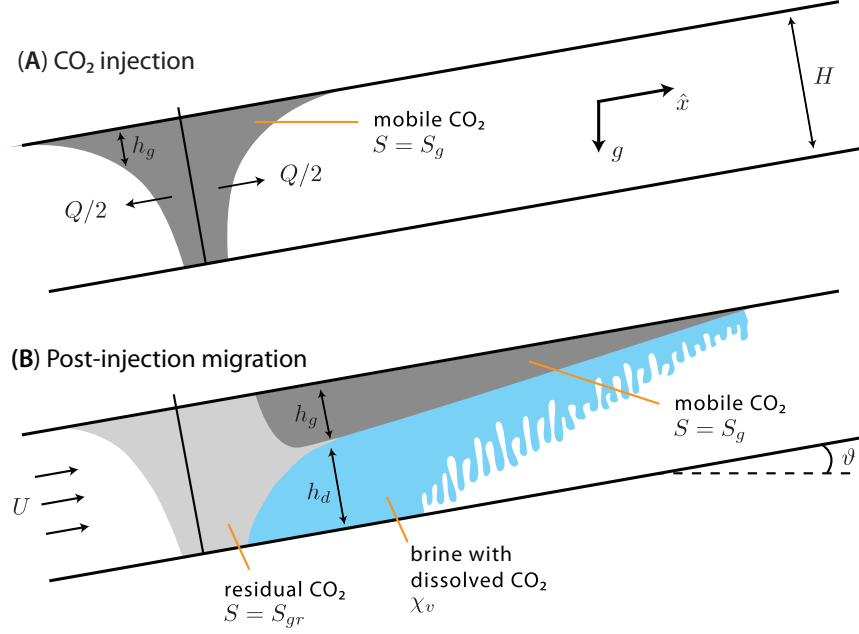


Figure 16: (A) During the injection period, CO₂ enters the aquifer at a high flow rate Q , displacing brine to its connate saturation S_{wc} . Since CO₂ is buoyant and less viscous than the brine, the injected CO₂ forms a gravity tongue [Nordbotten et al., 2006]. No residual trapping occurs since there is little if any imbibition, and solubility trapping is negligible because the injection period is in general much shorter than the time required for dissolution [MacMinn et al., 2010]. (B) Once injection stops, the CO₂ plume migrates away from the well array due to buoyancy and the natural hydraulic gradient. Gravity tonguing becomes more severe, with the plume forming a thin wedge along the bottom of the caprock. At the trailing edge of the plume, CO₂ becomes trapped due to capillarity [Juanes et al., 2006]. Along the bottom of the plume, CO₂ dissolves into the brine via convective mixing [Ennis-King and Paterson, 2005].

through an aquifer and becomes trapped through solubility and capillary trapping [MacMinn et al., 2010]. All parameters in the model are defined in Table 2. The major assumptions in the model are: (1) the interface between the CO₂ and brine is sharp [Bear, 1972; Huppert and Woods, 1995; Nordbotten et al., 2006; Hesse et al., 2008]; (2) capillary pressure effects are negligible; (3) the flow is predominantly horizontal (Dupuit approximation) [Bear, 1972; Yortsos, 1995]; (4) CO₂ leakage through the caprock is negligible; (5) the aquifer is homogeneous, isotropic, and incompressible; (6) the fluids are incompressible and their properties are constant; and (7) during the dissolution of CO₂ into brine, the total fluid volume is conserved.

Injection period. We divide the model into two parts: the injection period and the post-injection period (Fig. 16). During injection, the thickness of the mobile CO₂ plume, h_g , as a function of time, t , and distance along the aquifer, x , is [Nordbotten et al., 2006; Juanes

et al., 2006; MacMinn et al., 2010]:

$$(1 - S_{wc})\phi\partial_t h_g + \partial_x F_g^i = 0, \quad (63)$$

where F_g^i is the flux of CO₂ during injection. Note that the model is one dimensional since we consider injection from a long, line-drive array of wells, as shown in Figure 2. Since the flux of CO₂ due to injection is typically much larger than fluxes due to buoyancy or the natural hydraulic gradient, the flux term is given by

$$F_g^i = \frac{Q}{2W}f, \quad (64)$$

where Q/W is the injection rate per unit width of the injection-well array. The fractional flow function f is given by

$$f = \frac{h_g}{h_g + \mathcal{M}(H - h_g)}, \quad (65)$$

where H is the thickness of the aquifer and \mathcal{M} is the mobility ratio,

$$\mathcal{M} = \frac{\mu_g}{k_{rg}^* \mu_w}. \quad (66)$$

Post-injection period. Once injection stops, the CO₂ plume migrates away from the well array. During migration, it becomes trapped by capillarity at the back of the plume, and by dissolution along the bottom of the plume until the underlying brine is saturated (Fig. 16). To determine when the brine is saturated, we model the transport of dissolved CO₂ in the brine in addition to the migration of the free-phase CO₂ plume.

Plume model. The thickness of the plume, h_g , during post-injection is also governed by a one-dimensional hyperbolic equation:

$$(1 - S_{wc})\phi\tilde{R}\partial_t h_g + \partial_x (F_g^p) = \mathcal{L}, \quad (67)$$

where F_g^p is the CO₂ flux during post-injection. \tilde{R} is a conditional coefficient that accounts for residual trapping:

$$\tilde{R} = \begin{cases} 1 & \text{if } \partial_t h_g > -q_d/\phi, \\ 1 - \Gamma & \text{otherwise,} \end{cases} \quad (68)$$

where Γ is the capillary trapping coefficient, which quantifies the fraction of pore space that will be occupied by residual CO₂:

$$\Gamma = \frac{S_{gr}}{1 - S_{wc}}. \quad (69)$$

q_d is the volumetric flux of CO₂ leaving the plume due to dissolution:

$$q_d = \frac{\alpha\chi_v\phi(\rho_d - \rho_w)gk_{aq}}{\mu_w}, \quad (70)$$

where α is a constant roughly equal to 0.01 [Pau et al., 2010], $\Delta\rho_d$ is the density difference between brine and CO₂-saturated brine, and χ_v is the solubility of CO₂ in brine, expressed

as the volume of free-phase CO₂ that can be dissolved per unit volume of brine saturated with CO₂.

During post-injection, the flux is given by:

$$F_g^p = UHf + \frac{(\rho_b - \rho_g)gk_{aq}k_{gr}^* \sin \vartheta}{\mu_w}(1 - f)h_g, \quad (71)$$

where U is the Darcy velocity of the natural groundwater flow and ϑ is the slope of the caprock. The first term expresses the flux of CO₂ due to the natural hydraulic gradient and the second term expresses the flux due to upslope migration.

The right-hand side of the post-injection model (Eq. 67) is a loss term ($\mathcal{L} < 0$) that accounts for dissolution:

$$\mathcal{L} = \begin{cases} -\tilde{R}(1 - S_{wc})q_d & \text{if } h_d < H - h_g, \\ 0 & \text{otherwise,} \end{cases}$$

where h_d is the effective height of the water column under the plume that is saturated with CO₂. Substituting each of these expressions into Eq. 67 yields the complete CO₂ trapping model:

$$(1 - S_{wc})\tilde{R}\partial_t h_g + \partial_x \left(UHf + \frac{(\rho_w - \rho_g)gk_{aq}k_{gr}^* \sin \vartheta}{\mu_w}(1 - f)h_g \right) = \mathcal{L}. \quad (72)$$

CO₂-saturated-brine model. The model for the migration of CO₂-saturated brine tracks the thickness of the region of brine below the plume that is saturated with CO₂, h_d :

$$\chi_v \phi \partial_t h_d + \chi_v \partial_x F_d^p = -\mathcal{L} - \chi_v S_{wc} \phi \partial_t h_g, \quad (73)$$

where F_d^p is the flux of CO₂-saturated brine. The thickness of the CO₂-saturated region grows as a result of dissolution via the $-\mathcal{L}$ term (recall that $\mathcal{L} < 0$), which previously appeared as a loss term in the CO₂ model.

The flux of CO₂-saturated brine F_d^p may occur due to a natural hydraulic gradient or the slope of the aquifer:

$$F_d^p = UH(1 - f) - \frac{(\rho_g - \rho_w)gk_{aq}k_{gr}^* \sin \vartheta}{\mu_g}(1 - f)h_g. \quad (74)$$

We neglect fluxes that may be caused by the density difference between the brine and CO₂-saturated brine. We also neglect diffusion and dispersion.

Non-dimensional form of the equations. We choose the following non-dimensional variables:

$$\eta_g = h_g/H, \quad \eta_d = h_d/H, \quad \tau = t/T_c, \quad \xi = x/L_c, \quad (75)$$

where $L_c = QT_i/2W(1 - S_{wc})\phi H$, with $T_c = T_i$ being the injection time. With these variables, the injection model (Eq. 63) becomes:

$$\partial_\tau \eta_g + \frac{1}{2} \partial_\xi f = 0. \quad (76)$$

The model for the CO₂ migration during post-injection (Eq. 72) becomes:

$$\tilde{R}' \partial_\tau \eta_g + N_f \partial_\xi f + N_s \partial_\xi [(1-f)\eta_g] = -\tilde{R}' N_d, \quad (77)$$

and the model for the CO₂-saturated brine (Eq. 73) becomes:

$$\tilde{R}' \partial_\tau \eta_d + (1 - S_{wc}) N_f \partial_\xi f_d - (1 - S_{wc}) N_s \partial_\xi (f_d \eta_g) = \tilde{R}' \frac{N_d}{\Gamma_d} - S_{wc} \partial_\tau \eta_g, \quad (78)$$

where:

$$\tilde{R}' = \begin{cases} 1 & \text{if } \partial_\tau \eta_g > -N_d, \\ 1 - \Gamma & \text{otherwise.} \end{cases}$$

and

$$f(\eta_g) = \frac{\mathcal{M} \eta_g}{\mathcal{M} \eta_g + (1 - \eta_g)}, \quad f_d(\eta_g, \eta_d) = \frac{\eta_d}{\mathcal{M} \eta_g + (1 - \eta_g)}.$$

The coefficients in the equations are the flow number, N_f , and the slope number, N_s :

$$N_f = \frac{T_c}{T_i} \frac{2UH}{Q} \quad \text{and} \quad N_s = \frac{T_c}{L_c} \frac{(\rho_w - \rho_g) g k_{aq} k_{gr}^*}{(1 - S_{wc}) \phi \mu_g}, \quad (79)$$

which express the strength of the natural groundwater flow and the aquifer slope in driving plume migration. The dissolution number, N_d , expresses the strength of dissolution:

$$N_d = \begin{cases} \alpha \chi_v \frac{\Delta \rho_a g k_{aq} k_{gr}^* T_c}{H \phi \mu_g} & \text{if } \eta(\xi, \tau) > 0 \text{ and } \eta_d(\xi, \tau) < (1 - \eta(\xi, \tau)), \\ 0 & \text{otherwise.} \end{cases} \quad (80)$$

Migration-limited capacity

In an aquifer, a given volume of injected CO₂ will migrate a particular distance before becoming completely trapped by capillarity and solubility. There is a particular injection volume for which the CO₂ plume will just reach the boundary of the aquifer. We define this volume to be the migration-limited storage capacity. Rearranging the expression for non-dimensional distance ξ (Eq. 75), we obtain a formula for the injected volume $V_i = QT_i$:

$$V_i = xWH\phi(1 - S_{wc}) \frac{2}{\xi}.$$

By setting x to the total length of an aquifer, L_T , ξ to the dimensionless extent of the plume when it is fully trapped, ξ_T , we ensure that this injected volume will just fit in the aquifer. Since the model is one dimensional, we measure the length of an aquifer, L_T , in the direction parallel to migration. We calculate the dimensionless extent of the trapped plume, ξ_T , using the trapping model. To convert volume to mass of CO₂, we multiply by the density of CO₂ in the aquifer, and obtain the final expression for the storage capacity, \mathcal{C}_t :

$$\mathcal{C}_t = \rho_g L_T W H \phi (1 - S_{wc}) \frac{2}{\xi_T}. \quad (81)$$

The expression has the same form as equations commonly used in the literature (Eq. 62), but the efficiency factor $\varepsilon = 2/\xi_T$ can now be calculated explicitly.

To calculate the efficiency factor, we first solve the equation for the injection plume (Eq. 76) analytically using the method of characteristics [Nordbotten et al., 2006; MacMinn et al., 2010]. We use the solution as the initial condition for the equations governing post-injection migration (Eq. 77–78). While these equations can be solved semi-analytically in some limiting cases, we in general solve them numerically using a finite volume method with linear reconstructions and a van Leer limiter, and forward-Euler time stepping [LeVeque, 1992].

3 Application of mathematical models to basins in the continental United States

3.1 Methodology for application of the models

We calculate the storage capacity of eleven deep saline aquifers in the conterminous United States. We select these aquifers on the basis of their (1) size, (2) depth, and (3) structural integrity, and (4) on the availability of data. We select the largest aquifers because our model applies at large lateral length scales and because large aquifers will contribute the most strongly to the nationwide storage capacity. We select aquifers located at depths greater than 800 m to ensure that CO₂ will be stored efficiently as a high-density supercritical fluid. We study aquifers with as few major faults as possible to help reduce the possibility of leakage. While there are likely many deep saline aquifers that meet these criteria, we further restrict our study to those aquifers that have been well characterized and for which the data is publicly available.

Aquifer boundaries. For each aquifer, we use the four criteria stated above—sufficient size, depth, structural integrity, and data—to determine which parts of it are suitable for sequestration. In general, these criteria may be evaluated at a range of length scales. For example, faults and pinchouts in the caprock may occur at scales ranging from the sub-meter scale or less to the regional scale. Since we calculate storage capacity at the basin scale, we evaluate these criteria at the basin scale and assume that small-scale variations will have small impacts on the storage capacity. When one of these criteria is not met at the basin scale, we exclude the appropriate region from our analysis by setting a boundary (Fig. 17).

Some types of boundaries impose boundary conditions in the pressure model (Fig. 17). We set constant pressure boundaries at outcrops. We set no-flow boundaries where the reservoir pinches out between two confining layers, changes to low-permeability rock ($k \leq 10$ millidarcy (mD), 1 darcy= 10^{-12} m²), or becomes cut by basin-scale faults. While faults may be either conductive or sealing, we set them to be no-flow boundaries so that the calculation of pressure-limited capacity is conservative.

Model domains. Within the boundaries of an aquifer, we determine the area over which to apply the trapping model. This region defines the maximum allowable extent of the plume when fully trapped, L_T , and the width of the well array, W . We select model domains in which the aquifer properties exhibit sufficient uniformity for the trapping model to capture basin-scale behavior of the injected CO₂. In addition, we orient the model domains according to the dominant transport direction. If the transport directions are not co-linear, we compare N_s and N_f to determine the dominant process. We evaluate N_s and N_f using values of their parameters averaged over the entire area within the reservoir boundaries. However, if the depth and isopotential contours are very complicated within some part of that area such that transport from ground water flow or up-slope migration can not be approximated as one-dimensional, we exclude that area from our averaging.

Another constraint on the size of a model domain comes from an assumption in the trapping model: since the model assumes that all behavior perpendicular to the well-array









Criterion for suitable aquifers	Feature marked	Boundary condition in pressure model	Symbol
Sufficient data	Limit of available data	no flow	
Aquifer continuity	Reservoir pinchouts	no flow	
	Low-perm. regions	no flow	
Low potential of leakage	Faults	no flow	
	Outcrops	constant pressure	
	Caprock pinchouts	<i>not a pressure boundary</i>	
	High-perm. region in caprock	<i>not a pressure boundary</i>	
Sufficient depth	800m - depth contour	<i>not a pressure boundary</i>	

Figure 17: We exclude portions of an aquifer from our analysis if they do not meet the four criteria in this table. In our geologic maps, we delineate these regions by drawing boundaries. Some of these boundaries impose boundary conditions in the pressure model.

has a negligible or higher-order effect on migration, it rigorously applies to domains in which the ratio of the length parallel to the intended well array to the length parallel to transport is large. While we usually choose domains with an aspect ratio of two or larger, in some cases we use domains that have an aspect ratio closer to one. In these cases, the trapping model predicts a migration distance that is longer than the real migration distance of a given volume of CO₂, since the spread of the real plume parallel to the well array would be important.

In addition to setting the trapping model domain, we set the area over which to apply the pressure model. Since we use the same well array in the pressure model as we do in the trapping model, the widths of these two domains are the same. However, their lengths are often different because not all of the aquifer boundaries correspond to boundary conditions in the pressure model (Fig. 17). This is because regions are not suitable for storing CO₂ may be suitable for “storing” some of the pressure perturbation due to injection. The distances from the well array to the edges of the pressure model domain define the distances to the lateral boundaries in the pressure model, X_l and X_r .

As with the trapping model domains, the pressure-model domains should have large aspect ratios for the pressure model to be strictly valid. However, this is difficult to accomplish in practice, and many of the pressure model domains in this study have aspect ratios near one or less. In these cases, pressure diffusion in the direction parallel to the well array becomes important, resulting in a smaller overpressure at the well array for a given injection scenario compared to the model predictions. Since the model overestimates the pressure rise in these cases, it underestimates the pressure-limited capacity.

Model parameters. Within a model domain, we set the parameters in the models in three ways (Table 2): by using aquifer data directly, by using aquifer data to calculate the parameters, or by estimation. We list the method we use and the value of each parameter in the section describing each aquifer.

We use aquifer data directly to set parameters such as the aquifer depth, thickness, porosity, salinity, and permeability. Since the data often exhibit large uncertainty and variability at the basin scale, we choose representative values. We choose these values to make the storage capacity calculations conservative. For example, if an aquifer exhibits a wide range of porosities, we choose a low value in the range, which will result in a lower trapping-limited storage capacity.

When aquifer data cannot be used directly, we use it to calculate the required parameters. We calculate CO₂ viscosity and density as functions of temperature and pressure Carbon Capture and Sequestration Technologies at MIT. We calculate the temperature in an aquifer, T_{aq} , using the surface temperature, T_s , and the geothermal gradient, G . We calculate the fluid pressure assuming a hydrostatic gradient. Brine density, brine viscosity, and the solubility of CO₂ in brine are functions of salinity in addition to temperature and pressure. While aquifer brines may contain a wide variety of salts, we treat them as consisting of only water and sodium chloride (NaCl), which is by far the dominant salt in nearly every deep saline aquifer Kharaka and Hanor [2007]. We calculate the density and viscosity of brine using correlations based on temperature, pressure, and concentration of sodium chloride Batzle and Wang [1992]. We determine the solubility of CO₂ in brine from published experimental

Table 2: The input parameters used in our models and their symbols.

Parameter [dimensions]	Symbol
Residual CO ₂ saturation [-]	S_{gr}
Connate water saturation [-]	S_{wc}
Endpoint relative permeability to CO ₂ [-]	k_{gr}^*
Coefficient of CO ₂ -saturated-brine flux [-]	α
Compressibility [M ⁻¹ LT ²]	c
Undrained Poisson ratio [-]	ν
Geothermal gradient [ΘL ⁻¹]	G_T
Surface temperature [Θ]	T_s
Depth to top of aquifer [L]	D
Depth from aquifer to bedrock [L]	B
Net aquifer thickness [L]	H
Length of model domain [L]	L_t
Width of well array [L]	W
Porosity [-]	ϕ
Caprock slope [-]	ϑ
Darcy velocity [LT ⁻¹]	U
Aquifer permeability [L ²]	k_{aq}
Caprock permeability [L ²]	$\frac{k_c}{\bar{k}_x}$
Lateral overburden permeability [L ²]	\bar{k}_x
Vertical overburden permeability [L ²]	\bar{k}_z
Salinity [ML ⁻³]	s
CO ₂ solubility [-]	χ_v
Brine density [ML ⁻³]	ρ_w
CO ₂ density [ML ⁻³]	ρ_g
CO ₂ -saturated-brine density [ML ⁻³]	ρ_d
Brine viscosity [ML ⁻¹ T ⁻¹]	μ_w
CO ₂ viscosity [ML ⁻¹ T ⁻¹]	μ_g
Fracture pressure [ML ⁻¹ T ⁻²]	P_{frac}

data for salinities up four molal Duan and Sun [2003] and from a correlation for higher salinities Enick and Scott [1990].

In the trapping model, the relevant measure of CO₂ solubility is the volume of free-phase CO₂ that can be dissolved per unit volume of brine saturated with CO₂. This parameter, χ_v , can be calculated from the solubility in terms of mass fraction, χ_m :

$$\chi_v = \frac{\rho_d}{\rho_g} \chi_m.$$

To calculate the density of CO₂-saturated brine, ρ_d , we use the following formula Bachu [2003b]; Garcia [2001]:

$$\rho_d = \frac{\rho_w}{1 - \chi_m(1 - V_\phi \rho_w^*/M_g)},$$

where M_g is the molar mass of CO₂, ρ_w^* is the density of pure water at aquifer conditions, and V_ϕ is the apparent molar volume of CO₂ in the brine, given by the following correlation Garcia [2001]:

$$V_\phi = 37.51 \times 10^{-6} - (9.585 \times 10^{-8})T_{aq} + (8.740 \times 10^{-10})T_{aq}^2 - (5.044 \times 10^{-13})T_{aq}^3,$$

where T_{aq} is in degrees Celsius and V_ϕ is in m^3/mol .

When there is insufficient data to determine the required parameters, we estimate them. Since little or no data was available for the compressibility of the aquifers and caprocks in this study, we set the average compressibility for every basin to $c = 10^{-10} \text{ Pa}^{-1}$, as has been done in other basin-scale studies Zhou et al. [2008a]. We do not pursue a more rigorous approach because published compressibility data for many types of aquifers and caprocks are equal to within the variability and uncertainty of the data, and also similar to the compressibility of water at the pressure and temperature conditions of deep aquifers. For example, published values for sandstones and limestones generally range from 1×10^{-11} to $1 \times 10^{-10} \text{ Pa}^{-1}$ Wang [2000]; Cheng [2000], while published values for low-porosity shales and mudstones ($\phi < 0.2$) generally range from 1×10^{-11} to $1 \times 10^{-9} \text{ Pa}^{-1}$ Konikow and Neuzil [2007]; Croisé et al. [2004]; Escoffier et al. [2005]; Mishra et al. [2006]. Similarly, we set the Poisson ratio of the aquifers or caprocks to 0.3 in every basin, which is a value characteristic of many sedimentary rocks Wang [2000].

When data on caprock permeability is unavailable, we estimate it to be 0.01 mD Neuzil [1994]; Tokunaga et al. [1998]; Dewhurst et al. [1999]. While rocks deeper than about 3 km can exhibit much lower permeability Neglia [1979], we use this value for all confining units under the assumption that small fractures that are likely widespread at the basin scale will produce effective permeabilities of this order or higher.

Since aquifer-specific data on the multiphase-flow characteristics of CO_2 and brine was also unavailable, we estimate the connate water saturation, residual CO_2 saturation, and the endpoint relative permeability to CO_2 . Based on published data, we take $S_{wc} = 0.4$, $S_{gr} = 0.3$, and $k_{gr}^* = 0.6$ Bennion and Bachu [2008]. These values correspond to $\Gamma = 0.5$.

3.2 Aquifer data

We have identified over ten aquifers in the United States on which to apply the methodology for estimating the CO_2 storage capacity. We have collected the relevant geohydrologic information required to apply the pressure dissipation and CO_2 migration models.

Mt. Simon Sandstone

The Mt. Simon Sandstone is widespread in the Midwestern United States, as shown in Figure 18. It is a transgressive sandstone that consists dominantly of quartz arenite Wickstrom et al. [2005]; Young and Siegel [1992]. Near its base, the formation tends to be conglomeratic with igneous pebbles Willman et al. [1975]; Hovorka et al. [2003c]. Lenses of sandy to silty shale are interbedded in the lower part of the formation in Illinois, and in the upper part of the formation throughout the Midwest [Young and Siegel, 1992, p.B13].

The Mt. Simon Sandstone is overlain by the Eau Claire Formation, which is composed of silty dolomites, dolomitic sandstones, and shale Wickstrom et al. [2005]. This formation has been identified as a regional confining unit by a number of authors O. B. Lloyd and Lyke [1995]; Young and Siegel [1992]; Mandle and Kontis [1992]. The Mt. Simon unconformably overlies Precambrian igneous and metamorphic rocks, which we take as an aquiclude Willman et al. [1975]; Hovorka et al. [2003c].

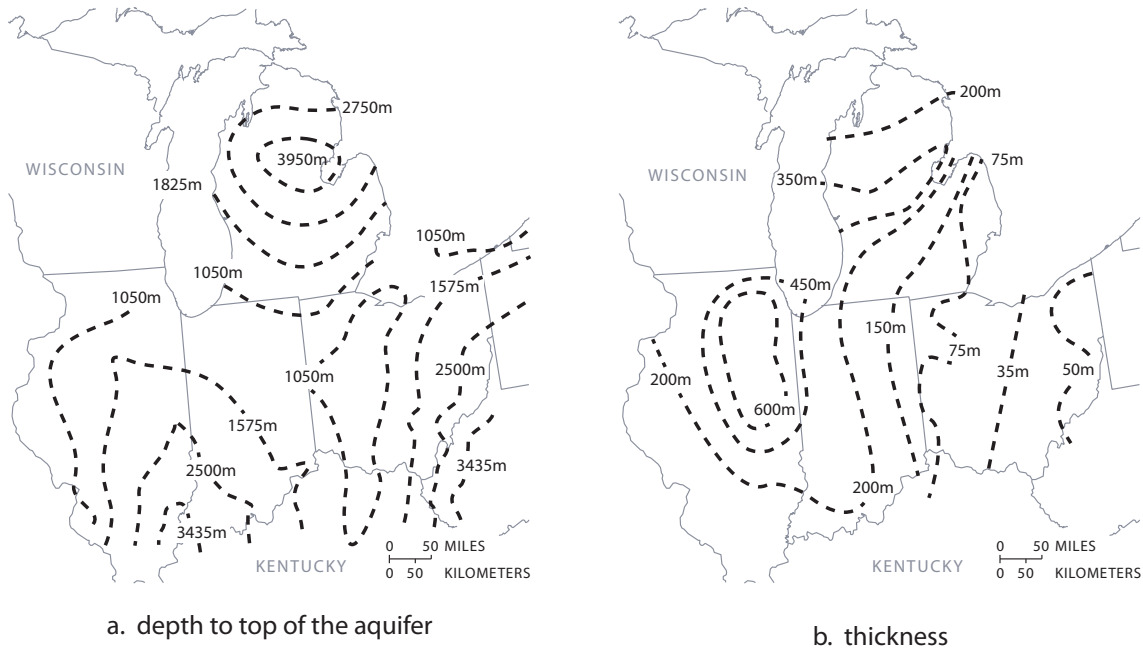


Figure 18: The Mt. Simon Sandstone is widespread in the Midwest. It is deepest and thickest in the centers of the Illinois, Michigan, and Appalachian Basins. (a) Modified from [Wickstrom et al., 2005, Fig.A2-3],[Hovorka et al., 2003a, Map c1mthsimong], and [Barnes et al., 2009, Fig.3]. (b) Modified from [Wickstrom et al., 2005, Fig.A2-2],[Leetaru and McBride, 2009, Fig.2], and [Barnes et al., 2009, Fig.4].

In this study, we model sequestration in deep parts of the formation that lie in the Michigan Basin, Illinois Basin, and the Indiana-Ohio Platform. Within each region, we identify a single model domain, as shown in Figure 19. The data for each domain are shown in Tables 3, 4, and 5.

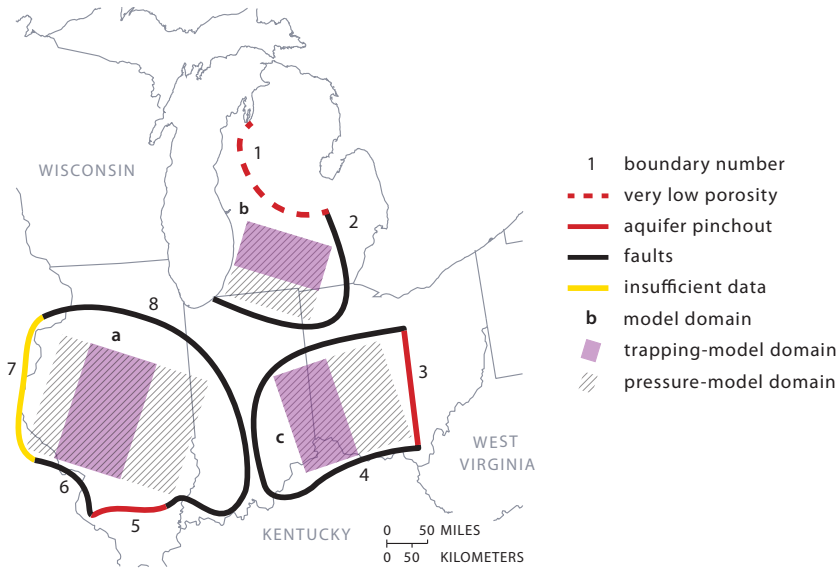


Figure 19: We divide the Mt. Simon Sandstone into regions a, b, and c using eight boundaries. Boundary 1 corresponds to where the porosity becomes very low due to diagenesis ($\phi < 0.1$) Barnes et al. [2009]. Boundary 3 corresponds to where the Mt. Simon Sandstone pinches out into thinner sandstones [Leetaru and McBride, 2009, Fig.2], and Boundary 5 corresponds to where it pinches out between the Precambrian basement and the caprock [Leetaru and McBride, 2009, Fig.2]. Boundary 7 corresponds to the edge of available depth and thickness maps [Hovorka et al., 2003a, Map c1mthsimonag]. Boundaries 2, 4, 6 and 8 correspond to basin-scale faults Wickstrom et al. [2005]; King and Beikman [1974]. Within each region, we set the extent and orientation of the model domains based on the aquifer’s topography since upslope migration is the dominant transport mechanism.

Table 3: Parameters for Region a of the Mt. Simon Sandstone.

Parameter	Symbol	Value	Data Source	Reference
Residual CO ₂ saturation	S_{rg}	0.3	estimated	Bennion and Bachu [2008]; Oak et al. [19]
Connate water saturation	S_{wc}	0.4	estimated	Bennion and Bachu [2008]; Oak et al. [19]
Endpoint relative permeability to CO ₂	k_{rg}^*	0.6	estimated	Bennion and Bachu [2008]; Oak et al. [19]
Coefficient of CO ₂ -saturated-brine flux	α	0.01	estimated	Kneafsey and Pruess [2010a]; Riaz et al. [19]
Compressibility (GPa ⁻¹)	c	0.1	estimated	[Wang, 2000, Table C1]
Undrained Poisson ratio	ν	0.3	estimated	[Wang, 2000, Table C1]
Geothermal gradient (°C/km)	G_T	20	aquifer data	Kron and Heiken [1980]; Nathenson and O'Connell [1990]
Surface temperature (°C)	T_s	10	aquifer data	USs [2010]
Depth to top of aquifer (m)	D	2000	aquifer data	[Hovorka et al., 2003a, Map c1mthsimong]
Depth from aquifer to bedrock (m)	B	0	aquifer data	Wickstrom et al. [2005]
Net aquifer thickness (m)	H	400	aquifer data	[Leetaru and McBride, 2009, Fig.2]
Length of model domain (km)	L_{aq}	100	aquifer data	Fig. 19
Length of pressure domain (km)	L_{pres}	300	aquifer data	Fig. 19
Width of well array (km)	W	200	aquifer data	Fig. 19
Porosity	ϕ	0.2	aquifer data	Leetaru and McBride [2009]
Caprock slope (degrees)	ϑ	0.5	calculated	[Hovorka et al., 2003a, Map c1mthsimong]
Darcy velocity (cm/yr)	U	1	calculated	[Gupta, 1993, Fig.43]
Aquifer permeability (mD)	k_{aq}	100	aquifer data	[Wickstrom et al., 2005, p.57]
Mean vertical permeability (mD)	k_{cap}	0.01	estimated	Neuzil [1994]; Tokunaga et al. [1998]; Devlin et al. [2005]
Lateral overburden permeability (mD)	\bar{k}_x	50	calculated	Fig. 2
Vertical overburden permeability (mD)	\bar{k}_z	0.02	calculated	Fig. 2
Salinity (ppm)	s	100000	aquifer data	MGs [2005]
CO ₂ solubility (volume fraction)	χ_v	0.05	calculated	Duan and Sun [2003]
Brine density (kg/m ³)	ρ_w	1000	calculated	Batzle and Wang [1992]
CO ₂ density (kg/m ³)	ρ_g	700	calculated	Carbon Capture and Sequestration Technology Center [2003]
Brine density change from diss. (kg/m ³)	$\Delta\rho_d$	6	calculated	Garcia [2001]; Bachu and Adams [2003]
Brine viscosity (mPa s)	μ_w	0.8	calculated	Batzle and Wang [1992]
CO ₂ viscosity (mPa s)	μ_g	0.06	calculated	Carbon Capture and Sequestration Technology Center [2003]
Fracture (MPa)	P_{frac}	40	calculated	Eq. 15,14; Zoback and Zoback [1980a]

Table 4: Parameters for Region b of the Mt. Simon Sandstone.

Parameter	Symbol	Value	Data Source	Reference
Residual CO ₂ saturation	S_{rg}	0.3	estimated	Bennion and Bachu [2008]; Oak et al. [1998]
Connate water saturation	S_{wc}	0.4	estimated	Bennion and Bachu [2008]; Oak et al. [1998]
Endpoint relative permeability to CO ₂	k_{rg}^*	0.6	estimated	Bennion and Bachu [2008]; Oak et al. [1998]
Coefficient of CO ₂ -saturated-brine flux	α	0.01	estimated	Kneafsey and Pruess [2010a]
Compressibility (GPa ⁻¹)	c	0.1	estimated	Wang [2000]; Cheng [2000]; Konikow and Pruess [2004]
Undrained Poisson ratio	ν	0.3	estimated	[Wang, 2000, Table C1]
Geothermal gradient (°C/km)	G_T	20	aquifer data	Kron and Heiken [1980]; Nathenson and Coker [1998]
Surface temperature (°C)	T_s	9	aquifer data	USs [2010]
Depth to top of aquifer (m)	D	2000	aquifer data	[Barnes et al., 2009, Fig.4]
Depth from aquifer to bedrock (m)	B	0	aquifer data	Wickstrom et al. [2005]
Net aquifer thickness (m)	H	200	aquifer data	[Barnes et al., 2009, Fig.4]
Length of model domain (km)	L_t	200	aquifer data	Fig. 19
Length of pressure domain (km)	L_{pres}	200	aquifer data	Fig. 19
Width of well array (km)	W	200	aquifer data	Fig. 19
Porosity	ϕ	0.2	aquifer data	Barnes et al. [2009]
Caprock slope (degree)	ϑ	0.7	calculated	[Barnes et al., 2009, Fig.4]
Darcy velocity (cm/yr)	U	1	calculated	[Gupta, 1993, Fig.43]
Aquifer permeability (mD)	k_{aq}	100	aquifer data	[Wickstrom et al., 2005, p.57]
Caprock permeability (mD)	k_c	0.01	estimated	Neuzil [1994]; Tokunaga et al. [1998]; Dewettinck et al. [2000]
Lateral overburden permeability (mD)	\bar{k}_x	50	calculated	Fig. 2
Vertical overburden permeability (mD)	\bar{k}_z	0.02	calculated	Fig. 2
Salinity (g/L)	s	200	aquifer data	[Lampe, 2009, Fig.37]
CO ₂ solubility (volume fraction)	χ_v	0.04	calculated	MacMinn et al. [2011]; Duan and Sun [2002]
Brine density (kg/m ³)	ρ_w	1000	calculated	Batzle and Wang [1992]
CO ₂ density (kg/m ³)	ρ_g	800	calculated	Carbon Capture and Sequestration Technology Center [2009]
Brine density change from diss. (kg/m ³)	$\Delta\rho_d$	8	calculated	Garcia [2001]; Bachu and Adams [2003]
Brine viscosity (mPa s)	μ_w	1	calculated	Batzle and Wang [1992]
CO ₂ viscosity (mPa s)	μ_g	0.07	calculated	Carbon Capture and Sequestration Technology Center [2009]
Fracture pressure (MPa)	P_{frac}	40	calculated	Eq. 15,14; Zoback and Zoback [1980a]

Table 5: Parameters for Region c of the Mt. Simon Sandstone.

Parameter	Symbol	Value	Data Source	Reference
Residual CO ₂ saturation	S_{rg}	0.3	estimated	Bennion and Bachu [2008]; Oak et al. [1998]
Connate water saturation	S_{wc}	0.4	estimated	Bennion and Bachu [2008]; Oak et al. [1998]
Endpoint relative permeability to CO ₂	k_{rg}^*	0.6	estimated	Bennion and Bachu [2008]; Oak et al. [1998]
Coefficient of CO ₂ -saturated-brine flux	α	0.01	estimated	Kneafsey and Pruess [2010a]
Compressibility (GPa ⁻¹)	c	0.1	estimated	Wang [2000]; Cheng [2000]; Konikow and [Wang, 2000, Table C1]
Undrained Poisson ratio	ν	0.3	estimated	[Wang, 2000, Table C1]
Geothermal gradient (°C/km)	G_T	20	aquifer data	Kron and Heiken [1980]; Nathenson and C
Surface temperature (°C)	T_s	10	aquifer data	USs [2010]
Depth to top of aquifer (m)	D	1000	aquifer data	[Hovorka et al., 2003a, Map c1simong]
Depth from aquifer to bedrock (m)	B	0	aquifer data	Wickstrom et al. [2005]
Net aquifer thickness (m)	H	100	aquifer data	[Barnes et al., 2009, Fig.4]
Length of model domain (km)	L_t	300	aquifer data	Fig. 19
Length of pressure domain (km)	L_{pres}	200	aquifer data	Fig. 19
Width of well array (km)	W	200	aquifer data	Fig. 19
Porosity	ϕ	0.2	estimated	Freeze and Cherry [1979]
Caprock slope (degree)	ϑ	0.001	calculated	[Hovorka et al., 2003a, Map c1simong]
Darcy velocity (cm/yr)	U	1	calculated	[Gupta, 1993, Fig.43]
Aquifer permeability (mD)	k_{aq}	100	aquifer data	[Wickstrom et al., 2005, p.57]
Caprock permeability (mD)	k_c	0.01	estimated	Neuzil [1994]; Tokunaga et al. [1998]; Dew
Lateral overburden permeability (mD)	\bar{k}_x	50	calculated	Fig. 2
Vertical overburden permeability (mD)	\bar{k}_z	0.02	calculated	Fig. 2
Salinity (g/L)	s	200	aquifer data	[Lampe, 2009, Fig.37]
CO ₂ solubility (volume fraction)	χ_v	0.04	calculated	MacMinn et al. [2011]; Duan and Sun [200
Brine density (kg/m ³)	ρ_w	1000	calculated	Batzle and Wang [1992]
CO ₂ density (kg/m ³)	ρ_g	700	calculated	Carbon Capture and Sequestration Techn
Brine density change from diss. (kg/m ³)	$\Delta\rho_d$	7	calculated	Garcia [2001]; Bachu and Adams [2003]
Brine viscosity (mPa s)	μ_w	1	calculated	Batzle and Wang [1992]
CO ₂ viscosity (mPa s)	μ_g	0.06	calculated	Carbon Capture and Sequestration Techn
Fracture pressure (MPa)	P_{frac}	20	calculated	Eq. 15,14; Zoback and Zoback [1980a]

Black Warrior River Aquifer

Following previous studies, we model a number of Cretaceous rocks in the southeastern Coastal Plain as a single aquifer called the Black Warrior River Aquifer Miller [1990]; Renken [1996]; Aucott [1996]; Strom and Mallory [1995]. This aquifer begins in central Alabama and Georgia, where it either outcrops or pinches out, and from there it deepens and thickens toward the Gulf of Mexico. In Alabama and northwestern Florida, it consists of rocks in the Eutaw and McShan Formations and the Tuscaloosa Group. In Georgia and northeastern Florida, it consists of rocks in the Eutaw Formation, Tuscaloosa Formation, and the Atkinson Formation [Miller, 1990, Fig.72]. These rocks are mostly sandstone interbedded with siltstone, shale, and mudstone Miller [1990]; Renken [1996]; Strom and Mallory [1995]. They were deposited in a variety of settings, including fluvial, deltaic, and marine environments.

A variety of rocks underlie the aquifer. These rocks include Precambrian crystalline rocks, Paleozoic and Mesozoic sedimentary rocks, and Lower Mesozoic redbeds and diabase [Miller, 1990, Fig.76]. While some of these rocks are porous and permeable, we do not model them

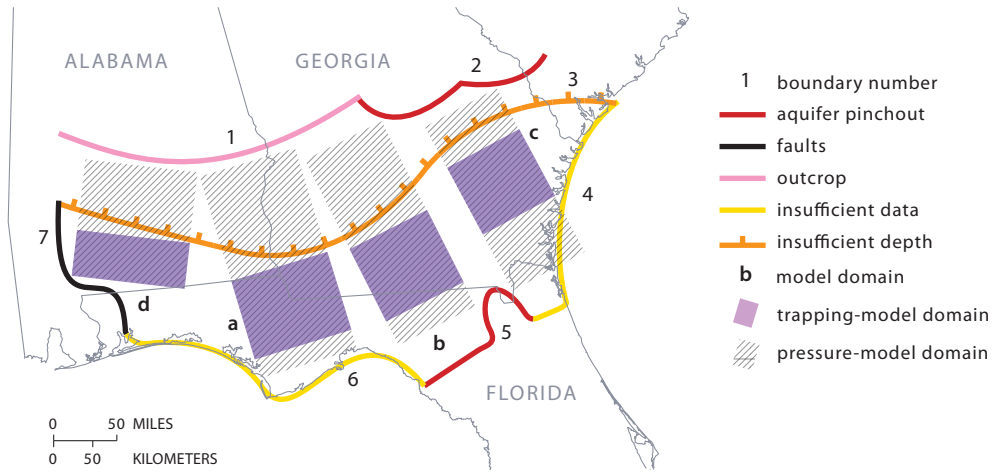


Figure 20: We identify seven boundaries that constrain the portion of the Black Warrior River Aquifer that is suitable for sequestration. Boundary 1 corresponds to where the aquifer crops out in central Alabama and Georgia [Miller, 1990, Fig.79]. Boundary 2 corresponds to where it pinches out between the overlying Chattahoochee River Aquifer and underlying low-permeability rocks Miller [1990]. Boundary 3 marks where the aquifer becomes shallower than 800m [Miller, 1990, Fig.79]. Boundaries 4 and 6 correspond to edge of available depth maps Miller [1990]; Renken [1996]; Applin and Applin [1967]. Boundary 5 shows where the aquifer pinches out or becomes very thin [Applin and Applin, 1967, Plate 3A]. Finally, Boundary 7 corresponds to where the aquifer becomes offset by a fault system by up to hundreds of meters. Within these boundaries, we identify four regions in which to apply our models (Regions a, b, c, and d).

because they are very poorly characterized. The aquifer is overlain by the Selma Group, which consists mostly of chalk and is recognized by many authors as a regional aquitard Miller [1990]; Renken [1996]; Strom and Mallory [1995].

A variety of geologic features constrain the region of the Black Warrior River Aquifer that is suitable for sequestration, as shown in Figure 20. Within this region, we identify four model domains, also shown in Figure 20. The data for each domain are shown in Tables 6, 7, 8, and 9.

Table 6: Parameters for Region a of the Black Warrior River Aquifer.

Parameter	Symbol	Value	Data Source	Reference
Residual CO ₂ saturation	S_{rg}	0.3	estimated	Bennion and Bachu [2008]; Oak et al. [1998]
Connate water saturation	S_{wc}	0.4	estimated	Bennion and Bachu [2008]; Oak et al. [1998]
Endpoint relative permeability to CO ₂	k_{rg}^*	0.6	estimated	Bennion and Bachu [2008]; Oak et al. [1998]
Coefficient of CO ₂ -saturated-brine flux	α	0.01	estimated	Kneafsey and Pruess [2010a]; Riaz et al. [2007]
Compressibility (GPa ⁻¹)	c	0.1	estimated	[Wang, 2000, Table C1]
Undrained Poisson ratio	ν	0.3	estimated	[Wang, 2000, Table C1]
Geothermal gradient (°C/km)	G_T	30	aquifer data	Kron and Heiken [1980]; Nathenson and C
Surface temperature (°C)	T_s	20	aquifer data	USs [2010]
Depth to top of aquifer (m)	D	1000	aquifer data	[Renken, 1996, Plate41],National Imagery
Depth from aquifer to bedrock (m)	B	0	aquifer data	[Miller, 1990, Fig.76]
Net aquifer thickness (m)	H	1000	aquifer data	[Renken, 1996, Plate 42]
Length of model domain (km)	L_T	100	aquifer data	Fig. 20
Length of pressure domain (km)	L_{press}	300	aquifer data	Fig. 20
Width of well array (km)	W	100	aquifer data	Fig. 20
Porosity	ϕ	0.2	estimated	Freeze and Cherry [1979]
Caprock slope (degrees)	ϑ	0.5	calculated	[Renken, 1996, Plate41]
Darcy velocity (cm/yr)	U	1 ^a	calculated	[Lee, 1994, p.D68]
Aquifer permeability (mD)	k_{aq}	100 ^b	aquifer data	[Barker and Pernik, 1994, Fig.30C][Renke
Mean vertical permeability (mD)	k_{cap}	0.01	aquifer data	Sadler et al. [1992]
Lateral overburden permeability (mD)	\bar{k}_x	50	calculated	Fig. 2
Vertical overburden permeability (mD)	\bar{k}_z	0.02	calculated	Fig. 2
Salinity (g/L)	s	100	aquifer data	[Lee, 1985, Plate 2]
CO ₂ solubility (volume fraction)	χ_v	0.05	calculated	Duan and Sun [2003]
Brine density (kg/m ³)	ρ_w	1000	calculated	Batzle and Wang [1992]
CO ₂ density (kg/m ³)	ρ_g	700	calculated	Carbon Capture and Sequestration Techn
Brine density change from diss. (kg/m ³)	$\Delta\rho_d$	8	calculated	Garcia [2001]; Bachu and Adams [2003]
Brine viscosity (mPa s)	μ_w	0.8	calculated	Batzle and Wang [1992]
CO ₂ viscosity (mPa s)	μ_g	0.05	calculated	Carbon Capture and Sequestration Techn
Fracture pressure (MPa)	P_{frac}	20	calculated	Eq. 15,14; Zoback and Zoback [1980a]

^a There are no data available to calculate the Darcy velocity in the deep Black Warrior River Aquifer. In the shallow aquifer about 10 cm/yr have been estimated using simulations and isotopic data [Lee, 1994, p.D68]. However, the region suitable for storage is more than 100 km south of where the data were taken and more than 750 m deeper. Since velocity generally decreases with distance from recharge sources, I arbitrarily lower the shallow aquifer velocity by a factor of 10. The resulting value is commensurate with other deep saline aquifers such as the Mt. Simon Sandstone.

^b Calculated from mapped values of transmissivity between 80 and 399 m²/day [Barker and Pernik, 1994, Fig.30C] and aquifer thickness [Renken, 1996, Plate 42].

Table 7: Parameters for Region b of the Black Warrior River Aquifer.

Parameter	Symbol	Value	Data Source	Reference
Residual CO ₂ saturation	S_{rg}	0.3	estimated	Bennion and Bachu [2008]; Oak et al. [1998]
Connate water saturation	S_{wc}	0.4	estimated	Bennion and Bachu [2008]; Oak et al. [1998]
Endpoint relative permeability to CO ₂	k_{rg}^*	0.6	estimated	Bennion and Bachu [2008]; Oak et al. [1998]
Coefficient of CO ₂ -saturated-brine flux	α	0.01	estimated	Kneafsey and Pruess [2010a]; Riaz et al. [2007]
Compressibility (GPa ⁻¹)	c	0.1	estimated	[Wang, 2000, Table C1]
Undrained Poisson ratio	ν	0.3	estimated	[Wang, 2000, Table C1]
Geothermal gradient (°C/km)	G_T	20	aquifer data	Kron and Heiken [1980]; Nathenson and C
Surface temperature (°C)	T_s	20	aquifer data	USs [2010]
Depth to top of aquifer (m)	D	100	aquifer data	[Renken, 1996, Plate41],National Imagery
Depth from aquifer to bedrock (m)	B	0	aquifer data	[Miller, 1990, Fig.76]
Net aquifer thickness (m)	H	300	aquifer data	[Renken, 1996, Plate 42]
Length of model domain (km)	L_T	100	aquifer data	Fig. 20
Length of pressure domain (km)	L_{pres}	300	aquifer data	Fig. 20
Width of well array (km)	W	100	aquifer data	Fig. 20
Porosity	ϕ	0.2	estimated	Freeze and Cherry [1979]
Caprock slope (degrees)	ϑ	0.2	calculated	[Renken, 1996, Plate41]
Darcy velocity (cm/yr)	U	1 ^a	calculated	[Lee, 1994, p.D68]
Aquifer permeability (mD)	k_{aq}	400 ^b	aquifer data	[Barker and Pernik, 1994, Fig.30C][Renke
Mean vertical permeability (mD)	k_{cap}	0.01	aquifer data	Sadler et al. [1992]
Lateral overburden permeability (mD)	\bar{k}_x	200	calculated	Fig. 2
Vertical overburden permeability (mD)	\bar{k}_z	0.02	calculated	Fig. 2
Salinity (g/L)	s	10	aquifer data	[Lee, 1985, Plate 2]
CO ₂ solubility (volume fraction)	χ_v	0.07	calculated	Duan and Sun [2003]
Brine density (kg/m ³)	ρ_w	1000	calculated	Batzle and Wang [1992]
CO ₂ density (kg/m ³)	ρ_g	700	calculated	Carbon Capture and Sequestration Techn
Brine density change from diss. (kg/m ³)	$\Delta\rho_d$	10	calculated	Garcia [2001]; Bachu and Adams [2003]
Brine viscosity (mPa s)	μ_w	0.7	calculated	Batzle and Wang [1992]
CO ₂ viscosity (mPa s)	μ_g	0.06	calculated	Carbon Capture and Sequestration Techn
Fracture pressure (MPa)	P_{frac}	10	calculated	Eq. 15,14; Zoback and Zoback [1980a]

^a There are no data available to calculate the Darcy velocity in the deep Black Warrior River Aquifer. In the shallow aquifer about 10 cm/yr have been estimated using simulations and isotopic data [Lee, 1994, p.D68]. However, the region suitable for storage is more than 100 km south of where the data were taken and more than 750 m deeper. Since velocity generally decreases with distance from recharge sources, I arbitrarily lower the shallow aquifer velocity by a factor of 10. The resulting value is commensurate with other deep saline aquifers such as the Mt. Simon Sandstone.

^b Calculated from mapped values of transmissivity between 80 and 399 m²/day [Barker and Pernik, 1994, Fig.30C] and aquifer thickness [Renken, 1996, Plate 42].

Table 8: Parameters for Region c of the Black Warrior River Aquifer.

Parameter	Symbol	Value	Data Source	Reference
Residual CO ₂ saturation	S_{rg}	0.3	estimated	Bennion and Bachu [2008]; Oak et al. [1998]
Connate water saturation	S_{wc}	0.4	estimated	Bennion and Bachu [2008]; Oak et al. [1998]
Endpoint relative permeability to CO ₂	k_{rg}^*	0.6	estimated	Bennion and Bachu [2008]; Oak et al. [1998]
Coefficient of CO ₂ -saturated-brine flux	α	0.01	estimated	Kneafsey and Pruess [2010a]; Riaz et al. [2007]
Compressibility (GPa ⁻¹)	c	0.1	estimated	[Wang, 2000, Table C1]
Undrained Poisson ratio	ν	0.3	estimated	[Wang, 2000, Table C1]
Geothermal gradient (°C/km)	G_T	20	aquifer data	Kron and Heiken [1980]; Nathenson and C
Surface temperature (°C)	T_s	20	aquifer data	USs [2010]
Depth to top of aquifer (m)	D	1000	aquifer data	[Renken, 1996, Plate41],National Imagery
Depth from aquifer to bedrock (m)	B	0	aquifer data	[Miller, 1990, Fig.76]
Net aquifer thickness (m)	H	200	aquifer data	[Renken, 1996, Plate 42]
Length of model domain (km)	L_T	90	aquifer data	Fig. 20
Length of pressure domain (km)	L_{pres}	200	aquifer data	Fig. 20
Width of well array (km)	W	100	aquifer data	Fig. 20
Porosity	ϕ	0.2	estimated	Freeze and Cherry [1979]
Caprock slope (degrees)	ϑ	0.2	calculated	[Renken, 1996, Plate41]
Darcy velocity (cm/yr)	U	1 ^a	calculated	[Lee, 1994, p.D68]
Aquifer permeability (mD)	k_{aq}	900 ^b	aquifer data	[Barker and Pernik, 1994, Fig.30C][Renke
Mean vertical permeability (mD)	k_{cap}	0.01	aquifer data	Sadler et al. [1992]
Lateral overburden permeability (mD)	\bar{k}_x	500	calculated	Fig. 2
Vertical overburden permeability (mD)	\bar{k}_z	0.02	calculated	Fig. 2
Salinity (g/L)	s	10	aquifer data	[Lee, 1985, Plate 2]
CO ₂ solubility (volume fraction)	χ_v	0.07	calculated	Duan and Sun [2003]
Brine density (kg/m ³)	ρ_w	1000	calculated	Batzle and Wang [1992]
CO ₂ density (kg/m ³)	ρ_g	700	calculated	Carbon Capture and Sequestration Techn
Brine density change from diss. (kg/m ³)	$\Delta\rho_d$	10	calculated	Garcia [2001]; Bachu and Adams [2003]
Brine viscosity (mPa s)	μ_w	0.7	calculated	Batzle and Wang [1992]
CO ₂ viscosity (mPa s)	μ_g	0.06	calculated	Carbon Capture and Sequestration Techn
Fracture pressure (MPa)	P_{frac}	20	calculated	Eq. 15,14; Zoback and Zoback [1980a]

^a There are no data available to calculate the Darcy velocity in the deep Black Warrior River Aquifer. In the shallow aquifer about 10 cm/yr have been estimated using simulations and isotopic data [Lee, 1994, p.D68]. However, the region suitable for storage is more than 100 km south of where the data were taken and more than 750 m deeper. Since velocity generally decreases with distance from recharge sources, I arbitrarily lower the shallow aquifer velocity by a factor of 10. The resulting value is commensurate with other deep saline aquifers such as the Mt. Simon Sandstone.

^b Calculated from mapped values of transmissivity between 80 and 399 m²/day [Barker and Pernik, 1994, Fig.30C] and aquifer thickness [Renken, 1996, Plate 42].

Table 9: Parameters for Region d of the Black Warrior River Aquifer.

Parameter	Symbol	Value	Data Source	Reference
Residual CO ₂ saturation	S_{rg}	0.3	estimated	Bennion and Bachu [2008]; Oak et al. [1998]
Connate water saturation	S_{wc}	0.4	estimated	Bennion and Bachu [2008]; Oak et al. [1998]
Endpoint relative permeability to CO ₂	k_{rg}^*	0.6	estimated	Bennion and Bachu [2008]; Oak et al. [1998]
Coefficient of CO ₂ -saturated-brine flux	α	0.01	estimated	Kneafsey and Pruess [2010a]; Riaz et al. [2007]
Compressibility (GPa ⁻¹)	c	0.1	estimated	[Wang, 2000, Table C1]
Undrained Poisson ratio	ν	0.3	estimated	[Wang, 2000, Table C1]
Geothermal gradient (°C/km)	G_T	30	aquifer data	Kron and Heiken [1980]; Nathenson and C
Surface temperature (°C)	T_s	20	aquifer data	USs [2010]
Depth to top of aquifer (m)	D	1000	aquifer data	[Renken, 1996, Plate41],National Imagery
Depth from aquifer to bedrock (m)	B	0	aquifer data	[Miller, 1990, Fig.76]
Net aquifer thickness (m)	H	2000	aquifer data	[Renken, 1996, Plate 42]
Length of model domain (km)	L_T	60	aquifer data	Fig. 20
Length of pressure domain (km)	L_{pres}	100	aquifer data	Fig. 20
Width of well array (km)	W	100	aquifer data	Fig. 20
Porosity	ϕ	0.2	estimated	Freeze and Cherry [1979]
Caprock slope (degrees)	ϑ	0.6	calculated	[Renken, 1996, Plate41]
Darcy velocity (cm/yr)	U	1 ^a	calculated	[Lee, 1994, p.D68]
Aquifer permeability (mD)	k_{aq}	60 ^b	aquifer data	[Barker and Pernik, 1994, Fig.30C][Renke
Mean vertical permeability (mD)	k_{cap}	0.01	aquifer data	Sadler et al. [1992]
Lateral overburden permeability (mD)	\bar{k}_x	30	calculated	Fig. 2
Vertical overburden permeability (mD)	\bar{k}_z	0.02	calculated	Fig. 2
Salinity (g/L)	s	80	aquifer data	[Lee, 1985, Plate 2]
CO ₂ solubility (volume fraction)	χ_v	0.06	calculated	Duan and Sun [2003]
Brine density (kg/m ³)	ρ_w	1000	calculated	Batzle and Wang [1992]
CO ₂ density (kg/m ³)	ρ_g	700	calculated	Carbon Capture and Sequestration Techn
Brine density change from diss. (kg/m ³)	$\Delta\rho_d$	9	calculated	Garcia [2001]; Bachu and Adams [2003]
Brine viscosity (mPa s)	μ_w	0.7	calculated	Batzle and Wang [1992]
CO ₂ viscosity (mPa s)	μ_g	0.05	calculated	Carbon Capture and Sequestration Techn
Fracture pressure (MPa)	P_{frac}	20	calculated	Eq. 15,14; Zoback and Zoback [1980a]

^a There are no data available to calculate the Darcy velocity in the deep Black Warrior River Aquifer. In the shallow aquifer about 10 cm/yr have been estimated using simulations and isotopic data [Lee, 1994, p.D68]. However, the region suitable for storage is more than 100 km south of where the data were taken and more than 750 m deeper. Since velocity generally decreases with distance from recharge sources, I arbitrarily lower the shallow aquifer velocity by a factor of 10. The resulting value is commensurate with other deep saline aquifers such as the Mt. Simon Sandstone.

^b Calculated from mapped values of transmissivity between 80 and 399 m²/day [Barker and Pernik, 1994, Fig.30C] and aquifer thickness [Renken, 1996, Plate 42].

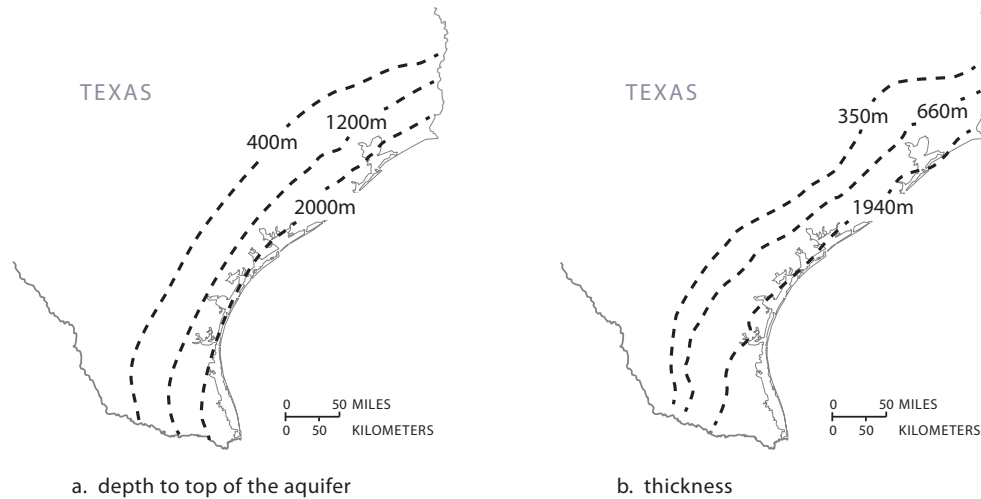


Figure 21: The Frio Formation is located on the east coast of Texas. It dips and thickens toward the coast. (a) Modified from [Hovorka et al., 2003a, Map c1friog1]. (b) Modified from [Hovorka et al., 2003a, Map c4friog].

Frio Formation

The Frio Formation occurs in the Gulf Basin in Texas. Starting at outcrops about 150km inland from the coast, it dips and thickens uniformly toward the coast as shown in Figure 21, reaching depths of more than 3000m below sea level [Hovorka, 1999, p.21].

The Frio Formation is highly heterogeneous, consisting of interfingering marine and non-marine sands and shales Galloway et al. [1982]. These sediments occur in a variety of facies such as deltaic and fluvial facies Hovorka et al. [2001]. The Frio Formation is overlain by the Anuhac Formation and underlain by the Vicksburg Group and Jackson Group. These units are composed dominantly of clay and form an effective aquitard and aquiclude Ryder and Ardis [1991].

We model sequestration in a broad region of the Frio Formation along the Texas coast, as shown in Figure 22. Within this region, we identify three regions in which to apply our models (Regions a, b, and c). The data for each region are shown in Tables 10, 11, and 12.

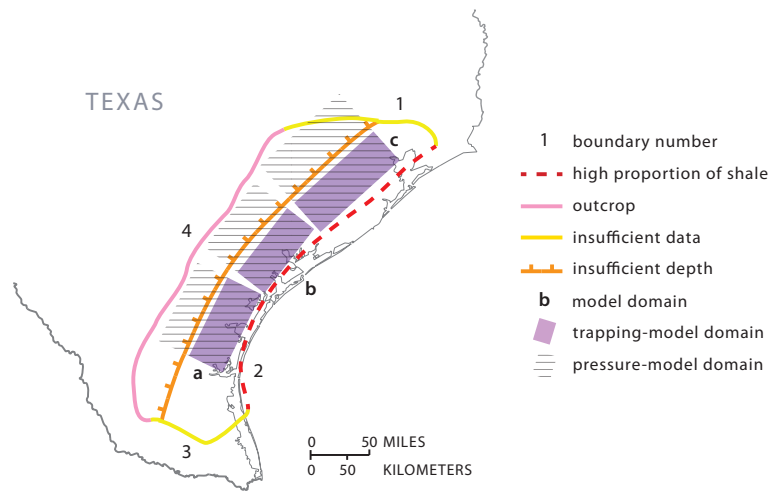


Figure 22: We identify four boundaries that constrain the portion of the Frio Formation that is suitable for sequestration. Boundaries 1 and 3 correspond to the edges of available depth and thickness maps Hovorka et al. [2003a]. Boundary 2 corresponds to where the proportion of shale in the formation becomes greater than 80% [Hovorka et al., 2003a, Map 5frio]. Boundary 4 corresponds to outcrops Hovorka et al. [2003a]. Within these boundaries, we identify three regions in which to apply our models (Regions a, b, and c).

Table 10: Parameters for Region a of the Frio Formation.

Parameter	Symbol	Value	Data Source	Reference
Residual CO ₂ saturation	S_{rg}	0.3	estimated	Bennion and Bachu [2008]; Oak et al. [1998]
Connate water saturation	S_{wc}	0.4	estimated	Bennion and Bachu [2008]; Oak et al. [1998]
Endpoint relative permeability to CO ₂	k_{rg}^*	0.6	estimated	Bennion and Bachu [2008]; Oak et al. [1998]
Coefficient of CO ₂ -saturated-brine flux	α	0.01	estimated	Kneafsey and Pruess [2010a]; Riaz et al. [2007]
Compressibility (GPa ⁻¹)	c	0.1	estimated	[Wang, 2000, Table C1]
Undrained Poisson ratio	ν	0.3	estimated	[Wang, 2000, Table C1]
Geothermal gradient (°C/km)	G_T	30	aquifer data	Kron and Heiken [1980]; Nathenson and C
Surface temperature (°C)	T_s	20	aquifer data	USs [2010]
Depth to top of aquifer (m)	D	1000	aquifer data	[Hovorka et al., 2003a, Map c1friog1]
Depth from aquifer to bedrock (m)	B	10000	aquifer data	Frezon et al. [1983]
Net aquifer thickness (m)	H	2000	aquifer data	[Hovorka et al., 2003a, Map c3friog]
Length of model domain (km)	L_T	50	aquifer data	Fig. 22
Length of pressure domain (km)	L_{pres}	100	aquifer data	Fig. 22
Width of well array (km)	W	100	aquifer data	Fig. 22
Porosity	ϕ	0.2	aquifer data	[Loucks et al., 1984, Fig.10]
Caprock slope (degrees)	ϑ	2	calculated	[Galloway et al., 1982, Fig.2]
Darcy velocity (cm/yr)	U	10 ^a	calculated	Kreitler et al. [1990]
Aquifer permeability (mD)	k_{aq}	400	aquifer data	[Loucks et al., 1984, Fig.8]
Mean vertical permeability (mD)	k_{cap}	0.01	estimated	Neuzil [1994]; Tokunaga et al. [1998]; Dew
Lateral overburden permeability (mD)	\bar{k}_x	200	calculated	Fig. 2
Vertical overburden permeability (mD)	\bar{k}_z	0.02	calculated	Fig. 2
Salinity (g/L)	s	50	aquifer data	[Morton and Land, 1987, Fig.2A]
CO ₂ solubility (volume fraction)	χ_v	0.07	calculated	Duan and Sun [2003]
Brine density (kg/m ³)	ρ_w	1000	calculated	Batzle and Wang [1992]
CO ₂ density (kg/m ³)	ρ_g	500	calculated	Carbon Capture and Sequestration Techn
Brine density change from diss. (kg/m ³)	$\Delta\rho_d$	8	calculated	Garcia [2001]; Bachu and Adams [2003]
Brine viscosity (mPa s)	μ_w	0.8	calculated	Batzle and Wang [1992]
CO ₂ viscosity (mPa s)	μ_g	0.04	calculated	Carbon Capture and Sequestration Techn
Fracture pressure (MPa)	P_{frac}	20	calculated	Eq. 15,14; Zoback and Zoback [1980a]

^a We set the Darcy velocity to 10 cm/yr based on reported ranges for the velocity Kreitler et al. [1990] and values in other o

Table 11: Parameters for Region b of the Frio Formation.

Parameter	Symbol	Value	Data Source	Reference
Residual CO ₂ saturation	S_{rg}	0.3	estimated	Bennion and Bachu [2008]; Oak et al. [1998]
Connate water saturation	S_{wc}	0.4	estimated	Bennion and Bachu [2008]; Oak et al. [1998]
Endpoint relative permeability to CO ₂	k_{rg}^*	0.6	estimated	Bennion and Bachu [2008]; Oak et al. [1998]
Coefficient of CO ₂ -saturated-brine flux	α	0.01	estimated	Kneafsey and Pruess [2010a]; Riaz et al. [2004]
Compressibility (GPa ⁻¹)	c	0.1	estimated	[Wang, 2000, Table C1]
Undrained Poisson ratio	ν	0.3	estimated	[Wang, 2000, Table C1]
Geothermal gradient (°C/km)	G_T	30	aquifer data	Kron and Heiken [1980]; Nathenson and C
Surface temperature (°C)	T_s	20	aquifer data	USs [2010]
Depth to top of aquifer (m)	D	1000	aquifer data	[Hovorka et al., 2003a, Map c1friog1]
Depth from aquifer to bedrock (m)	B	10000	aquifer data	Frezon et al. [1983]
Net aquifer thickness (m)	H	900	aquifer data	[Hovorka et al., 2003a, Map c3friog]
Length of model domain (km)	L_T	40	aquifer data	Fig. 22
Length of pressure domain (km)	L_{pres}	100	aquifer data	Fig. 22
Width of well array (km)	W	100	aquifer data	Fig. 22
Porosity	ϕ	0.2	aquifer data	[Loucks et al., 1984, Fig.10]
Caprock slope (degrees)	ϑ	2	calculated	[Galloway et al., 1982, Fig.2]
Darcy velocity (cm/yr)	U	10 ^a	calculated	Kreitler et al. [1990]
Aquifer permeability (mD)	k_{aq}	400	aquifer data	[Loucks et al., 1984, Fig.8]
Mean vertical permeability (mD)	k_{cap}	0.01	estimated	Neuzil [1994]; Tokunaga et al. [1998]; Dew
Lateral overburden permeability (mD)	\bar{k}_x	200	calculated	Fig. 2
Vertical overburden permeability (mD)	\bar{k}_z	0.02	calculated	Fig. 2
Salinity (g/L)	s	50	aquifer data	[Morton and Land, 1987, Fig.2A]
CO ₂ solubility (volume fraction)	χ_v	0.08	calculated	Duan and Sun [2003]
Brine density (kg/m ³)	ρ_w	1000	calculated	Batzle and Wang [1992]
CO ₂ density (kg/m ³)	ρ_g	500	calculated	Carbon Capture and Sequestration Techn
Brine density change from diss. (kg/m ³)	$\Delta\rho_d$	8	calculated	Garcia [2001]; Bachu and Adams [2003]
Brine viscosity (mPa s)	μ_w	0.6	calculated	Batzle and Wang [1992]
CO ₂ viscosity (mPa s)	μ_g	0.04	calculated	Carbon Capture and Sequestration Techn
Fracture pressure (MPa)	P_{frac}	20	calculated	Eq. 15,14; Zoback and Zoback [1980a]

^a We set the Darcy velocity to 10 cm/yr based on reported ranges for the velocity Kreitler et al. [1990] and values in other c

Table 12: Parameters for Region c of the Frio Formation.

Parameter	Symbol	Value	Data Source	Reference
Residual CO ₂ saturation	S_{rg}	0.3	estimated	Bennion and Bachu [2008]; Oak et al. [1998]
Connate water saturation	S_{wc}	0.4	estimated	Bennion and Bachu [2008]; Oak et al. [1998]
Endpoint relative permeability to CO ₂	k_{rg}^*	0.6	estimated	Bennion and Bachu [2008]; Oak et al. [1998]
Coefficient of CO ₂ -saturated-brine flux	α	0.01	estimated	Kneafsey and Pruess [2010a]; Riaz et al. [2004]
Compressibility (GPa ⁻¹)	c	0.1	estimated	[Wang, 2000, Table C1]
Undrained Poisson ratio	ν	0.3	estimated	[Wang, 2000, Table C1]
Geothermal gradient (°C/km)	G_T	30	aquifer data	Kron and Heiken [1980]; Nathenson and C
Surface temperature (°C)	T_s	20	aquifer data	USs [2010]
Depth to top of aquifer (m)	D	1000	aquifer data	[Hovorka et al., 2003a, Map c1friog1]
Depth from aquifer to bedrock (m)	B	10000	aquifer data	Frezon et al. [1983]
Net aquifer thickness (m)	H	700	aquifer data	[Hovorka et al., 2003a, Map c3friog]
Length of model domain (km)	L_T	50	aquifer data	Fig. 22
Length of pressure domain (km)	L_{pres}	100	aquifer data	Fig. 22
Width of well array (km)	W	100	aquifer data	Fig. 22
Porosity	ϕ	0.2	aquifer data	[Loucks et al., 1984, Fig.10]
Caprock slope (degrees)	ϑ	6	calculated	[Galloway et al., 1982, Fig.2]
Darcy velocity (cm/yr)	U	10 ^a	calculated	Kreitler et al. [1990]
Aquifer permeability (mD)	k_{aq}	400	aquifer data	[Loucks et al., 1984, Fig.8]
Mean vertical permeability (mD)	k_{cap}	0.01	estimated	Neuzil [1994]; Tokunaga et al. [1998]; Dew
Lateral overburden permeability (mD)	\bar{k}_x	200	calculated	Fig. 2
Vertical overburden permeability (mD)	\bar{k}_z	0.02	calculated	Fig. 2
Salinity (g/L)	s	100	aquifer data	[Morton and Land, 1987, Fig.2A]
CO ₂ solubility (volume fraction)	χ_v	0.08	calculated	Duan and Sun [2003]
Brine density (kg/m ³)	ρ_w	1000	calculated	Batzle and Wang [1992]
CO ₂ density (kg/m ³)	ρ_g	500	calculated	Carbon Capture and Sequestration Techn
Brine density change from diss. (kg/m ³)	$\Delta\rho_d$	8	calculated	Garcia [2001]; Bachu and Adams [2003]
Brine viscosity (mPa s)	μ_w	0.6	calculated	Batzle and Wang [1992]
CO ₂ viscosity (mPa s)	μ_g	0.04	calculated	Carbon Capture and Sequestration Techn
Fracture pressure (MPa)	P_{frac}	20	calculated	Eq. 15,14; Zoback and Zoback [1980a]

^a We set the Darcy velocity to 10 cm/yr based on reported ranges for the velocity Kreitler et al. [1990] and values in other c

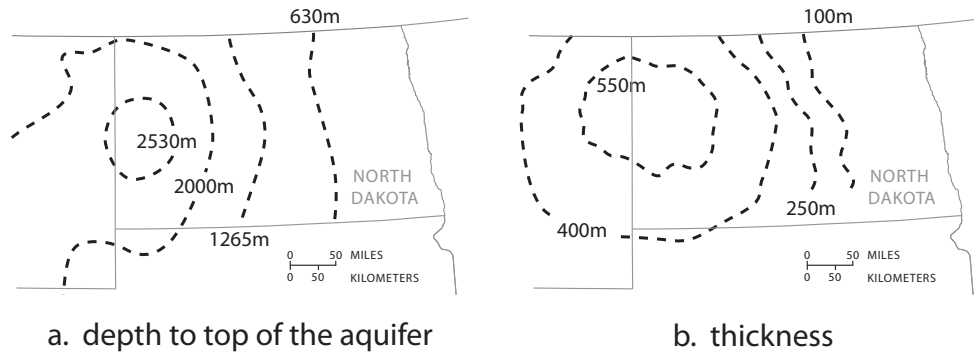


Figure 23: The Madison Limestone is located in Williston Basin in North Dakota, South Dakota, and Montana. The basin is roughly bowl-shaped, with the center and deepest part of the bowl located in western North Dakota. (a) Modified from [Hovorka et al., 2003a, Map c1madisong]. (b) Modified from [Downey, 1984, Fig.11].

Madison Limestone

The Madison Limestone occurs in the Williston Basin Whitehead [1996]. In general, it dips and thickens towards the center of the basin in western North Dakota, as shown Figure 23.

The Madison Limestone consists of a sequence of carbonates and evaporates that are divided into three formations Downey [1984]. From oldest to youngest, these are the Lodgepole Limestone, the Mission Canyon Limestone, and the Charles Formation. The Lodgepole Limestone consists mainly of argillaceous, thin-bedded limestone and dolomite. The Mission Canyon Limestone consists mainly of limestone that is coarsely crystalline at its base and finer at its top. The Charles Formation consists of anhydrite and halite with interbedded dolomite and limestone.

In the Williston Basin, the Madison Limestone is overlain by the Big Snowy Group Downey [1984]. This group consists mostly of shale and sandstone, with minor limestone. We model it together with the Charles Formation as an aquitard. The aquifer is underlain by the Bakken Formation in the Williston Basin, which consists of more than 30 meters of shale and siltstone Downey [1984]. We model this formation as an aquiclude.

We model sequestration in two regions of the Madison Limestone, as shown in Figure 24. Within each region, we identify one model domain. The data for each domain are shown in Tables 13 and 14.

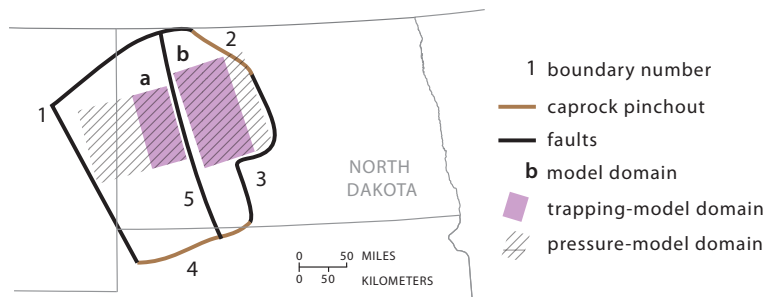


Figure 24: We identify five boundaries that constrain the portion of the Frio Formation that is suitable for sequestration. Boundaries 1, 3, and 5 correspond to basin-scale faults and lineaments [Downey, 1984, Fig.16]. Boundaries 2 and 4 correspond to where the caprock pinches out [Downey, 1984, Fig.12]. Within these boundaries, we identify two regions in which to apply our models (Regions a and b).

Table 13: Parameters for Region a of the Madison Limestone.

Parameter	Symbol	Value	Data Source	Reference
Residual CO ₂ saturation	S_{rg}	0.3	estimated	Bennion and Bachu [2008]; Oak et al. [1998]
Connate water saturation	S_{wc}	0.4	estimated	Bennion and Bachu [2008]; Oak et al. [1998]
Endpoint relative permeability to CO ₂	k_{rg}^*	0.6	estimated	Bennion and Bachu [2008]; Oak et al. [1998]
Coefficient of CO ₂ -saturated-brine flux	α	0.01	estimated	Kneafsey and Pruess [2010a]; Riaz et al. [2004]
Compressibility (GPa ⁻¹)	c	0.1	estimated	[Wang, 2000, Table C1]
Undrained Poisson ratio	ν	0.3	estimated	[Wang, 2000, Table C1]
Geothermal gradient (°C/km)	G_T	40	aquifer data	Kron and Heiken [1980]; Nathenson and C
Surface temperature (°C)	T_s	6	aquifer data	USs [2010]
Depth to top of aquifer (m)	D	3000	aquifer data	Szulczewski [2009]
Depth from aquifer to bedrock (m)	B	2000	aquifer data	Frezon et al. [1983]
Net aquifer thickness (m)	H	600	aquifer data	Szulczewski [2009]
Length of model domain (km)	L_T	60	aquifer data	Fig. 24
Length of pressure domain (km)	L_{pres}	200	aquifer data	Fig. 24
Width of well array (km)	W	100	aquifer data	Fig. 24
Porosity	ϕ	0.08	estimated	Szulczewski [2009]
Caprock slope (degrees)	ϑ	0.4	calculated	Szulczewski [2009]
Darcy velocity (cm/yr)	U	8	calculated	Szulczewski [2009]
Aquifer permeability (mD)	k_{aq}	60	aquifer data	Szulczewski [2009]
Mean vertical permeability (mD)	k_{cap}	0.01	estimated	Neuzil [1994]; Tokunaga et al. [1998]; Dew
Lateral overburden permeability (mD)	\bar{k}_x	30	calculated	Fig. 2
Vertical overburden permeability (mD)	\bar{k}_z	0.02	calculated	Fig. 2
Salinity (g/L)	s	200	aquifer data	[Whitehead, 1996, Fig.61]
CO ₂ solubility (volume fraction)	χ_v	0.05	calculated	Duan and Sun [2003]
Brine density (kg/m ³)	ρ_w	1000	calculated	Batzle and Wang [1992]
CO ₂ density (kg/m ³)	ρ_g	500	calculated	Carbon Capture and Sequestration Techn
Brine density change from diss. (kg/m ³)	$\Delta\rho_d$	5	calculated	Garcia [2001]; Bachu and Adams [2003]
Brine viscosity (mPa s)	μ_w	0.4	calculated	Batzle and Wang [1992]
CO ₂ viscosity (mPa s)	μ_g	0.04	calculated	Carbon Capture and Sequestration Techn
Fracture pressure (MPa)	P_{frac}	30	calculated	Eq. 15,14; Zoback and Zoback [1980a]

Table 14: Parameters for Region b of the Madison Limestone.

Parameter	Symbol	Value	Data Source	Reference
Residual CO ₂ saturation	S_{rg}	0.3	estimated	Bennion and Bachu [2008]; Oak et al. [1998]
Connate water saturation	S_{wc}	0.4	estimated	Bennion and Bachu [2008]; Oak et al. [1998]
Endpoint relative permeability to CO ₂	k_{rg}^*	0.6	estimated	Bennion and Bachu [2008]; Oak et al. [1998]
Coefficient of CO ₂ -saturated-brine flux	α	0.01	estimated	Kneafsey and Pruess [2010a]; Riaz et al. [2004]
Compressibility (GPa ⁻¹)	c	0.1	estimated	[Wang, 2000, Table C1]
Undrained Poisson ratio	ν	0.3	estimated	[Wang, 2000, Table C1]
Geothermal gradient (°C/km)	G_T	40	aquifer data	Kron and Heiken [1980]; Nathenson and C
Surface temperature (°C)	T_s	6	aquifer data	USs [2010]
Depth to top of aquifer (m)	D	2000	aquifer data	Szulczewski [2009]
Depth from aquifer to bedrock (m)	B	1000	aquifer data	Frezon et al. [1983]
Net aquifer thickness (m)	H	500	aquifer data	Szulczewski [2009]
Length of model domain (km)	L_T	90	aquifer data	Fig. 24
Length of pressure domain (km)	L_{pres}	100	aquifer data	Fig. 24
Width of well array (km)	W	200	aquifer data	Fig. 24
Porosity	ϕ	0.08	estimated	Szulczewski [2009]
Caprock slope (degrees)	ϑ	0.5	calculated	Szulczewski [2009]
Darcy velocity (cm/yr)	U	5	calculated	Szulczewski [2009]
Aquifer permeability (mD)	k_{aq}	60	aquifer data	Szulczewski [2009]
Mean vertical permeability (mD)	k_{cap}	0.01	estimated	Neuzil [1994]; Tokunaga et al. [1998]; Dew
Lateral overburden permeability (mD)	\bar{k}_x	30	calculated	Fig. 2
Vertical overburden permeability (mD)	\bar{k}_z	0.02	calculated	Fig. 2
Salinity (g/L)	s	300	aquifer data	[Whitehead, 1996, Fig.61]
CO ₂ solubility (volume fraction)	χ_v	0.03	calculated	Duan and Sun [2003]
Brine density (kg/m ³)	ρ_w	1000	calculated	Batzle and Wang [1992]
CO ₂ density (kg/m ³)	ρ_g	500	calculated	Carbon Capture and Sequestration Techn
Brine density change from diss. (kg/m ³)	$\Delta\rho_d$	11	calculated	Garcia [2001]; Bachu and Adams [2003]
Brine viscosity (mPa s)	μ_w	0.6	calculated	Batzle and Wang [1992]
CO ₂ viscosity (mPa s)	μ_g	0.04	calculated	Carbon Capture and Sequestration Techn
Fracture pressure (MPa)	P_{frac}	30	calculated	Eq. 15,14; Zoback and Zoback [1980a]

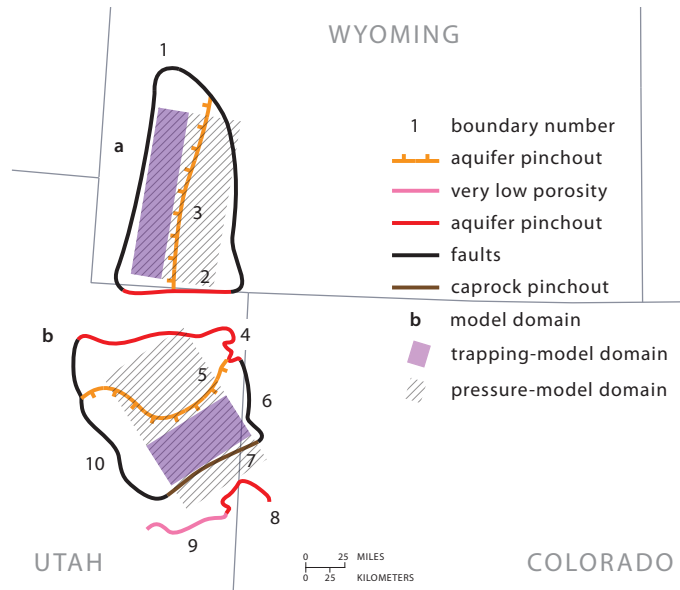


Figure 25: We identify ten boundaries that constrain the portion of the Navajo-Nugget Aquifer that is suitable for sequestration. Boundaries 1, 6, and 10 correspond to basin-scale faults in Mesozoic rocks [Freethy and Cordy, 1991, Fig.6]. Boundaries 2, 4, and 8 mark where the Navajo-Nugget Aquifer is absent [Freethy et al., 1988, Fig.14]. Boundaries 3 and 5 correspond to where the aquifer becomes more than 4000 m deep, which we consider to be too deep for a cost-effective sequestration project National Imagery and Mapping Agency; Freethy et al. [1988]. Boundary 7 corresponds to the farthest extent of the Carmel-Twin Creek Confining Unit [Freethy and Cordy, 1991, Plate 2B]. Lastly, Boundary 9 corresponds to where the Navajo-Nugget Aquifer crops out [Freethy et al., 1988, Fig.14]

Navajo-Nugget Aquifer

The Navajo-Nugget Aquifer is sufficiently deep for sequestration in the eastern Uinta Basin in northeastern Utah and the Green River Basin in southwest Wyoming [Freethy and Cordy, 1991, Figure 10]. In the eastern Uinta Basin, it consists of the Glen Canyon Sandstone. In the Green River Basin, it consists of the Nugget Sandstone [Freethy and Cordy, 1991, Plate 1]. These rocks were deposited primarily in an eolian environment, but contain minor fluvial components. They typically consist of massive, crossbedded sandstone that has well-sorted, very fine to medium grains [Freethy and Cordy, 1991, p.C17].

The Navajo-Nugget Aquifer is overlain by the Carmel-Twin Creek Confining Unit. This unit consists mostly of siltstone and shale with some interbedded gypsum. The aquifer is underlain by the Chinle-Moenkopi Confining Unit. This unit consists mostly of siltstone, claystone, and limestone [Freethy and Cordy, 1991, Table 1].

We model sequestration from one well array in both the Uinta Basin and the Green River Basin, as shown in Figure 25. The data for these regions are shown in Tables 15 and 16.

Table 15: Parameters for Region a of the Navajo-Nugget Aquifer.

Parameter	Symbol	Value	Data Source	Reference
Residual CO ₂ saturation	S_{rg}	0.3	estimated	Bennion and Bachu [2008]; Oak et al. [1998]
Connate water saturation	S_{wc}	0.4	estimated	Bennion and Bachu [2008]; Oak et al. [1998]
Endpoint relative permeability to CO ₂	k_{rg}^*	0.6	estimated	Bennion and Bachu [2008]; Oak et al. [1998]
Coefficient of CO ₂ -saturated-brine flux	α	0.01	estimated	Kneafsey and Pruess [2010a]; Riaz et al. [2007]
Compressibility (GPa ⁻¹)	c	0.1	estimated	[Wang, 2000, Table C1]
Undrained Poisson ratio	ν	0.3	estimated	[Wang, 2000, Table C1]
Geothermal gradient (°C/km)	G_T	30	aquifer data	Kron and Heiken [1980]; Nathenson and Calkins [1998]
Surface temperature (°C)	T_s	6	aquifer data	USGS [2010]
Depth to top of aquifer (m)	D	3000	aquifer data	National Imagery and Mapping Agency; Freethy et al. [1988]
Depth from aquifer to bedrock (m)	B	500	aquifer data	Frezon et al. [1983]; Freethy et al. [1988]
Net aquifer thickness (m)	H	200	aquifer data	[Freethy and Cordy, 1991, Plate 3A]
Length of trapping-model domain (km)	L_T	30	aquifer data	Fig. 25
Length of pressure-model domain (km)	L_{pres}	90	aquifer data	Fig. 25
Width of well array (km)	W	200	aquifer data	Fig. 25
Porosity	ϕ	0.2	estimated	[Freethy and Cordy, 1991, Fig.30]
Caprock slope (degrees)	ϑ	2	calculated	Freethy et al. [1988]
Darcy velocity (cm/yr)	U	10 ^a	calculated	[Freethy et al., 1988, Fig.15]
Aquifer permeability (mD)	k_{aq}	100 ^b	calculated	[Freethy and Cordy, 1991, Figs.33,46]
Mean vertical permeability (mD)	k_{cap}	0.01	estimated	Neuzil [1994]; Tokunaga et al. [1998]; Dewettinck et al. [2000]
Lateral overburden permeability (mD)	\bar{k}_x	50	calculated	Fig. 2
Vertical overburden permeability (mD)	\bar{k}_z	0.02	calculated	Fig. 2
Salinity (g/L)	s	35	aquifer data	[Freethy et al., 1988, Fig.19]
CO ₂ solubility (volume fraction)	χ_v	0.07	calculated	MacMinn et al. [2011]; Duan and Sun [2002]
Brine density (kg/m ³)	ρ_w	1000	calculated	Batzle and Wang [1992]
CO ₂ density (kg/m ³)	ρ_g	600	calculated	Carbon Capture and Sequestration Technology Center [2009]
Brine density change from diss. (kg/m ³)	$\Delta\rho_d$	9	calculated	Garcia [2001]; Bachu and Adams [2003]
Brine viscosity (mPa s)	μ_w	0.4	calculated	Batzle and Wang [1992]
CO ₂ viscosity (mPa s)	μ_g	0.05	calculated	Carbon Capture and Sequestration Technology Center [2009]
Fracture pressure (MPa)	P_{frac}	70	calculated	Eq. 15,14; Zoback and Zoback [1980a]

^a In deep parts of the aquifer where we model sequestration, hydraulic head measurements are not available. As a result, we use a Darcy velocity based on head measurements in the shallower parts of the reservoir. While the actual velocity in the model domain is likely higher, the Darcy velocity does not affect the capacity estimation since migration is driven dominantly by slope ($N_s/N_f \gg 1$).

^b Hydraulic conductivity data for the Navajo-Nugget Aquifer generally comes from outcrops or shallow wells, where it is about 3 m/day [Freethy and Cordy, 1991, Figs.33,46]. This corresponds to permeabilities in the range of about 40 to 4000 mD. In areas where sequestration are deeply buried, we set the permeability to a low value in this range.

Table 16: Parameters for Region b of the Navajo-Nugget Aquifer.

Parameter	Symbol	Value	Data Source	Reference
Residual CO ₂ saturation	S_{rg}	0.3	estimated	Bennion and Bachu [2008]; Oak et al. [1998]
Connate water saturation	S_{wc}	0.4	estimated	Bennion and Bachu [2008]; Oak et al. [1998]
Endpoint relative permeability to CO ₂	k_{rg}^*	0.6	estimated	Bennion and Bachu [2008]; Oak et al. [1998]
Coefficient of CO ₂ -saturated-brine flux	α	0.01	estimated	Kneafsey and Pruess [2010a]; Riaz et al. [2004]
Compressibility (GPa ⁻¹)	c	0.1	estimated	[Wang, 2000, Table C1]
Undrained Poisson ratio	ν	0.3	estimated	[Wang, 2000, Table C1]
Geothermal gradient (°C/km)	G_T	30	aquifer data	Kron and Heiken [1980]; Nathenson and C
Surface temperature (°C)	T_s	10	aquifer data	USs [2010]
Depth to top of aquifer (m)	D	3000	aquifer data	National Imagery and Mapping Agency; F
Depth from aquifer to bedrock (m)	B	5000	aquifer data	Frezon et al. [1983]; Freethey et al. [1988]
Net aquifer thickness (m)	H	200	aquifer data	[Freethey and Cordy, 1991, Plate 3A]
Length of trapping-model domain (km)	L_T	50	aquifer data	Fig. 25
Length of pressure-model domain (km)	L_{pres}	200	aquifer data	Fig. 25
Width of well array (km)	W	100	aquifer data	Fig. 25
Porosity	ϕ	0.2	estimated	[Freethey and Cordy, 1991, Fig.30]
Caprock slope (degrees)	ϑ	2	calculated	Freethey et al. [1988]
Darcy velocity (cm/yr)	U	10 ^a	calculated	[Freethey et al., 1988, Fig.15]
Aquifer permeability (mD)	k_{aq}	100 ^b	calculated	[Freethey and Cordy, 1991, Figs.33,46]
Mean vertical permeability (mD)	k_{cap}	0.01	estimated	Neuzil [1994]; Tokunaga et al. [1998]; Dew
Lateral overburden permeability (mD)	\bar{k}_x	50	calculated	Fig. 2
Vertical overburden permeability (mD)	\bar{k}_z	0.02	calculated	Fig. 2
Salinity (g/L)	s	35	aquifer data	[Freethey et al., 1988, Fig.19]
CO ₂ solubility (volume fraction)	χ_v	0.07	calculated	MacMinn et al. [2011]; Duan and Sun [2002]
Brine density (kg/m ³)	ρ_w	1000	calculated	Batzle and Wang [1992]
CO ₂ density (kg/m ³)	ρ_g	600	calculated	Carbon Capture and Sequestration Techn
Brine density change from diss. (kg/m ³)	$\Delta\rho_d$	10	calculated	Garcia [2001]; Bachu and Adams [2003]
Brine viscosity (mPa s)	μ_w	0.4	calculated	Batzle and Wang [1992]
CO ₂ viscosity (mPa s)	μ_g	0.05	calculated	Carbon Capture and Sequestration Techn
Fracture pressure (MPa)	P_{frac}	60	calculated	Eq. 15,14; Zoback and Zoback [1980a]

^a In deep parts of the aquifer where we model sequestration, hydraulic head measurements are not available. As a result, we based on head measurements in the shallower parts of the reservoir. While the actual velocity in the model domain is likely different, the Darcy velocity does not affect the capacity estimation since migration is driven dominantly by slope ($N_s/N_f \gg 1$).

^b Hydraulic conductivity data for the Navajo-Nugget Aquifer generally comes from outcrops or shallow wells, where it is about 3 m/day [Freethey and Cordy, 1991, Figs.33,46]. This corresponds to permeabilities in the range of about 40 to 4000 mD. In areas where sequestration are deeply buried, we set the permeability to a low value in this range.

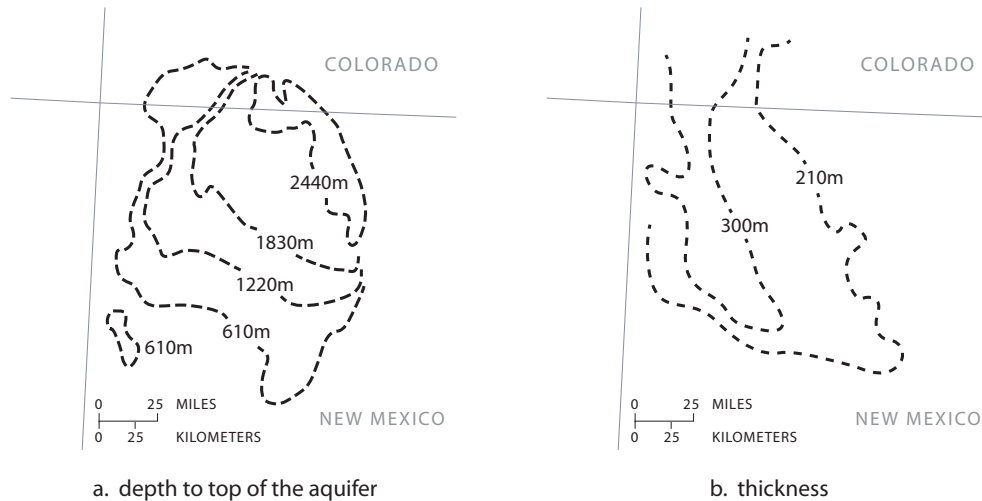


Figure 26: (a) The Morrison Formation deepens toward a northwest-southeast axis in the northeastern part of the San Juan Basin. Modified from [Dam et al., 1990, Fig.6]. (b) It thickens toward a north-south axis in the western part of the basin. Modified from [Dam et al., 1990, Fig.5].

Morrison Formation

The Morrison Formation occurs in the northwestern corner of New Mexico in the San Juan Basin, as shown in Figure 26. It consists of five members that have varying extents [Kernodle, 1996, p.48]. The bottom three members are the Salt Wash Member, the Recapture Member, and the Westwater Canyon Member. These members consist mainly of interbedded sandstone and claystone, and are the target members for sequestration in our study [Craig et al., 1955, p.135-155]. They are overlain by the Brushy Basin Member and the Jackpile Sandstone Member. The Brushy Basin member consists predominantly of claystone that contains varying amounts of silt and sand [Craig et al., 1955, p.135-156]. We take it to be the caprock in our study.

The Morrison Formation is underlain by the Wanakah Formation in the San Juan Basin. The uppermost member of this formation is the Todilto Member, which consists of limestone overlain by gypsum and anhydrite. The Wanakah Formation has been identified in previous hydrologic studies as a confining unit, and we take it to be the aquiclude in our study [Kernodle, 1996, p.54].

We model sequestration in the center of the San Juan Basin, as shown in Figure 27. The data for this region are shown in Table 17.

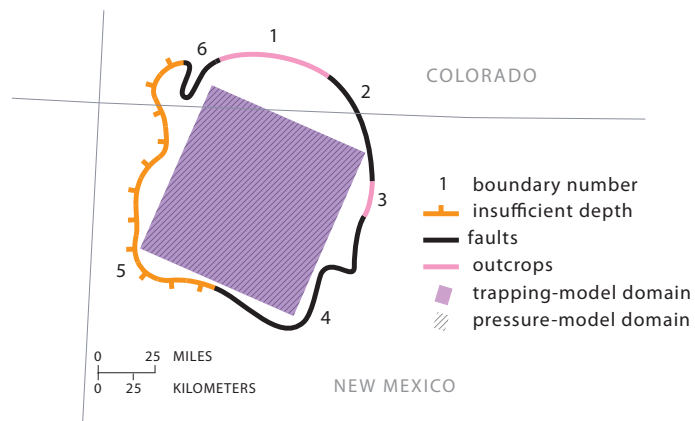


Figure 27: We identify six boundaries that constrain the portion of the Morrison Formation that is suitable for sequestration. Boundaries 1 and 3 correspond to outcrops, and Boundary 5 corresponds to where the depth to the top of the formation becomes less than 800 m [Dam et al., 1990, Fig.6]. Boundaries 2, 4, and 6 exclude major faults or fault systems in the San Juan Basin from the study area [Kernodle, 1996, Fig.7].

Table 17: Parameters for the Morrison Formation.

Parameter	Symbol	Value	Data Source	Reference
Residual CO ₂ saturation	S_{rg}	0.3	estimated	Bennion and Bachu [2008]; Oak et al. [1998]
Connate water saturation	S_{wc}	0.4	estimated	Bennion and Bachu [2008]; Oak et al. [1998]
Endpoint relative permeability to CO ₂	k_{rg}^*	0.6	estimated	Bennion and Bachu [2008]; Oak et al. [1998]
Coefficient of CO ₂ -saturated-brine flux	α	0.01	estimated	Kneafsey and Pruess [2010a]; Riaz et al. [2007]
Compressibility (GPa ⁻¹)	c	0.1	estimated	[Wang, 2000, Table C1]
Undrained Poisson ratio	ν	0.3	estimated	[Wang, 2000, Table C1]
Geothermal gradient (°C/km)	G_T	30	aquifer data	Kron and Heiken [1980]; Nathenson and C
Surface temperature (°C)	T_s	10	aquifer data	USs [2010]
Depth to top of aquifer (m)	D	2000 ^a	aquifer data	[Dam et al., 1990, Fig.6][Craig et al., 1955]
Depth from aquifer to bedrock (m)	B	1000	aquifer data	Frezon et al. [1983]
Net aquifer thickness (m)	H	200 ^b	aquifer data	[Dam et al., 1990, Fig.5][Craig et al., 1955]
Length of trapping-model domain (km)	L_T	100	aquifer data	Fig. 27
Length of pressure-model domain (km)	L_{pres}	100	aquifer data	Fig. 27
Width of well array (km)	W	100	aquifer data	Fig. 27
Porosity	ϕ	0.2	estimated	
Caprock slope (degrees)	ϑ	0.9	calculated	[Dam et al., 1990, Fig.7]
Darcy velocity (cm/yr)	U	8	calculated	[Kernodle, 1996, Fig.52][Dam et al., 1990, Fig.29]
Aquifer permeability (mD)	k_{aq}	70 ^c	calculated	[Dam et al., 1990, Fig.9]
Mean vertical permeability (mD)	k_{cap}	0.01	estimated	Neuzil [1994]; Tokunaga et al. [1998]; Dew
Lateral overburden permeability (mD)	\bar{k}_x	40	calculated	Fig. 2
Vertical overburden permeability (mD)	\bar{k}_z	0.02	calculated	Fig. 2
Salinity (g/L)	s	5	aquifer data	[Dam et al., 1990, Fig.15]
CO ₂ solubility (volume fraction)	χ_v	0.09	calculated	Duan and Sun [2003]
Brine density (kg/m ³)	ρ_w	1000	calculated	Batzle and Wang [1992]
CO ₂ density (kg/m ³)	ρ_g	600	calculated	Carbon Capture and Sequestration Techn
Brine density change from diss. (kg/m ³)	$\Delta\rho_d$	10	calculated	Garcia [2001]; Bachu and Adams [2003]
Brine viscosity (mPa s)	μ_w	0.4	calculated	Batzle and Wang [1992]
CO ₂ viscosity (mPa s)	μ_g	0.04	calculated	Carbon Capture and Sequestration Techn
Fracture pressure (MPa)	P_{frac}	50	calculated	Eq. 15,14; Zoback and Zoback [1980a]

^a We calculate the depth of the target members—the Salt Wash Member, the Recapture Member, and the Westwater C—by adding the depth of the Morrison Formation [Dam et al., 1990, Fig.6] to the thickness of the Brushy Basin Member [Craig et al., 1955, Fig.29], which is the topmost unit of the formation. We ignore the Jackpile Sandstone Member since it exists mainly in the basin outside of the trapping model domain.

^b We calculate the thickness of the target members by subtracting the thickness of the Brushy Basin Member [Craig et al., 1955, Fig.29] from the thickness of entire the Morrison Formation [Dam et al., 1990, Fig.5].

^c We found only a few values of transmissivity within the model domain. To calculate permeability, we divide the transmissivity by the aquifer thickness at that location to determine hydraulic conductivity, and then multiply that value by μ_w/ρ_w to

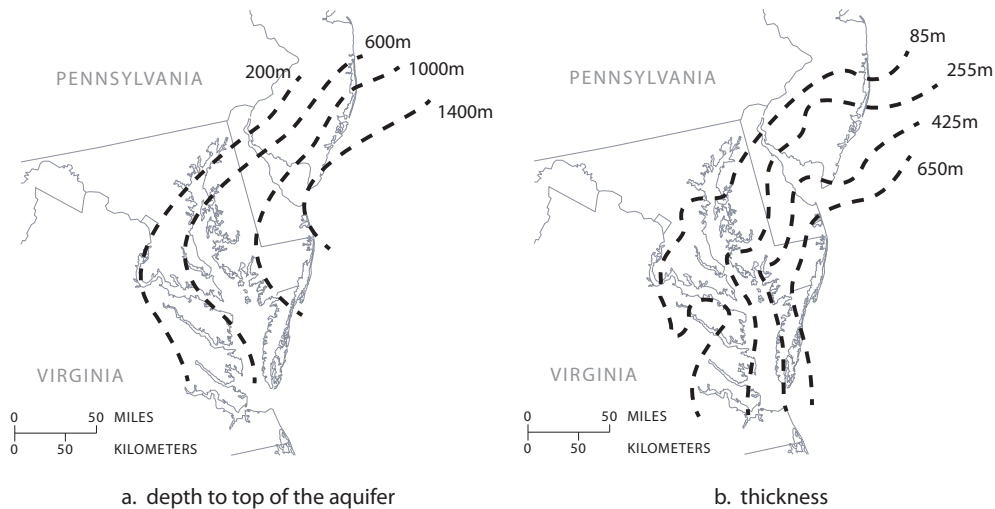


Figure 28: (a) The western limit of the aquifer is the Fall Line, where it pinches out against crystalline rock Trapp and Horn [1997]. From the Fall Line, it dips and thickens seaward. (a) Modified from [Hovorka et al., 2003a, Map c1potomac]. (b) Modified from [Hovorka et al., 2003a, Map c3potomac].

Lower Potomac Aquifer

While the Lower Potomac Aquifer underlies almost the entire North Atlantic Coastal Plain, we study sequestration in Maryland and Delaware. Here it consists mostly of sediments deposited in fluvial or deltaic environments: it contains lenses of sand and gravel with interstitial clay [H. Trapp, 1992, p.G30]. These lenses constitute between 20 and 60% of the aquifer thickness, and are interbedded with clayey and silty layers.

The aquifer is bounded above by a confining unit composed mostly of clay and sandy clay beds. It is bounded below by crystalline bedrock H. Trapp [1992]; Trapp and Horn [1997].

While the Lower Potomac Aquifer extends under the Chesapeake Bay and the Atlantic Ocean, we study CO₂ storage only under the Delmarva Peninsula, as shown in Figure 29. The data for this region is shown in Table 18.

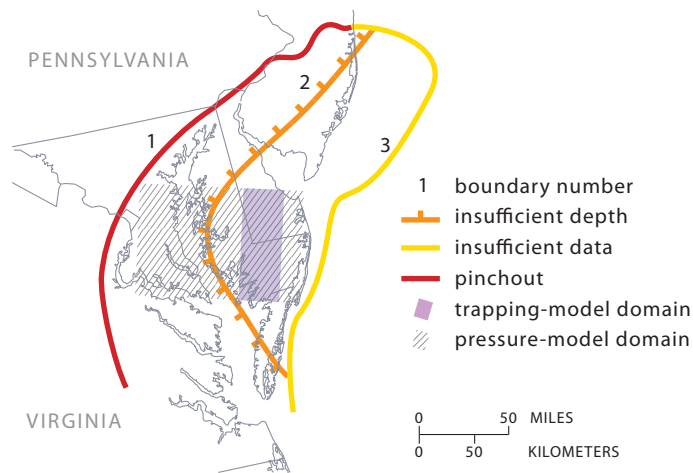


Figure 29: We identify 3 boundaries that constrain the portion of the Lower Potomac Aquifer that is suitable for sequestration. Boundary 1 corresponds to the Fall Line, where Coastal Plain sediments crop out or pinch out against the crystalline basement [H. Trapp, 1992, Plate 1A,1B]. Since it is unclear whether the Lower Potomac pinches out or crops out in the study area, we choose this boundary to be a pinchout boundary to make our capacity estimates conservative. Boundary 2 corresponds to where the top of the aquifer becomes less than 800 m deep [Hovorka et al., 2003a, Map c1potomac]. Boundary 3 corresponds to the limits of the aquifer depth and thickness maps [Hovorka et al., 2003a, Maps c1potomac, c3potomac].

Table 18: Parameters for the Lower Potomac Aquifer.

Parameter	Symbol	Value	Data Source	Reference
Residual CO ₂ saturation	S_{rg}	0.3	estimated	Bennion and Bachu [2008]; Oak et al. [1998]
Connate water saturation	S_{wc}	0.4	estimated	Bennion and Bachu [2008]; Oak et al. [1998]
Endpoint relative permeability to CO ₂	k_{rg}^*	0.6	estimated	Bennion and Bachu [2008]; Oak et al. [1998]
Coefficient of CO ₂ -saturated-brine flux	α	0.01	estimated	Kneafsey and Pruess [2010a]; Riaz et al. [2004]
Compressibility (GPa ⁻¹)	c	0.1	estimated	[Wang, 2000, Table C1]
Undrained Poisson ratio	ν	0.3	estimated	[Wang, 2000, Table C1]
Geothermal gradient (°C/km)	G_T	30	aquifer data	Kron and Heiken [1980]; Nathenson and C
Surface temperature (°C)	T_s	10	aquifer data	USs [2010]
Depth to top of aquifer (m)	D	1000	aquifer data	[Hovorka et al., 2003a, Map c1potomac]
Depth from aquifer to bedrock (m)	B	0	aquifer data	[Trapp and Horn, 1997, Fig.19,20]
Net aquifer thickness (m)	H	400	aquifer data	[Hovorka et al., 2003a, Map c4potomac]
Length of trapping-model domain (km)	L_T	40	aquifer data	Fig. 29
Length of pressure-model domain (km)	L_{pres}	100	aquifer data	Fig. 29
Width of well array (km)	W	100	aquifer data	Fig. 29
Porosity	ϕ	0.2	estimated	
Caprock slope (degrees)	ϑ	0.3	calculated	[H. Trapp, 1992, Plate 7B]
Darcy velocity (cm/yr)	U	10	calculated	[Szulczewski, 2009, Table A.1]
Aquifer permeability (mD)	k_{aq}	3000	calculated	[Szulczewski, 2009, Table A.1]
Mean vertical permeability (mD)	k_{cap}	0.1	estimated	Neuzil [1994]; Tokunaga et al. [1998]; Dew
Lateral overburden permeability (mD)	\bar{k}_x	2000	calculated	Fig. 2
Vertical overburden permeability (mD)	\bar{k}_z	0.2	calculated	Fig. 2
Salinity (g/L)	s	5	aquifer data	[Trapp and Horn, 1997, Fig.57]
CO ₂ solubility (volume fraction)	χ_v	0.1	calculated	Duan and Sun [2003]
Brine density (kg/m ³)	ρ_w	1000	calculated	Batzle and Wang [1992]
CO ₂ density (kg/m ³)	ρ_g	500	calculated	Carbon Capture and Sequestration Techn
Brine density change from diss. (kg/m ³)	$\Delta\rho_d$	10	calculated	Garcia [2001]; Bachu and Adams [2003]
Brine viscosity (mPa s)	μ_w	0.7	calculated	Batzle and Wang [1992]
CO ₂ viscosity (mPa s)	μ_g	0.04	calculated	Carbon Capture and Sequestration Techn
Fracture pressure (MPa)	P_{frac}	20	calculated	Eq. 15,14; Zoback and Zoback [1980a]

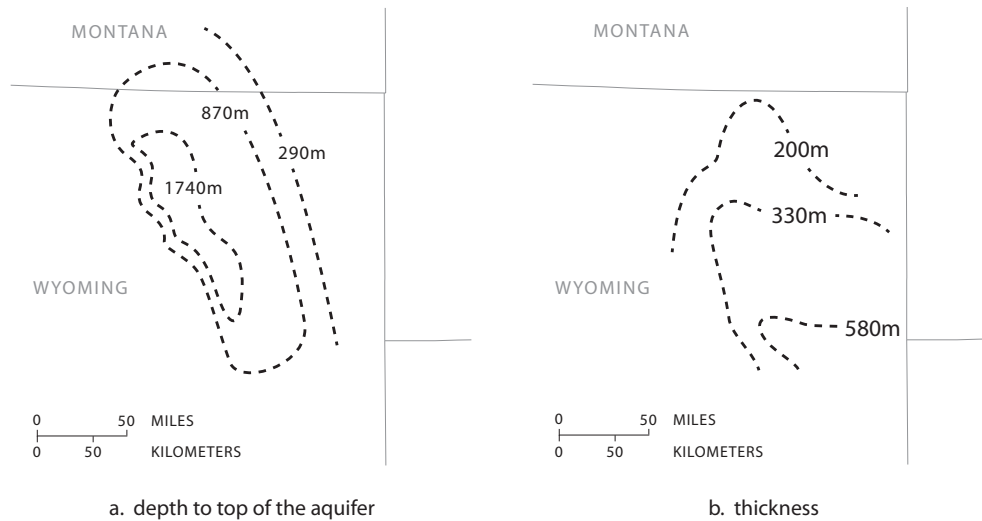


Figure 30: The Fox Hills Sandstone deepens along the axis of the Powder River Basin, which runs northwest to southeast. It thickens toward the southeast. (a) Modified from [Hovorka et al., 2003a, Map c1foxhillsg]. (b) Modified from [Hovorka et al., 2003a, Map c3foxhillsg].

Fox Hills Sandstone

The Fox Hills Sandstone occurs in the Powder River Basin, which is located in northeastern Wyoming. In general, it consists of massive, fine- to medium-grained sandstone with siltstone and minor shale, which are sometimes interbedded [Merewether, 1996, p.T68]. The depth to the top of these rocks and their thickness are shown in Figure 30.

The Fox Hills Sandstone is conformably overlain by and intertongued with the Lance Formation in Wyoming, which provides an extensive top seal [Hovorka et al., 2003c, p.82]. It is conformably underlain by marine shale and siltstone in the Lewis Shale or Pierre Shale, which forms an aquiclude [Downey and Dinwiddie, 1988, Plate II].

We model sequestration in the center of the Powder River Basin, as shown in Figure 31. The data for this region is shown in Table 19.

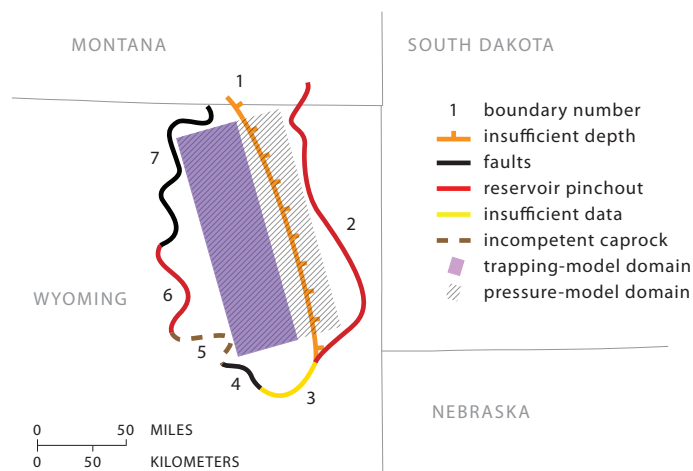


Figure 31: We identify 7 boundaries that constrain the portion of the Fox Hills Sandstone that is suitable for sequestration. Boundary 1 corresponds to where the top of the reservoir becomes less than 800 m deep [Hovorka et al., 2003a, Map c1foxhillsg]. Boundaries 2 and 6 correspond to where we interpret the reservoir to pinch out. While we found no cross sections of the reservoir at these locations, we base this interpretation on the observation that the caprock and rocks stratigraphically below the reservoir crop out contiguously there [Whitehead, 1996, Fig.56]. Boundary 3 corresponds to the limit of the reservoir depth and thickness maps [Hovorka et al., 2003a, Maps c1foxhillsg, c3foxhillsg]. Boundaries 4 and 7 correspond to basin-scale faults [Whitehead, 1996, Fig.56]. Lastly, Boundary 5 corresponds to where the caprock contains more than 50% sand [Hovorka et al., 2003a, Map 81foxhillsg].

Table 19: Parameters for the Fox Hills Sandstone.

Parameter	Symbol	Value	Data Source	Reference
Residual CO ₂ saturation	S_{rg}	0.3	estimated	Bennion and Bachu [2008]; Oak et al. [1998]
Connate water saturation	S_{wc}	0.4	estimated	Bennion and Bachu [2008]; Oak et al. [1998]
Endpoint relative permeability to CO ₂	k_{rg}^*	0.6	estimated	Bennion and Bachu [2008]; Oak et al. [1998]
Coefficient of CO ₂ -saturated-brine flux	α	0.01	estimated	Kneafsey and Pruess [2010a]; Riaz et al. [2007]
Compressibility (GPa ⁻¹)	c	0.1	estimated	[Wang, 2000, Table C1]
Undrained Poisson ratio	ν	0.3	estimated	[Wang, 2000, Table C1]
Geothermal gradient (°C/km)	G_T	30	aquifer data	Kron and Heiken [1980]; Nathenson and Coats [1990]
Surface temperature (°C)	T_s	10	aquifer data	USs [2010]
Depth to top of aquifer (m)	D	1000	aquifer data	[Hovorka et al., 2003a, Map c1fohillsg]
Depth from aquifer to bedrock (m)	B	4000	aquifer data	Frezon et al. [1983]
Net aquifer thickness (m)	H	200	aquifer data	[Hovorka et al., 2003a, Map 4fohillsg]
Length of trapping-model domain (km)	L_T	100	aquifer data	Fig. 31
Length of pressure-model domain (km)	L_{pres}	100	aquifer data	Fig. 31
Width of well array (km)	W	200	aquifer data	Fig. 31
Porosity	ϕ	0.2	estimated	
Caprock slope (degrees)	ϑ	1	calculated	[Hovorka et al., 2003a, Map c1fohillsg]
Darcy velocity (cm/yr)	U	10 ^a	calculated	[Whitehead, 1996, Fig.56], McPherson and Cole [2000]
Aquifer permeability (mD)	k_{aq}	100	calculated	McPherson and Cole [2000]
Mean vertical permeability (mD)	k_{cap}	.01	estimated	Neuzil [1994]; Tokunaga et al. [1998]; Dewett [1998]
Lateral overburden permeability (mD)	\bar{k}_x	50	calculated	Fig. 2
Vertical overburden permeability (mD)	\bar{k}_z	0.02	calculated	Fig. 2
Salinity (g/L)	s	2	aquifer data	[Whitehead, 1996, Fig.57]
CO ₂ solubility (volume fraction)	χ_v	0.1	calculated	Duan and Sun [2003]
Brine density (kg/m ³)	ρ_w	1000	calculated	Batzle and Wang [1992]
CO ₂ density (kg/m ³)	ρ_g	500	calculated	Carbon Capture and Sequestration Technology Center [2003]
Brine density change from diss. (kg/m ³)	$\Delta\rho_d$	11	calculated	Garcia [2001]; Bachu and Adams [2003]
Brine viscosity (mPa s)	μ_w	0.7	calculated	Batzle and Wang [1992]
CO ₂ viscosity (mPa s)	μ_g	0.04	calculated	Carbon Capture and Sequestration Technology Center [2003]
Fracture pressure (MPa)	P_{frac}	10	calculated	Eq. 15,14; Zoback and Zoback [1980a]

^a We calculate the Darcy velocity with Darcy's law, using a head gradient of 0.003 [Whitehead, 1996, Fig.56].

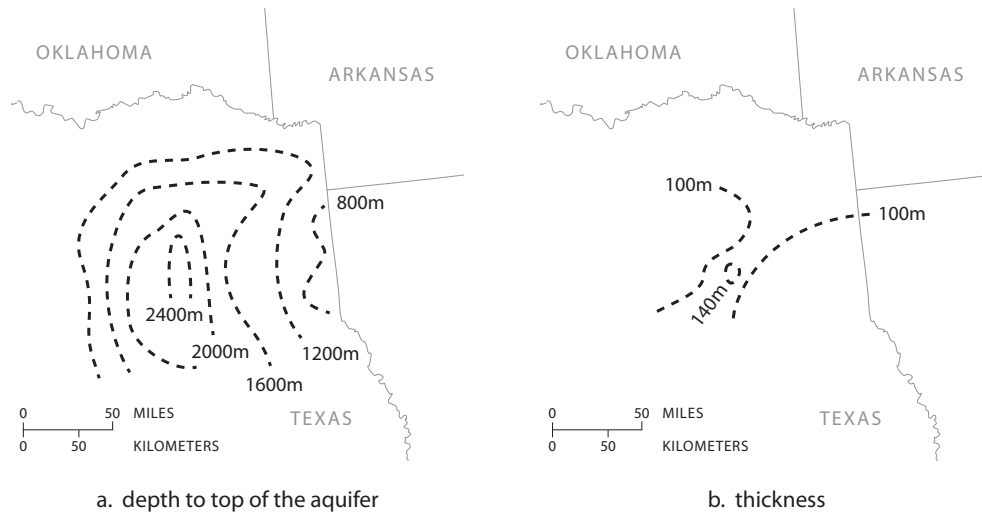


Figure 32: The Paluxy Formation deepens and thickens toward the center of the East Texas Basin. (a) Modified from [Hovorka et al., 2003a, Map c1paluxyg]. (b) Modified from [Hovorka et al., 2003a, Map c3paluxyg].

Paluxy Sandstone

While the Paluxy Formation is widespread throughout the Gulf Coastal Plain, we focus on deep parts of the formation in the East Texas Basin, which lies in northeastern Texas Foote et al. [1988]. The depth to the top of the formation and its thickness is shown in Figure 32.

In the East Texas Basin, the Paluxy Formation is a quartz arenite, but in some areas can contain up to fifty percent clay [Hovorka et al., 2003c, p.163]. It is overlain by the Goodland Limestone, which can be fairly porous and is likely a poor caprock. This limestone, however, is overlain by the Kiamichi Shale. We model this shale as the aquitard in our study and ignore the intervening Goodland Limestone since it is thin compared to the Paluxy Formation. The Paluxy is underlain by interbedded shale and limestone in the Glen Rose Formation, which we model as the aquiclude Foote et al. [1988].

We model sequestration in the center of the East Texas Basin, as shown in Figure 33. The data for this region is shown in Table 20.

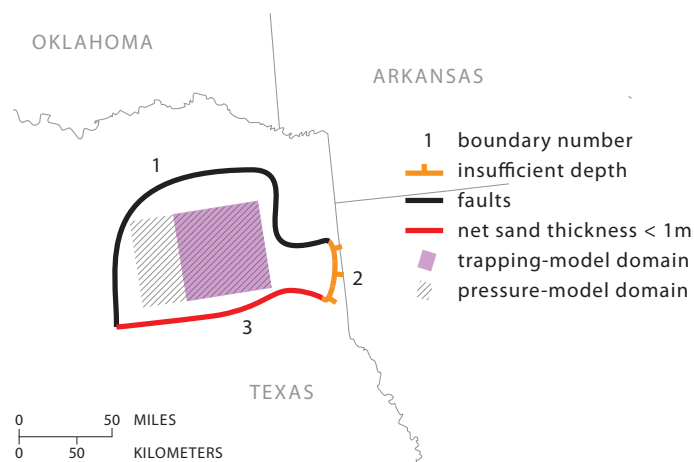


Figure 33: We identify three boundaries that constrain the portion of the Paluxy Sandstone that is suitable for sequestration. Boundary 1 corresponds to the edges of four major fault zones: the Mexia Fault Zone, the Talco Fault Zone, and the South Arkansas Fault Zone [Foote et al., 1988, Fig.3]. Boundary 2 corresponds to where the top of the formation becomes less than 800m deep [Hovorka et al., 2003a, Map c1paluxyg]. Boundary 3 marks where the net sand thickness in the formation becomes less than 1m [Hovorka et al., 2003a, Map c4paluxyg].

Table 20: Parameters for the Paluxy Sandstone.

Parameter	Symbol	Value	Data Source	Reference
Residual CO ₂ saturation	S_{rg}	0.3	estimated	Bennion and Bachu [2008]; Oak et al. [1998]
Connate water saturation	S_{wc}	0.4	estimated	Bennion and Bachu [2008]; Oak et al. [1998]
Endpoint relative permeability to CO ₂	k_{rg}^*	0.6	estimated	Bennion and Bachu [2008]; Oak et al. [1998]
Coefficient of CO ₂ -saturated-brine flux	α	0.01	estimated	Kneafsey and Pruess [2010a]; Riaz et al. [2004]
Compressibility (GPa ⁻¹)	c	0.1	estimated	[Wang, 2000, Table C1]
Undrained Poisson ratio	ν	0.3	estimated	[Wang, 2000, Table C1]
Geothermal gradient (°C/km)	G_T	30	aquifer data	Kron and Heiken [1980]; Nathenson and O'Neil [1980]
Surface temperature (°C)	T_s	20	aquifer data	USs [2010]
Depth to top of aquifer (m)	D	2000	aquifer data	[Hovorka et al., 2003a, Map c1paluxyg]
Depth from aquifer to bedrock (m)	B	6000	aquifer data	Frezon et al. [1983][Hovorka et al., 2003a, Map c2paluxyg]
Net aquifer thickness (m)	H	15	aquifer data	[Hovorka et al., 2003a, Map c3paluxyg]
Length of trapping-model domain (km)	L_T	70	aquifer data	Fig. 33
Length of pressure-model domain (km)	L_{pres}	100	aquifer data	Fig. 33
Width of well array (km)	W	80	aquifer data	Fig. 33
Porosity	ϕ	0.2	aquifer data	[Hovorka et al., 2003a, Map 14paluxy]
Caprock slope (degrees)	ϑ	1	calculated	[Hovorka et al., 2003a, Map c1paluxyg]
Darcy velocity (cm/yr)	U	5.0 ^a	estimated	
Aquifer permeability (mD)	k_{aq}	300	aquifer data	[Hovorka et al., 2003a, Map 2paluxy]
Mean vertical permeability (mD)	k_{cap}	0.01	estimated	Neuzil [1994]; Tokunaga et al. [1998]; Devlin [1998]
Lateral overburden permeability (mD)	\bar{k}_x	100	calculated	Fig. 2
Vertical overburden permeability (mD)	\bar{k}_z	0.02	calculated	Fig. 2
Salinity (ppm)	s	100000	aquifer data	[Hovorka et al., 2003a, Map 12cpaluxy]
CO ₂ solubility (volume fraction)	χ_v	0.05	calculated	Duan and Sun [2003]
Brine density (kg/m ³)	ρ_w	1000	calculated	Batzle and Wang [1992]
CO ₂ density (kg/m ³)	ρ_g	600	calculated	Carbon Capture and Sequestration Technology Center [2003]
Brine density change from diss. (kg/m ³)	$\Delta\rho_d$	7	calculated	Garcia [2001]; Bachu and Adams [2003]
Brine viscosity (mPa s)	μ_w	0.5	calculated	Batzle and Wang [1992]
CO ₂ viscosity (mPa s)	μ_g	0.04	calculated	Carbon Capture and Sequestration Technology Center [2003]
Fracture pressure (MPa)	P_{frac}	30	calculated	Eq. 15,14; Zoback and Zoback [1980a]

^a We found no data on Darcy velocity or hydraulic head in the Paluxy Formation. In the absence of data, we choose a reasonable value based on our experience with other deep saline aquifers. Ultimately, this value is unimportant since slope dominates transport ($N_s \gg N_d$).

St. Peter Sandstone

While the St. Peter Sandstone is widespread in the Mississippi River Valley, we model sequestration only in the Illinois Basin where it is sufficiently deep and well characterized. The structure of the formation in this basin is shown in Figure 34.

The stratigraphy of the St. Peter Sandstone is complicated. It consists of three members whose occurrence and size vary with location: the Kress Member, the Tonti Member, and the Starved Rock Sandstone Member. The Kress Member is the lowermost unit and is present only in central and northern Illinois Basin. It is composed of poorly-sorted, cherty conglomerate, clayey sandstone, and shale. The Tonti Member is the middle member and is generally the most widespread and thickest unit in the St. Peter. It is a fine-grained, very pure quartz arenite. The Starved Rock Sandstone is the uppermost member and is mostly present in the northern and central Illinois Basin. It is a quartz sandstone like the Tonti Member, but is medium-grained and more cross-bedded Young and Siegel [1992]; Willman et al. [1975].

The St. Peter Sandstone is overlain by at least four different formations or groups in different parts of the Illinois Basin: the Dutchtown Limestone [Kolata, 1990, Fig.5-10], the Joachim Dolomite [Kolata, 1990, Fig.5-11], the Platteville Group, and the Glenwood Formation [Willman et al., 1975, p.63]. While these rocks exhibit a variety of different lithologies, we take them as a group to be an aquitard because all of the rocks contain low-permeability layers. For example, the Dutchtown Limestone contains beds of shale; the Joachim Dolomite contains beds of shale, gypsum, and anhydrite; the Platteville Group contains beds of chert and shale; and the uppermost layer in the Glenwood Formation is composed of shale. Other authors have also suggested that at least some of these rocks will act as a caprock Young and Siegel [1992]; Hovorka et al. [2003c]. If this assumption is wrong, the overlying Maquoketa Shale is a well-recognized caprock Young and Siegel [1992]; Mandle and Kontis [1992].

The St. Peter Sandstone is underlain by a variety of rocks since its base is a major regional unconformity [Willman et al., 1975, Fig.O-13]. In the southernmost part of the Illinois Basin, it is underlain by the Everton Dolomite. In the northernmost part of the basin, it is underlain by the Cambrian Potosi Dolomite, Franconia Formation, and Eminance Formation. In most of the remaining parts of the region, the St. Peter is underlain by Ordovician rocks in the Prairie du Chien Group: the Shakopee Dolomite, the New Richmond Sandstone, the Oneota Dolomite, and the Gunter Sandstone [Willman et al., 1975, p.45-60]. Although we do not identify these rocks as a regional aquiclude, we do not consider them for sequestration since their geology is complex and can be very different from the overlying St. Peter Sandstone.

We model sequestration in southern Illinois, as shown in Figure 35. The data for this region are shown in Table 21.

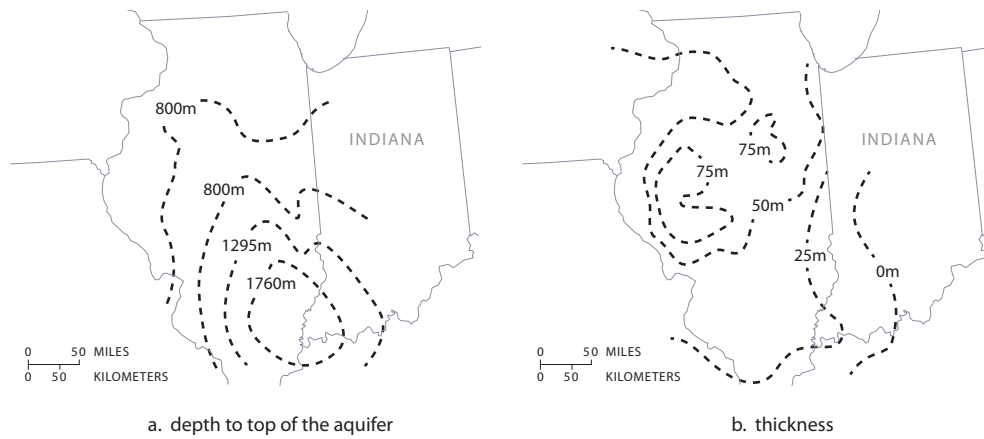


Figure 34: (a) The St. Peter Sandstone dips toward the center of the Illinois Basin in southern Illinois. Modified from [Hovorka et al., 2003a, Map c1stpeter]. (b) Its thickness is highly variable due to irregularities in an unconformity at the base of the formation and post-depositional erosion [Willman et al., 1975, p.62]. In some areas, this erosion has completely removed the St. Peter. Modified from [Hovorka et al., 2003a, Map c3stpeter].

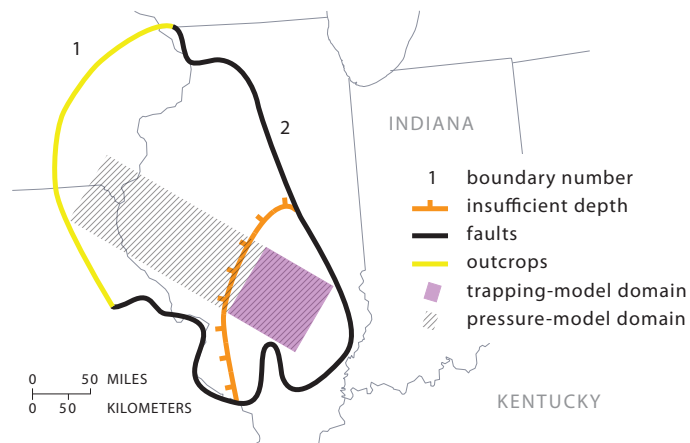


Figure 35: We identify two boundaries that constrain the portion of the St. Peter Sandstone in the Illinois Basin that is suitable for sequestration. Boundary 1 corresponds to the end of the available depth and formation thickness maps [Hovorka et al., 2003a, Maps c1stpeter, c3stpeter]. Boundary 2 corresponds to basin-scale faults King and Beikman [1974].

Table 21: Parameters for the St. Peter Sandstone.

Parameter	Symbol	Value	Data Source	Reference
Residual CO ₂ saturation	S_{rg}	0.3	estimated	Bennion and Bachu [2008]; Oak et al. [1998]
Connate water saturation	S_{wc}	0.4	estimated	Bennion and Bachu [2008]; Oak et al. [1998]
Endpoint relative permeability to CO ₂	k_{rg}^*	0.6	estimated	Bennion and Bachu [2008]; Oak et al. [1998]
Coefficient of CO ₂ -saturated-brine flux	α	0.01	estimated	Kneafsey and Pruess [2010a]; Riaz et al. [2004]
Compressibility (GPa ⁻¹)	c	0.1	estimated	[Wang, 2000, Table C1]
Undrained Poisson ratio	ν	0.3	estimated	[Wang, 2000, Table C1]
Geothermal gradient (°C/km)	G_T	20	aquifer data	Kron and Heiken [1980]; Nathenson and Coker [1998]
Surface temperature (°C)	T_s	10	aquifer data	USs [2010]
Depth to top of aquifer (m)	D	2000	aquifer data	[Hovorka et al., 2003a, Map c1stpeter]
Depth from aquifer to bedrock (m)	B	1000	aquifer data	[Hovorka et al., 2003a, Map c1stpeter]Frederick et al. [2003]
Net aquifer thickness (m)	H	40	aquifer data	[Hovorka et al., 2003a, Map c1stpeter]
Length of trapping-model domain (km)	L_T	100	aquifer data	Fig. 35
Length of pressure-model domain (km)	L_{pres}	400	aquifer data	Fig. 35
Width of well array (km)	W	100	aquifer data	Fig. 35
Porosity	ϕ	0.06	calculated	Hoholick et al. [1984]
Caprock slope (degrees)	ϑ	0.5	calculated	[Hovorka et al., 2003a, Map c1stpeter]
Darcy velocity (cm/yr)	U	1	calculated	[Mandle and Kontis, 1992, Fig.27C]
Aquifer permeability (mD)	k_{aq}	50 ^a	aquifer data	[Mandle and Kontis, 1992, Fig.19C]
Mean vertical permeability (mD)	k_{cap}	0.01	estimated	Neuzil [1994]; Tokunaga et al. [1998]; Devlin et al. [2003]
Lateral overburden permeability (mD)	\bar{k}_x	30	calculated	Fig. 2
Vertical overburden permeability (mD)	\bar{k}_z	0.02	calculated	Fig. 2
Salinity (ppm)	s	100000	aquifer data	[Meents et al., 1952, Fig.13]
CO ₂ solubility (volume fraction)	χ_v	0.05	calculated	MacMinn et al. [2011]; Duan and Sun [2002]
Brine density (kg/m ³)	ρ_w	1000	calculated	Batzle and Wang [1992]
CO ₂ density (kg/m ³)	ρ_g	800	calculated	Carbon Capture and Sequestration Technology Center [2003]
Brine density change from diss. (kg/m ³)	$\Delta\rho_d$	8	calculated	Garcia [2001]; Bachu and Adams [2003]
Brine viscosity (mPa s)	μ_w	1	calculated	Batzle and Wang [1992]
CO ₂ viscosity (mPa s)	μ_g	0.07	calculated	Carbon Capture and Sequestration Technology Center [2003]
Fracture pressure (MPa)	P_{frac}	30	calculated	Eq. 15,14; Zoback and Zoback [1980a]

^a We calculate permeability from mapped values of hydraulic conductivity that range from about 40 to 190 m/yr [Mandle and Kontis, 1992, Fig.19C]. To convert to permeability, we assume a density of 1000 kg/m³ and a viscosity of 0.5 mPa s.

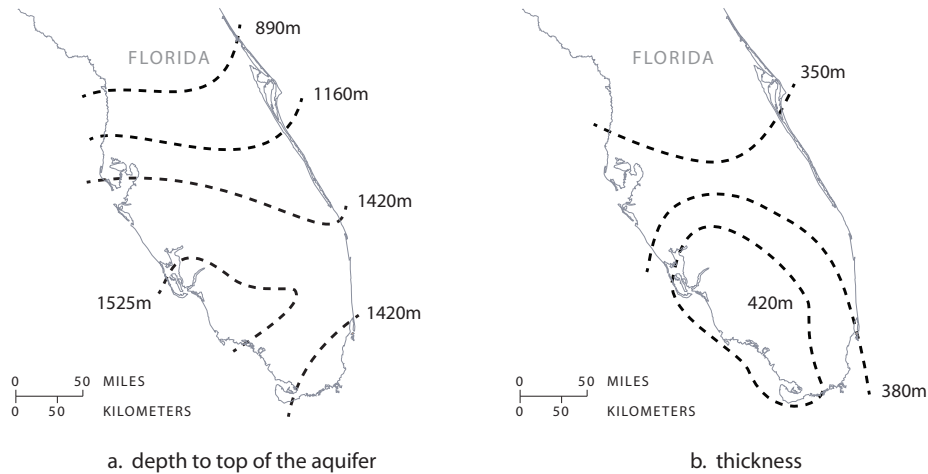


Figure 36: The Cedar Keys and Lawson Dolomites deepen and thicken toward the southwestern part of the Florida peninsula. (a) Modified from [Hovorka et al., 2003a, Map c1cedarkey]. (b) Modified from [Hovorka et al., 2003a, Map c3cedarkeyg].

Cedar Keys and Lawson Dolomites

The Lawson Formation and lower Cedar Keys Formation occur in Florida in the South Florida Basin. The depth to the top of these rocks and their thickness is shown in Figure 36.

The Lawson Formation consists of two members [Applin and Appin, 1944, Table 1]. Its lower member is mostly white chalk that is irregularly interbedded with chalky dolomite or dolomitic chalk. Its upper member is finely to coarsely crystalline dolomite that contains gypsum and anhydrite [Applin and Applin, 1967, p.G26-G27]. The Lawson Formation overlies unnamed carbonate beds of Taylor age. Over the Florida peninsula, these beds consist mostly of chalky dolomite interbedded with few beds of shale or marlstone Applin and Appin [1944]. We choose these beds to be the bottom boundary in our model since we found almost no information about them.

The Lawson Formation is unconformably overlain by the lower Cedar Keys Formation, which consists of limestone Applin and Applin [1967]. It is overlain by the middle Cedar Keys Formation, which consists of massively bedded anhydrite [Hovorka et al., 2003c, p.72]. These anhydrite beds are nearly impermeable and are the caprock in our study Miller [1990].

We model sequestration in the center of the Florida peninsula, as shown in Figure S25. The data for this region is shown in Table 22.

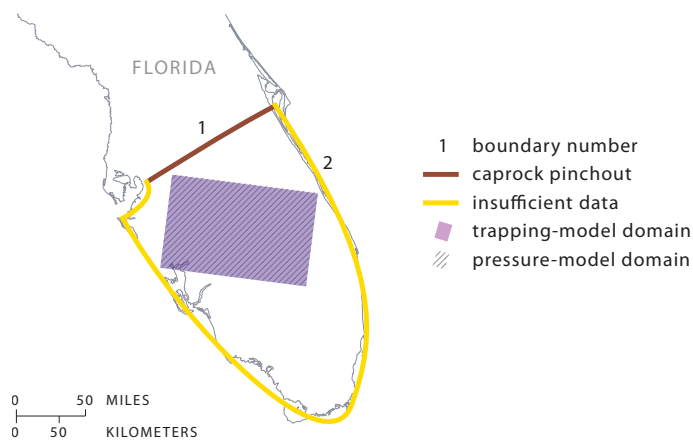


Figure 37: We identify 2 boundaries that constrain the portion of the Cedar Keys and Lawson Dolomites that is suitable for sequestration. Boundary 1 corresponds to the limit of the caprock for the overlying Floridan Aquifer. While maps show that the middle Cedar Keys Formation, which we take as the caprock in this study, does not pinchout here, we put a boundary for safety since the maps are likely very inaccurate Hovorka et al. [2003b]. Boundary 2 corresponds to the edges of the reservoir depth and thickness maps [Hovorka et al., 2003a, Maps c1cedarkey, c3cedarkeyg].

Table 22: Parameters for the Cedar Keys and Lawson Dolomites.

Parameter	Symbol	Value	Data Source	Reference
Residual CO ₂ saturation	S_{rg}	0.3	estimated	Bennion and Bachu [2008]; Oak et al. [1998]
Connate water saturation	S_{wc}	0.4	estimated	Bennion and Bachu [2008]; Oak et al. [1998]
Endpoint relative permeability to CO ₂	k_{rg}^*	0.6	estimated	Bennion and Bachu [2008]; Oak et al. [1998]
Coefficient of CO ₂ -saturated-brine flux	α	0.01	estimated	Kneafsey and Pruess [2010a]; Riaz et al. [2007]
Compressibility (GPa ⁻¹)	c	0.1	estimated	[Wang, 2000, Table C1]
Undrained Poisson ratio	ν	0.3	estimated	[Wang, 2000, Table C1]
Geothermal gradient (°C/km)	G_T	20	aquifer data	Kron and Heiken [1980]; Nathenson and C
Surface temperature (°C)	T_s	20	aquifer data	USs [2010]
Depth to top of aquifer (m)	D	2000	aquifer data	[Hovorka et al., 2003a, Map c1cedarkey]
Depth from aquifer to bedrock (m)	B	2000	aquifer data	Frezon et al. [1983]Hovorka et al. [2003a]
Net aquifer thickness (m)	H	400	aquifer data	[Hovorka et al., 2003a, Map c3cedarkeyg]
Length of trapping-model domain (km)	L_T	100	aquifer data	Fig. S25
Length of pressure-model domain (km)	L_{pres}	100	aquifer data	Fig. S25
Width of well array (km)	W	200	aquifer data	Fig. S25
Porosity	ϕ	0.2	aquifer data	Hovorka et al. [2003c]
Caprock slope (degrees)	ϑ	0.2	calculated	[Hovorka et al., 2003a, Map c1cedarkey]
Darcy velocity (cm/yr)	U	0 ^a	estimated	
Aquifer permeability (mD)	k_{aq}	10	aquifer data	Hovorka et al. [2003c]
Mean vertical permeability (mD)	k_{cap}	0.01	estimated	Neuzil [1994]; Tokunaga et al. [1998]; Dew
Lateral overburden permeability (mD)	\bar{k}_x	5	calculated	Fig. 2
Vertical overburden permeability (mD)	\bar{k}_z	0.02	calculated	Fig. 2
Salinity (g/L)	s	100 ^b	aquifer data	Hovorka et al. [2003c]
CO ₂ solubility (volume fraction)	χ_v	0.05	calculated	Duan and Sun [2003]
Brine density (kg/m ³)	ρ_w	1000	calculated	Batzle and Wang [1992]
CO ₂ density (kg/m ³)	ρ_g	800	calculated	Carbon Capture and Sequestration Techn
Brine density change from diss. (kg/m ³)	$\Delta\rho_d$	8	calculated	Garcia [2001]; Bachu and Adams [2003]
Brine viscosity (mPa s)	μ_w	0.7	calculated	Batzle and Wang [1992]
CO ₂ viscosity (mPa s)	μ_g	0.07	calculated	Carbon Capture and Sequestration Techn
Fracture pressure (MPa)	P_{frac}	30	calculated	Eq. 15,14; Zoback and Zoback [1980a]

^a We found no data on Darcy velocity or hydraulic head in the Cedar Keys and Lawson Dolomites. In the absence of data, we set the Darcy velocity to zero. However, since the slope of the aquifer is small ($\theta = 0.18$), a nonzero velocity may change the results. Darcy velocity has the same magnitude as that in the overlying Floridan aquifer ($U = 1.8$ cm/yr [Miller, 1990, Fig.60]), thus, the ground water flow is not negligible.

^b We found no data on salinity in the Cedar Keys and Lawson Dolomites. However, some data are available for the overlying formations: brine in the overlying Upper Floridan Aquifer has a salinity of a few grams per liter [Miller, 1990, Fig.68], the underlying Sunniland Limestone has a salinity of a few hundred grams per liter. For the salinity of brine in the Cedar Keys and Lawson Dolomites, we choose a middle value of 100 g/L.

4 Estimation of CO₂ storage capacity and injectivity

4.1 Sensitivity analysis on model parameters

Because hydrogeologic data for saline aquifers are highly uncertain, we analyze the sensitivity of both the migration model and the pressure model to variations in their input parameters. We calculate the relative sensitivity of the capacity of an aquifer C to a parameter \mathcal{P} as:

$$\tilde{S} = \frac{\mathcal{P}_0}{C_0} \frac{\partial C}{\partial \mathcal{P}} \Big|_{\mathcal{P}_0}, \quad (82)$$

where \mathcal{P}_0 is the baseline value of the parameter and C_0 is the baseline capacity. The baseline for each aquifer is the set of parameter values given in previous reports. For the pressure model, the baseline values and the sensitivities depend on the injection time. We assess the sensitivity for each aquifer at three different injection times— $T = 50, 100,$ and 150 years—to define three baselines. These injection times bracket the key time horizon in our study, 100 years.

For both the migration model and the pressure model, the relative sensitivities vary between -1 and 2 within individual aquifers, indicating the relative importance of some parameters over others. For example, the migration model is highly sensitive to the width of the well array, W , the length of the model domain, L , and the aquifer thickness, H —key parameters for calculating an aquifer’s pore volume—but is relatively insensitive to the aquifer permeability, k_{aq} . The pressure model is highly sensitive to the aquifer depth, D , and the average density of the overburden, $\bar{\rho}_o$ —two key parameters for calculating the fracture pressure—but is relatively insensitive to salinity, s . All sensitivities for the migration model are listed in Table 23; all sensitivities for the pressure model are listed in Table 24.

Table 23: Sensitivity of the migration model to its input parameters.

Reservoir	Region	W	H	D	T_s	G	$\bar{\rho}_w$	s	k_{aq}	ϕ	S_{wc}	S_{gr}	k_{gr}^*	α	θ	U	L_T
Mt. Simon	a	1	0.49	0.71	0.1	-0.75	0.19	-0.73	0	1	-0.097	0.87	-0.85	0.54	-0.46	0	1.6
Mt. Simon	b	1	0.64	0.72	0.094	-0.53	0.17	-0.78	0.021	1	0.12	1.2	-0.82	0.37	-0.31	-0.021	1.4
Mt. Simon	c	1	1	0.74	0.17	-0.51	0.0052	-0.15	0.0071	1	-0.49	0.0086	-0.93	0	0.0071	0.17	1
Black Warrior River	a	1	0.77	0.77	0.19	-2.1	0.054	-0.34	0	1	0.44	1.7	-0.89	0.2	-0.2	0	1.2
Black Warrior River	b	1	0.88	0.56	0.14	-0.73	0.061	-0.069	0	1	-0.51	0.068	-0.76	0.069	-0.1	-0.013	1.1
Black Warrior River	c	1	0.91	0.46	0.14	-0.7	0.034	-0.028	0	1	-0.64	0.031	-0.92	-0.018	-0.078	0	0.98
Black Warrior River	d	1	0.94	0.73	0.22	-1.6	0.032	-0.18	0	1	0.65	2	-0.86	0.084	-0.056	0	1.1
Frio	a	1	0.99	1.7	0.27	-1.1	-0.0058	-0.14	0.0044	1	0.71	2.1	-0.77	0.014	-0.031	0	1
Frio	b	1	0.94	1.7	0.23	-1.2	0.025	-0.15	0	1	0.69	2.1	-0.76	0.038	-0.059	0	1
Frio	c	1	1	1.2	0.22	-1	0.011	-0.15	0.0012	1	0.72	2.1	-0.84	0.015	0.0091	0.0013	1
Madison	a	1	0.92	1.2	0.047	-0.59	0.064	-0.25	0.0067	1	0.6	1.9	-0.82	0.075	-0.067	-0.0013	1.1
Madison	b	1	0.78	1.5	-0.012	-0.75	0.15	-0.44	-0.017	1	0.53	1.7	-1	0.14	-0.16	-0.086	1.1
Navajo-Nugget	a	1	0.78	0.98	-0.035	-0.48	-0.034	-0.15	0	1	0.61	1.9	-0.83	0.13	-0.2	0	1.1
Navajo-Nugget	b	1	0.67	1.1	0.077	-0.54	0.22	-0.21	0	1	0.28	1.4	-0.76	0.36	-0.3	0	1.4
Morrison		1	0.56	1	0.085	-0.83	0.18	-0.056	0	1	0.1	1.2	-0.81	0.43	-0.4	0	1.5
Potomac		1	0.53	2.6	0.11	-2.3	0.17	-0.039	-0.0082	1	0.0031	1	-0.89	0.47	-0.44	0.011	1.5
Fox Hills		1	0.54	2.6	0.11	-2.3	0.16	-0.012	0	1	0.011	1	-0.88	0.46	-0.42	0	1.5
Paluxy		1	0.39	1.3	0.089	-1	0.52	-0.72	0	1	-0.31	0.54	-0.84	0.62	-0.55	0	1.7
St. Peter		1	0.89	0.26	0.073	-0.39	0.053	-0.29	0	1	-0.12	0.37	-0.66	0.036	-0.1	0	1
Cedar Keys		1	0.64	0.64	0.13	-0.5	0.17	-0.43	0	1	-0.36	0.31	-0.69	0.25	-0.33	0	1.3

Table 24: Sensitivity of the pressure model to its input parameters for three different injection times.

Reservoir	Region	T (years)	W	H	D	T _s	G	$\bar{\rho}_w$	s	k _{aq}	k _{cap}	c	ν	$\bar{\rho}$	B	L _{Pmin}	L _{Pmax}	
Mt. Simon	a	50	1	0.64	1.4	0.11	-0.027	-0.77	-0.16	0.5	0.18	0.32	0	1.8	0	0	0	0
		100	1	0.58	1.4	0.11	-0.013	-0.77	-0.17	0.5	0.21	0.29	0	1.8	0	0	0	0
		150	1	0.55	1.4	0.12	-0.0025	-0.77	-0.18	0.5	0.23	0.26	0	1.8	0	0	0	0
Mt. Simon	b	50	1	0.48	1.5	0.099	0.085	-0.77	-0.24	0.5	0.26	0.24	0	1.8	0	0	0	0
		100	1	0.41	1.5	0.1	0.092	-0.77	-0.25	0.5	0.3	0.2	0	1.8	0	0	0	0
		150	1	0.38	1.5	0.11	0.1	-0.77	-0.26	0.5	0.32	0.18	0	1.8	0	0	0	0
Mt. Simon	c	50	1	0.48	1.4	0.12	-0.049	-0.77	-0.26	0.5	0.26	0.24	0	1.8	0	0	0.00071	0
		100	1	0.43	1.4	0.12	-0.037	-0.77	-0.27	0.5	0.29	0.22	0	1.8	0	0	0.0075	0
		150	1	0.41	1.4	0.13	-0.027	-0.77	-0.26	0.5	0.32	0.21	0	1.8	0	0	0.025	0
Black Warrior River	a	50	1	0.77	1.3	0.17	-0.79	-0.77	-0.1	0.32	0.12	0.38	1.4	1.8	0	0	0	0
		100	1	0.73	1.1	0.12	-0.84	-0.77	-0.11	0.5	0.18	0.31	1.4	1.8	0	0	0	0
		150	1	0.68	0.87	0.081	-1.3	-0.77	-0.12	0.6	0.24	0.25	1.4	1.8	0	0	0	0
Black Warrior River	b	50	1	0.57	1.4	0.26	-0.18	-0.77	-0.032	0.46	0.23	0.27	1.4	1.8	0	0	0.038	0
		100	1	0.48	1.3	0.28	-0.15	-0.77	-0.035	0.4	0.3	0.2	1.4	1.8	0	0	0.097	-0.00087
		150	1	0.43	1.3	0.3	-0.13	-0.77	-0.038	0.37	0.36	0.14	1.4	1.8	0	0	0.13	-0.0033
Black Warrior River	c	50	1	0.46	1.4	0.26	-0.16	-0.77	-0.0061	0.49	0.28	0.23	1.4	1.8	0	0	0.023	0.027
		100	1	0.42	1.3	0.26	-0.17	-0.77	-0.0066	0.46	0.36	0.17	1.4	1.8	0	0	0.067	0.06
		150	1	0.39	1.2	0.26	-0.16	-0.77	-0.0072	0.45	0.43	0.12	1.4	1.8	0	0	0.097	0.079
Black Warrior River	d	50	1	0.79	1.4	0.16	-0.61	-0.77	-0.086	0.5	0.11	0.39	1.4	1.8	0	0	0	0
		100	1	0.73	1.4	0.17	-0.59	-0.77	-0.092	0.5	0.15	0.35	1.4	1.8	0	0	0	0
		150	1	0.68	1.4	0.18	-0.57	-0.77	-0.098	0.5	0.19	0.31	1.4	1.8	0	0	0	0
Frio	a	50	1	0.7	2.1	0.18	-0.52	-0.77	-0.092	0.56	0.15	0.29	1.4	1.8	0	0	0	-0.18
		100	1	0.67	2.1	0.18	-0.45	-0.77	-0.094	0.62	0.17	0.21	1.4	1.8	0	0	0	-0.36
		150	1	0.66	2.2	0.19	-0.41	-0.77	-0.095	0.66	0.17	0.17	1.4	1.8	0	0	0	-0.47
Frio	b	50	1	0.59	2.1	0.19	-0.51	-0.77	-0.099	0.54	0.2	0.26	1.4	1.8	0	0	0	-0.12
		100	1	0.55	2.1	0.2	-0.45	-0.77	-0.1	0.59	0.22	0.18	1.4	1.8	0	0	0	-0.27
		150	1	0.54	2.1	0.2	-0.41	-0.77	-0.1	0.62	0.23	0.15	1.4	1.8	0	0	0	-0.36
Frio	c	50	1	0.51	1.8	0.19	-0.4	-0.77	-0.14	0.5	0.14	0.25	1.4	1.8	0	0	0	-0.00064
		100	1	0.47	1.8	0.19	-0.38	-0.77	-0.14	0.5	0.28	0.22	1.4	1.8	0	0	0	-0.011
		150	1	0.45	1.8	0.2	-0.36	-0.77	-0.15	0.51	0.31	0.18	1.4	1.8	0.00048	0	-0.032	
Madison	a	50	1	0.53	1.8	0.041	-0.031	-0.77	-0.13	0.49	0.23	0.27	0	1.8	0.0013	0	0.0042	
		100	1	0.45	1.8	0.042	-0.0052	-0.77	-0.14	0.5	0.26	0.24	0	1.8	0.015	0	0.031	
		150	1	0.4	1.8	0.043	-0.00027	-0.77	-0.14	0.5	0.26	0.24	0	1.8	0.036	0.00064	0.061	
Madison	b	50	1	0.46	1.1	0.056	-0.93	-0.77	-0.15	-0.35	0.26	0.23	0	1.8	0.011	0	0	
		100	1	0.39	1.1	0.057	-0.89	-0.77	-0.15	-0.32	0.27	0.22	0	1.8	0.06	0	0	
		150	1	0.36	1.1	0.057	-0.86	-0.77	-0.15	-0.29	0.27	0.22	0	1.8	0.1	0	0	
Navajo-Nugget	a	50	1	0.32	1.9	0.056	0.26	-0.77	-0.13	0.5	0.34	0.16	0	1.8	0	0	0.00044	
		100	1	0.28	1.9	0.057	0.27	-0.77	-0.13	0.5	0.36	0.14	0	1.8	0	0	0.0093	
		150	1	0.27	1.9	0.058	0.27	-0.77	-0.13	0.49	0.37	0.14	0	1.8	0	0	0.028	
Navajo-Nugget	b	50	1	0.43	1.6	0.087	0.005	-0.77	-0.12	0.33	0.29	0.21	0	1.8	0.14	0	0	
		100	1	0.43	1.6	0.087	0.0047	-0.77	-0.12	0.33	0.28	0.22	0	1.8	0.22	0	0	
		150	1	0.43	1.6	0.087	0.0044	-0.77	-0.12	0.34	0.29	0.21	0	1.8	0.26	0.00028	0.00055	
Morrisson		50	1	0.36	1.8	0.11	0.063	-0.77	-0.031	0.5	0.3	0.2	0	1.8	0.041	0.16	0	
		100	1	0.31	1.9	0.11	0.061	-0.77	-0.03	0.5	0.3	0.2	0	1.8	0.11	0.26	0	
		150	1	0.27	1.9	0.11	0.065	-0.77	-0.031	0.5	0.3	0.2	0	1.8	0.15	0.32	0.00067	
Potomac		50	1	0.43	2.4	0.15	-1.3	-0.77	-0.022	0.29	0.32	0.39	0	1.8	0	0.2	0.4	
		100	1	0.31	2.2	0.17	-1.3	-0.77	-0.026	0.26	0.47	0.27	0	1.8	0	0.24	0.48	
		150	1	0.24	2.1	0.19	-1.3	-0.77	-0.029	0.25	0.57	0.18	0	1.8	0	0.25	0.49	
Fox Hills		50	1	0.36	2.6	0.15	-1.1	-0.77	-0.011	0.5	0.34	0.16	0	1.8	0	0	0.67	
		100	1	0.36	2.7	0.16	-1.1	-0.77	-0.012	0.5	0.39	0.11	0	1.8	0	0	0.65	
		150	1	0.37	2.7	0.17	-1.1	-0.77	-0.012	0.5	0.42	0.08	0	1.8	0	0	0.63	
Paluxy		50	1	0.27	1.7	0.16	-0.13	-0.77	-0.21	0.47	0.36	0.15	1.4	1.8	0	0	0.025	0.028
		100	1	0.24	1.7	0.17	-0.14	-0.77	-0.23	0.44	0.38	0.15	1.4	1.8	0	0	0.072	0.06
		150	1	0.23	1.7	0.17	-0.15	-0.77	-0.23	0.42	0.4	0.16	1.4	1.8	0.00051	0.11	0.081	
St. Peter		50	1	0.27	1.4	0.15	0.046	-0.77	-0.16	0.5	0.36	0.14	0	1.8	0.0022	0	0	
		100	1	0.24	1.4	0.15	0.049	-0.77	-0.16	0.5	0.37	0.13	0	1.8	0.017	0.00012	0	
		150	1	0.23	1.4	0.15	0.049	-0.77	-0.16	0.5	0.37	0.13	0	1.8	0.035	0.0015	0	
Cedar Keys		50	1	0.5	1.4	0.19	0.051	-0.77	-0.13	0.5	0.25	0.25	1.4	1.8	0	0	0	
		100	1	0.45	1.4	0.2	0.063	-0.77	-0.13	0.5	0.27	0.23	1.4	1.8	0.00079	0	0	
		150	1	0.43	1.4	0.2	0.069	-0.77	-0.14	0.5	0.28	0.22	1.4	1.8	0.0037	0	0	

4.2 Probability distributions for parameters with greatest impact

To quantify uncertainty in the hydrogeologic properties of an aquifer, we estimate a low and high value for each input parameter using one of three methods. This is a simplification of hydrogeologic uncertainty, since in reality each parameter would be associated with a probability density function (PDF) of possible values. We use this simplified approach here because detailed PDFs are not available.

We estimate the low and high values of each parameter using one of three methods. For some parameters, such as surface temperature and geothermal gradient, we estimate an absolute uncertainty $\Delta\mathcal{P}$ and apply it symmetrically about the baseline value, so that the low and high values of a parameter \mathcal{P} with baseline value \mathcal{P}_0 will be $\mathcal{P}_{\text{low}} = \mathcal{P}_0 - \Delta\mathcal{P}/2$ and $\mathcal{P}_{\text{high}} = \mathcal{P}_0 + \Delta\mathcal{P}/2$, respectively (Table 25). For other parameters, such as aquifer depth and thickness, we estimate a relative uncertainty ψ and apply it symmetrically about the baseline value, so that the low and high values will be $\mathcal{P}_{\text{low}} = (1 - \psi/2)\mathcal{P}_0$ and $\mathcal{P}_{\text{high}} = (1 + \psi/2)\mathcal{P}_0$, respectively (Table 26). The remaining parameters—the groundwater velocity, compressibility, and permeability of the aquifer and caprock—are often assumed to be log-normally distributed, so we estimate a relative uncertainty Ψ in the log of the parameter. The corresponding low and high values will then be $\mathcal{P}_{\text{low}} = \mathcal{P}_0^{1+\Psi/2}$ and $\mathcal{P}_{\text{high}} = \mathcal{P}_0^{1-\Psi/2}$. We take the relative uncertainty in the log to be $\Psi = 0.03$ for all of these log-normally distributed parameters.

Table 25: Parameters for which we estimate an absolute uncertainty, and corresponding absolute uncertainties $\Delta\mathcal{P}$.

Parameter	Symbol	$\Delta\mathcal{P}$
Connate water saturation [–]	S_{wc}	0.2
Residual CO ₂ saturation [–]	S_{gr}	0.2
Endpoint relative permeability to CO ₂ [–]	k_{gr}^*	0.2
Coefficient of CO ₂ -saturated-brine flux [–]	α	0.002
Average density of water in overburden [kg/m ³]	$\overline{\rho}_w$	20
Average density of overburden [kg/m ³]	$\overline{\rho}_o$	230
Surface temperature [°C]	T_s	1
Geothermal gradient [°C/km]	G	2

Table 26: Parameters for which we estimate a relative uncertainty, and corresponding relative uncertainties $\psi = \Delta\mathcal{P}/\mathcal{P}$.

Parameter	Symbol	ψ
Depth to top of aquifer	D	0.2
Depth from aquifer to bedrock	B	0.2
Net aquifer thickness	H	0.2
Width of well array	W	0.1
Length of model domain	L_t	0.1
Distance from well array to closest pressure boundary	L_{Pmin}	0.1
Distance from well array to farthest pressure boundary	L_{Pmax}	0.1
Porosity	ϕ	0.4
Caprock slope	ϑ	0.2
Salinity	s	0.1

4.3 Uncertainty analysis

Uncertainty in the hydrogeologic properties of an aquifer leads to uncertainty in its storage capacity. We use the low, baseline, and high values of each parameter estimated in the previous section to calculate the uncertainty in each aquifer’s storage capacity with two different methods.

In the Extrema Method, we calculate low and high values of the capacity by choosing the set of parameter values that will give the lowest capacity and the set that will give the highest capacity. To do so, we choose either the low or high value of each parameter as driven by the sensitivity analysis: to calculate the high capacity, for example, we take the high value of all parameters to which the capacity has a positive sensitivity, and the low value of all parameters to which the capacity has a negative sensitivity.

In the PDF Method, we generate a PDF for the capacity by estimating the capacity for every possible combination of the low, baseline, and high values of the parameters. The uncertainty in the capacity is then the standard deviation of this PDF. Since using the migration and pressure models to calculate the capacity for every parameter combination is computationally infeasible, we instead extrapolate the capacity for each combination using the sensitivity analysis:

$$C = C_0 + \tilde{S}_{\mathcal{P}_1}\Delta\mathcal{P}_1 + \tilde{S}_{\mathcal{P}_2}\Delta\mathcal{P}_2 + \tilde{S}_{\mathcal{P}_3}\Delta\mathcal{P}_3 + \dots, \quad (83)$$

where the $\Delta\mathcal{P}_i = \mathcal{P}_i - \mathcal{P}_{i,0}$, $i = 1 \dots N$, are the uncertainties in the N input parameters and $\tilde{S}_{\mathcal{P}_i}$ are the associated sensitivities. Using Eq. (83), we calculate a capacity for every possible combination of the low, baseline, and high values of each parameter for all $N = 16$ input parameters, generating $3^{16} \approx 43 \times 10^6$ values of capacity that compose the approximate PDF of capacity.

We calculate the uncertainties in the migration-limited capacity and the pressure-limited capacity independently. For the migration-limited capacity, the low capacities derived from the Extrema Method, C_l , are about 20–40% of the baseline capacity, and the high capacities, C_h , are about 200–350% of the baseline capacity (Table 27). From the PDF Method, the probability density functions are symmetric because the uncertainties in most of the input parameters are symmetric, and those with asymmetric uncertainties (Darcy velocity and permeability) exhibit low sensitivities (Figure 38). As a result, the mean capacities from these distributions, \bar{C} , are nearly the same as the baseline capacities, C_0 . One standard deviation, σ_C , is about 30–45% of the baseline capacity, and the upper end of the uncertainty window calculated from one standard deviation— $\bar{C} + \sigma_C$ —is then about 130 to 145% of the baseline capacity (Table 27).

We use one standard deviation as the appropriate measure of uncertainty from the PDF Method for both migration-limited and pressure-limited capacities. We do not use two standard deviations because the uncertainty window derived from two standard deviations is typically large to the point of being meaningless: for most of the well arrays, the lower end of the uncertainty window is below the low capacity from the Extrema Method, and in at least one case goes to zero (Figures 39 & 41). Indeed, the approximate probability density functions from which they are calculated often reach into negative capacities, indicating that the lower ends of the uncertainty windows derived from them are also too low (Figures 38 & 40). The upper ends of the uncertainty windows are likely also too low, since the high

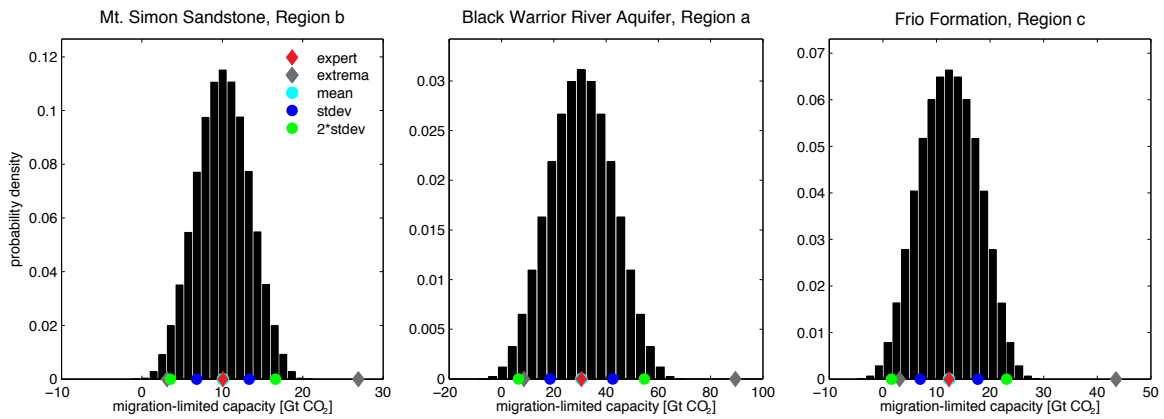


Figure 38: Approximate probability density functions for the migration-limited capacity of three well arrays.

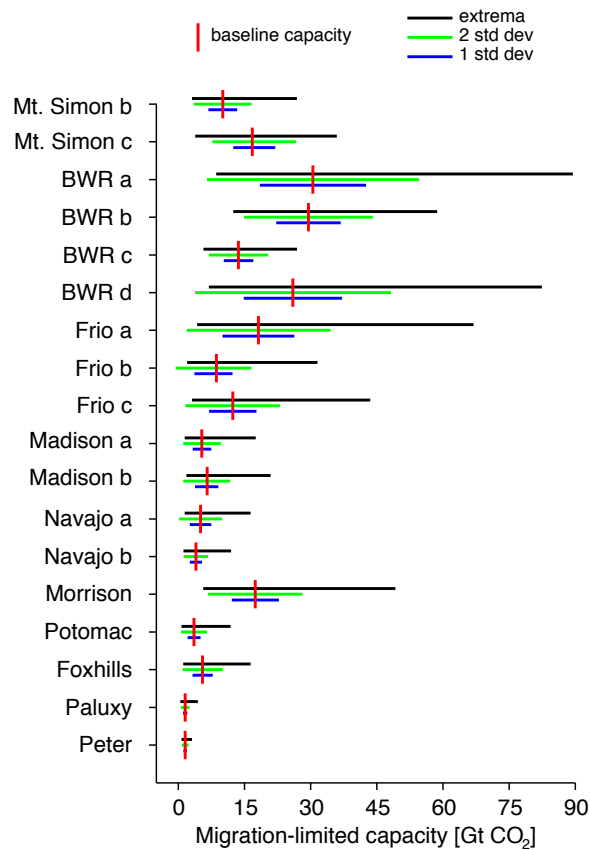


Figure 39: The baseline migration-limited capacity and three measures of uncertainty for nearly all the well arrays in the study. We do not show Mt. Simon, Region a or Cedar Keys because their baseline capacities and uncertainties are so large that the data for other aquifers becomes obscured.

Table 27: Uncertainty in migration-limited capacity.

Reservoir	Region	C_0	\bar{C}	$\frac{\bar{C}-C_0}{C_0}$	σ_C	$\frac{\sigma_C}{C_0}$	C_l	$\frac{C_l-C_0}{C_0}$	C_h	$\frac{C_h-C_0}{C_0}$
Mt. Simon	a	88	88	0	27	0.31	29	-0.67	250	1.8
Mt. Simon	b	10	10	0	3.3	0.32	3.1	-0.69	27	1.7
Mt. Simon	c	17	17	0.027	4.8	0.28	3.8	-0.77	36	1.1
Black Warrior River	a	31	31	0	12	0.39	8.6	-0.72	89	1.9
Black Warrior River	b	30	30	0	7.3	0.25	12	-0.58	59	0.99
Black Warrior River	c	14	14	0	3.4	0.25	5.7	-0.58	27	0.97
Black Warrior River	d	26	26	0	11	0.43	6.9	-0.73	82	2.2
Frio	a	18	18	0	8.1	0.45	4.3	-0.77	67	2.7
Frio	b	8.6	8	-0.075	4.3	0.5	2	-0.76	32	2.7
Frio	c	12	12	0	5.4	0.44	3.1	-0.75	44	2.5
Madison	a	5.3	5.4	0.015	2.1	0.4	1.4	-0.73	18	2.3
Madison	b	6.6	6.4	-0.016	2.7	0.41	1.8	-0.72	21	2.2
Navajo-Nugget	a	5.1	5.1	0	2.4	0.48	1.4	-0.72	16	2.2
Navajo-Nugget	b	4	4	0	1.4	0.35	1.2	-0.7	12	2
Morrison		17	17	0	5.3	0.31	5.7	-0.68	49	1.8
Potomac		3.6	3.6	0.0038	1.5	0.42	0.74	-0.79	12	2.3
Foxhills		5.5	5.5	0	2.3	0.42	1.1	-0.79	16	2
Paluxy		1.5	1.5	0	0.5	0.32	0.47	-0.7	4.4	1.9
St. Peter		1.6	1.6	0	0.38	0.24	0.72	-0.55	3.1	0.97
Cedar Keys		87	87	0	22	0.25	38	-0.57	180	1.1

capacity from the Extrema Method suggests that the true probability density function is skewed to the right.

For the pressure-limited capacity, the low capacities derived from the Extrema Method are generally 30% of the baseline capacity, and the high capacities are generally 300 to 400% of the baseline capacity (Table 28). Compared with the migration-limited capacity, the high capacities are typically a larger fraction of the baseline capacity because the pressure model has more input parameters with large uncertainty, such as the compressibility and caprock permeability, and is more sensitive to the shared parameters with large uncertainties, such as the aquifer permeability. These parameters with large-uncertainties also have asymmetric uncertainties, and cause the capacity distributions obtained from the PDF Method to be asymmetric and often multi-peaked (Figure 40). As a result, the mean capacities from these distributions, \bar{C} , are different from the baseline capacities, C_0 (Figure 41). One standard deviation, σ_C , is about 50 – 60% of the baseline capacity, leading to error windows that are about 100 – 120% of the baseline capacity (Table 28).

We extend the uncertainty results from one injection time to all injection times by pro-rating. We calculate the high and low capacities from the Extrema Method at all injection times as:

$$C_l(T) = C_0(T) \frac{C_l(100 \text{ yrs})}{C_0(100 \text{ yrs})}, \quad C_h(T) = C_0(T) \frac{C_h(100 \text{ yrs})}{C_0(100 \text{ yrs})}, \quad (84)$$

where $C_l(T)$ and $C_h(T)$ are the low and high capacities at any injection time, T , respectively; $C_l(100 \text{ yrs})$ and $C_h(100 \text{ yrs})$ are the low and high capacities for an injection time of 100 years,

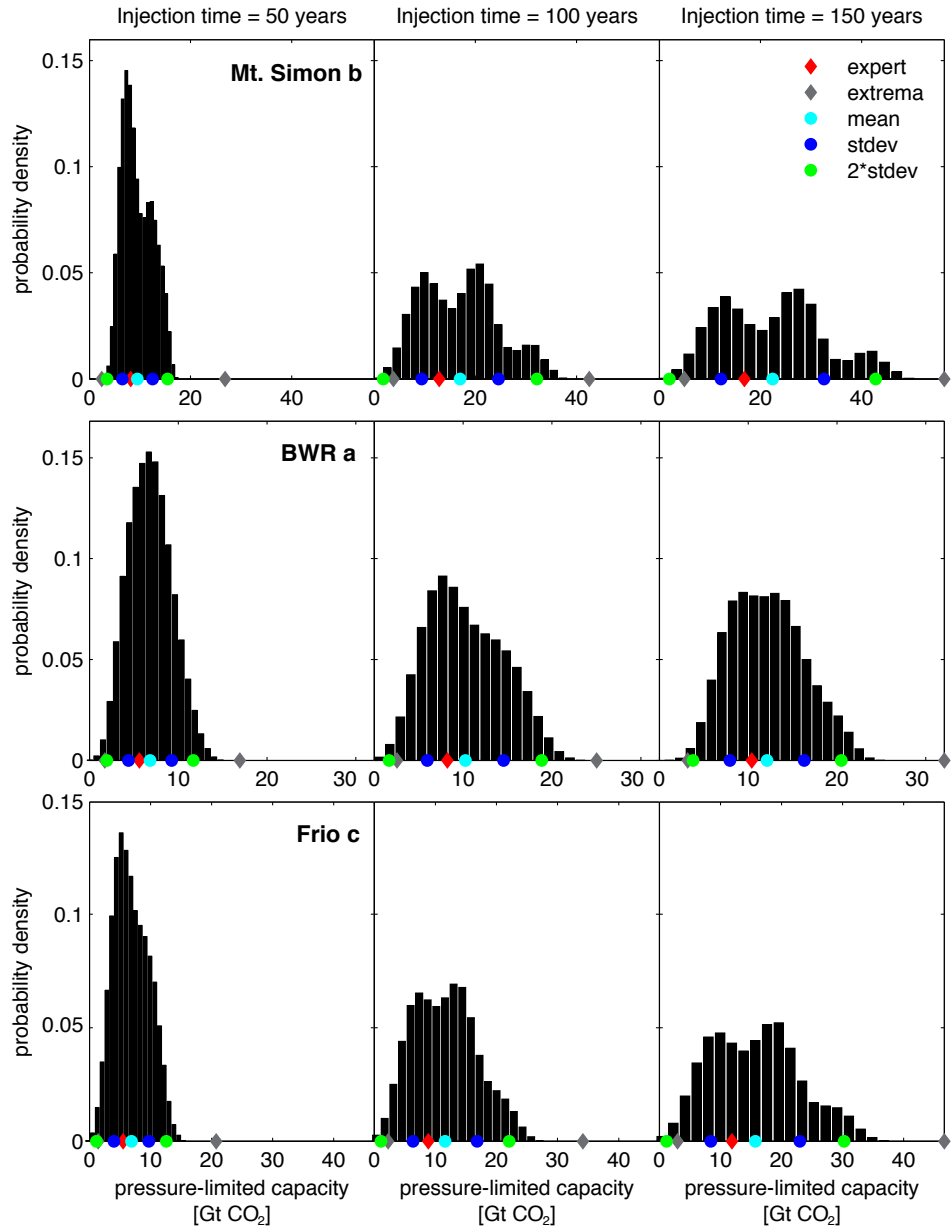


Figure 40: Approximate probability density functions for the pressure-limited capacity of three well arrays.

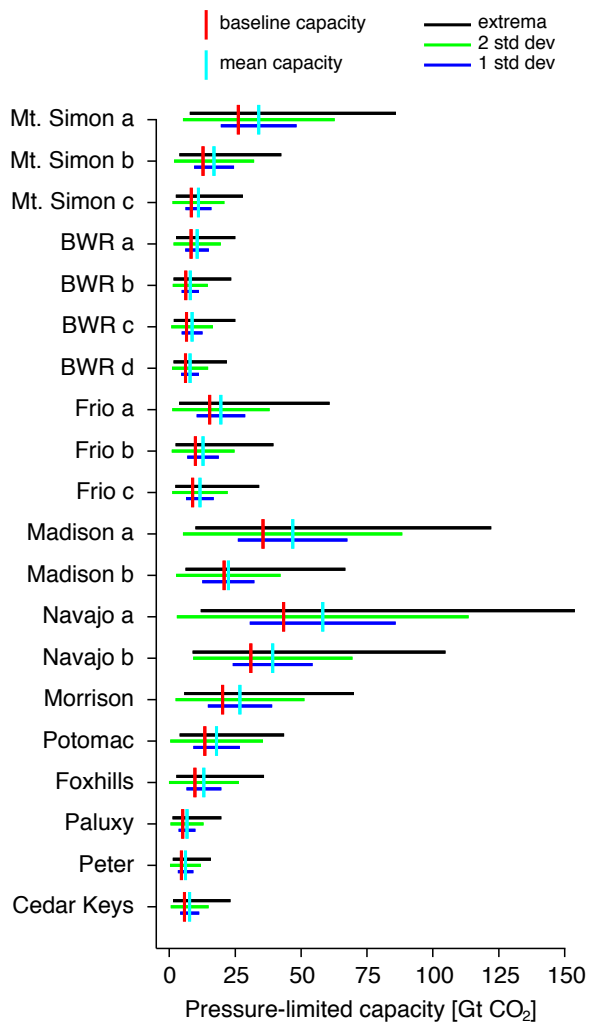


Figure 41: The baseline and mean pressure-limited capacity with three measures of uncertainty for all well arrays.

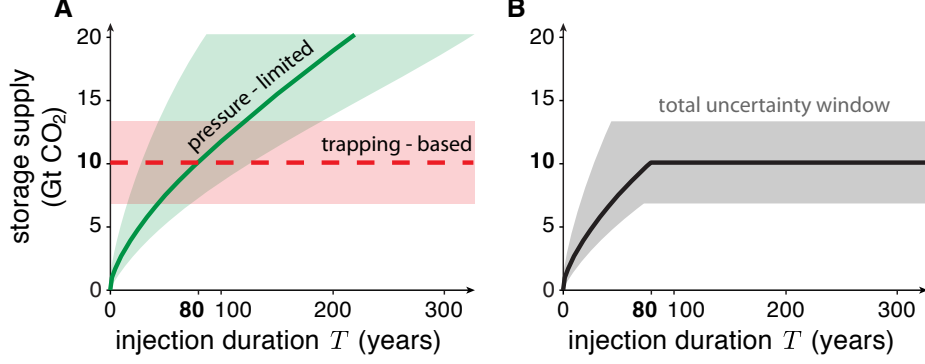


Figure 42: **(A)** The migration-limited and pressure-limited capacity for Region **b** of the Mt. Simon Sandstone, with uncertainty windows based on one standard deviation of the approximate PDF. **(B)** The total uncertainty window combines the uncertainties from both types of capacity. The upper boundary of the window corresponds to the lowermost of the two upper boundaries, and the lower boundary corresponds to the lowermost of the two lower boundaries.

respectively; and $C_0(100 \text{ yrs})$ is the baseline capacity for an injection time of 100 years. We choose to prorate based on the results at 100 years because that is the important time horizon in our study; the results obtained by prorating from an average of the results at 50, 100, and 150 years are extremely similar. We calculate the uncertainty window from the PDF Method at all injection times as:

$$C_{\mp\sigma}(T) = C_0(T) \frac{\overline{C}(100 \text{ yrs}) \mp \sigma_C(100 \text{ yrs})}{C_0(100 \text{ yrs})}, \quad (85)$$

where $C_{-\sigma}(T)$ and $C_{+\sigma}(T)$ are, respectively, the lower and upper ends of the uncertainty window based on one standard deviation at all injection times, T ; $\overline{C}(100 \text{ yrs})$ is the mean capacity at an injection time of 100 years; and $\sigma_C(100 \text{ yrs})$ is the standard deviation at an injection time of 100 years.

To construct the complete uncertainty window for a particular aquifer, we combine the uncertainties from the migration-limited and pressure-limited capacities, as shown in Figure 42. To construct the complete uncertainty window for the entire US storage supply, we combine the uncertainties from all the aquifers.

Table 28: Uncertainty in pressure-limited capacity.

Reservoir	Region	T	C_0	\bar{C}	$\frac{\bar{C}-C_0}{C_0}$	σ_C	$\frac{\sigma_C}{C_0}$	C_t	$\frac{C_t-C_0}{C_0}$	C_h	$\frac{C_h-C_0}{C_0}$
Mt. Simon	a	50	16	21	0.29	8.8	0.54	4.9	-0.7	53	2.2
		100	26	34	0.3	14	0.55	7.8	-0.7	86	2.3
		150	35	46	0.3	20	0.56	10	-0.7	120	2.3
Mt. Simon	b	50	8.2	11	0.31	4.7	0.57	2.4	-0.7	27	2.3
		100	13	17	0.32	7.6	0.59	3.8	-0.7	43	2.3
		150	17	22	0.33	10	0.61	5	-0.71	56	2.3
Mt. Simon	c	50	4.9	6.4	0.31	2.8	0.57	1.5	-0.7	16	2.3
		100	8.4	11	0.32	4.9	0.59	2.5	-0.71	28	2.3
		150	12	15	0.33	7	0.61	3.4	-0.71	39	2.4
Black Warrior River	a	50	5.6	6.8	0.21	2.4	0.43	1.7	-0.69	17	2
		100	8.2	11	0.28	4.5	0.54	2.6	-0.69	25	2
		150	10	14	0.33	6.6	0.63	3.2	-0.69	32	2.1
Black Warrior River	b	50	3.7	4.8	0.28	2	0.53	0.98	-0.74	14	2.7
		100	6.2	8	0.29	3.3	0.53	1.6	-0.74	23	2.8
		150	8.5	11	0.3	4.8	0.57	2.2	-0.75	33	2.9
Black Warrior River	c	50	3.8	5	0.3	2.2	0.56	1	-0.74	14	2.8
		100	6.6	8.7	0.32	4	0.61	1.7	-0.74	25	2.8
		150	9.1	12	0.34	6	0.66	2.3	-0.75	35	2.9
Black Warrior River	d	50	4.3	5.5	0.27	2.4	0.55	1.2	-0.72	15	2.4
		100	6.1	7.9	0.28	3.4	0.56	1.7	-0.73	22	2.6
		150	7.7	10	0.29	4.4	0.56	2.1	-0.73	28	2.6
Frio	a	50	9.2	12	0.27	5.2	0.56	2.3	-0.75	35	2.8
		100	15	20	0.28	9.2	0.6	3.7	-0.76	61	3
		150	21	28	0.28	13	0.62	5	-0.77	87	3
Frio	b	50	5.9	7.5	0.28	3.3	0.57	1.5	-0.75	23	2.8
		100	9.9	13	0.29	6	0.6	2.4	-0.76	40	3
		150	14	18	0.3	8.6	0.62	3.3	-0.76	56	3.1
Frio	c	50	5.5	6.9	0.25	2.9	0.52	1.4	-0.74	21	2.8
		100	8.8	12	0.31	5.2	0.59	2.3	-0.75	34	2.9
		150	12	16	0.32	7.3	0.61	3	-0.75	47	2.9
Madison	a	50	21	28	0.31	12	0.57	6	-0.72	74	2.5
		100	36	47	0.32	21	0.58	9.9	-0.72	120	2.4
		150	48	63	0.32	28	0.59	13	-0.72	160	2.4
Madison	b	50	13	14	0.065	6.5	0.48	3.9	-0.71	44	2.3
		100	21	22	0.077	9.9	0.48	6.1	-0.71	67	2.2
		150	27	29	0.086	12	0.46	7.9	-0.71	86	2.2
Navajo-Nugget	a	50	25	34	0.34	16	0.63	7.1	-0.72	90	2.5
		100	43	58	0.34	28	0.64	12	-0.72	150	2.6
		150	59	80	0.35	38	0.64	16	-0.73	210	2.6
Navajo-Nugget	b	50	18	23	0.27	9.1	0.49	5.2	-0.72	64	2.4
		100	31	39	0.27	15	0.49	8.8	-0.72	100	2.4
		150	41	53	0.27	21	0.5	12	-0.71	140	2.4
Morrison		50	12	16	0.33	7.3	0.6	3.4	-0.72	42	2.5
		100	20	27	0.33	12	0.6	5.7	-0.72	70	2.5
		150	27	36	0.33	16	0.61	7.6	-0.72	94	2.5
Potomac		50	9.5	12	0.29	5.2	0.55	2.9	-0.7	29	2.1
		100	13	18	0.33	8.8	0.65	4	-0.71	44	2.2
		150	17	24	0.37	13	0.75	4.9	-0.71	58	2.3
Fox Hills		50	5.8	7.8	0.34	3.8	0.65	1.6	-0.72	21	2.6
		100	9.7	13	0.35	6.6	0.68	2.7	-0.73	36	2.7
		150	13	18	0.36	9.4	0.71	3.6	-0.73	50	2.8
Paluxy		50	2.9	3.8	0.33	1.8	0.62	0.7	-0.76	11	2.9
		100	5	6.7	0.33	3.2	0.62	1.2	-0.75	20	2.9
		150	7	9.3	0.33	4.4	0.63	1.7	-0.75	27	2.9
St. Peter		50	2.5	3.4	0.35	1.6	0.64	0.7	-0.72	8.6	2.5
		100	4.5	6.2	0.35	3	0.65	1.3	-0.72	16	2.5
		150	6.5	8.8	0.36	4.2	0.65	1.8	-0.72	22	2.5
Cedar Keys		50	3.4	4.5	0.33	2.1	0.61	0.84	-0.75	14	3
		100	5.8	7.7	0.34	3.6	0.62	1.4	-0.76	23	3
		150	7.9	11	0.34	5	0.63	1.9	-0.76	32	3.1

4.4 Synopsis of aquifer data and storage capacities

Table 29: General ranges in the input parameters for both the pressure model and the trapping model parameters, see Tables 26 & 25.

Parameter	Symbol	Value	Data Source	Reference
Residual CO ₂ saturation	S_{rg}	0.2 – 0.4	experiments	Bennion and Bachu [2008]; Oak et al.
Connate water saturation	S_{wc}	0.3 – 0.5	experiments	Bennion and Bachu [2008]; Oak et al.
Endpoint relative permeability to CO ₂	k_{rg}^*	0.5 – 0.7	experiments	Bennion and Bachu [2008]; Oak et al.
Coefficient of CO ₂ -saturated-brine flux	α	0.01	estimated	Kneafsey and Pruess [2010a]; Riaz et al.
Compressibility (GPa ⁻¹)	c	4e-11 – 3e-10 ^a	experiments	[Wang, 2000, Table C1]
Undrained Poisson ratio	ν	0.28 – 0.33	experiments	[Wang, 2000, Table C1]
Geothermal gradient (°C/km)	G_T	15 – 40	nationwide data	Kron and Heiken [1980]; Nathenson et al.
Surface temperature (°C)	T_s	0 – 21	nationwide data	USs [2010]
Depth to top of aquifer (m)	D	800 – 3000 ^b	nationwide data	see text
Depth from aquifer to bedrock (m)	B	0 – 13,000	nationwide data	Frezon et al. [1983]
Net aquifer thickness (m)	H	≤ 500	nationwide data	see text
Length of trapping-model domain (km)	L_T	50 – 500	aquifer data	Frezon et al. [1988]
Length of pressure-model domain (km)	L_{pres}	50 – 500	nationwide data	Frezon et al. [1988]
Width of well array (km)	W	50 – 500	nationwide data	Frezon et al. [1988]
Porosity	ϕ	0 – 0.3	nationwide data	Freeze and Cherry [1979]
Caprock slope (degrees)	ϑ	0 – 2	nationwide data	see text
Darcy velocity (cm/yr)	U	0 – 10	nationwide data	[Bjørlykke, 1993, p.145]
Aquifer permeability (mD)	k_{aq}	10 – 1000	nationwide data	Ortoleva [1994]; Freeze and Cherry [1979]
Mean vertical permeability (mD)	k_{cap}	1e-8 – 1	experiments	Neuzil [1994]; Tokunaga et al. [1999]
Salinity (g/L)	s	0 – 450 ^c	nationwide data	Hovorka et al. [2003c]
CO ₂ solubility (volume fraction)	χ_v	0.01 – 0.14	$f(T, P, s)$	Duan and Sun [2003]
Brine density (kg/m ³)	ρ_w	959 – 1130	$f(T, P, s)$	Batzle and Wang [1992]
CO ₂ density (kg/m ³)	ρ_g	200 – 800	$f(T, P)$	Carbon Capture and Sequestration [2004]
CO ₂ -saturated-brine density (kg/m ³)	ρ_s	969 – 1133	$f(T, P, s, \chi_v)$	Garcia [2001]
Brine viscosity (mPa s)	μ_w	0.2 – 1.2	$f(T, P, s)$	Batzle and Wang [1992]
CO ₂ viscosity (mPa s)	μ_g	0.03 – 0.07	$f(T, P)$	Carbon Capture and Sequestration [2004]
Fracture pressure (MPa)	P_{frac}	10 – 70	$f(\rho_o, \rho_w, D, \phi)$	Eq. 15,14; Zoback and Zoback [1990]

^a Range for sandstones. The compressibility of limestone and mudstone are within this range (limestone, $c \approx 6e - 11$; mudstone, $c \approx 1e - 11$).

^b 800 m is the depth at which CO₂ changes from a gas to a supercritical fluid, assuming a hydrostatic pressure gradient of 25° C/km. 3000 m is the depth below which the density of CO₂ nearly stops increasing, also assuming a hydrostatic pressure gradient of 25° C/km. Since the storage efficiency stops increasing below 3000 m, the higher cost of drilling at greater depths Bachu [2003a].

^c Since we only found CO₂ solubility data for $0 \leq s \leq 200$ g/L ($0 \leq s \leq 4$ m), all parameters that are based on s are calculated at $s = 200$ g/L.

Table 30: Storage capacities for every aquifer we study at different injection times, T . Capacities written in bold are pressure limited; otherwise, they are migration limited.

Reservoir	Region	Storage capacity (Gt CO ₂) at different injection times, T (years)										
		$T = 25$	50	75	100	150	200	250	300	400	500	600
Mt. Simon	a	$9.4^{+7.9}_{-2.4}$	$15^{+12}_{-3.7}$	$19^{+16}_{-4.8}$	$23^{+20}_{-5.9}$	$31^{+26}_{-7.8}$	$37^{+32}_{-9.5}$	44^{+37}_{-11}	50^{+42}_{-13}	61^{+52}_{-16}	73^{+43}_{-18}	84^{+32}_{-23}
Mt. Simon	b	$4.8^{+4.4}_{-1.3}$	$7.5^{+5.8}_{-2}$	$9.8^{+3.6}_{-3}$	$10^{+3.3}_{-3.3}$	$10^{+3.3}_{-3.3}$	$10^{+3.3}_{-3.3}$	$10^{+3.3}_{-3.3}$	$10^{+3.3}_{-3.3}$	$10^{+3.3}_{-3.3}$	$10^{+3.3}_{-3.3}$	$10^{+3.3}_{-3.3}$
Mt. Simon	c	$2.7^{+2.5}_{-0.72}$	$4.5^{+4.1}_{-1.2}$	$6.1^{+5.6}_{-1.6}$	7.7^{+7}_{-2}	$11^{+9.7}_{-2.8}$	$13^{+8.6}_{-3.6}$	$16^{+5.9}_{-4.3}$	$17^{+5.2}_{-4.3}$	$17^{+5.2}_{-4.3}$	$17^{+5.2}_{-4.3}$	$17^{+5.2}_{-4.3}$
Black Warrior River	a	$3.8^{+3.2}_{-1}$	$5.6^{+4.6}_{-1.5}$	$7^{+5.8}_{-1.9}$	$8.2^{+6.8}_{-2.2}$	$10^{+8.6}_{-2.7}$	$12^{+10}_{-3.3}$	$14^{+12}_{-3.8}$	$16^{+13}_{-4.3}$	$20^{+17}_{-5.3}$	$24^{+19}_{-6.3}$	$28^{+15}_{-9.2}$
Black Warrior River	b	$2.3^{+1.9}_{-0.58}$	$3.7^{+3.1}_{-0.93}$	$5.0^{+4.1}_{-1.3}$	$6.2^{+5.1}_{-1.6}$	$8.6^{+7}_{-2.1}$	$11^{+9}_{-2.7}$	$13^{+11}_{-3.3}$	$16^{+13}_{-3.9}$	20^{+17}_{-5}	$25^{+12}_{-6.2}$	$29^{+7.3}_{-7.3}$
Black Warrior River	c	$2.3^{+2.1}_{-0.65}$	$3.8^{+3.5}_{-1.1}$	$5.2^{+4.8}_{-1.5}$	$6.5^{+6}_{-1.8}$	$8.9^{+8.1}_{-2.5}$	$11^{+5.7}_{-3.2}$	$14^{+3.4}_{-3.8}$	$14^{+3.4}_{-3.4}$	$14^{+3.4}_{-3.4}$	$14^{+3.4}_{-3.4}$	$14^{+3.4}_{-3.4}$
Black Warrior River	d	$3.2^{+2.7}_{-0.87}$	$4.3^{+3.6}_{-1.2}$	$5.3^{+4.4}_{-1.5}$	$6.1^{+5.1}_{-1.7}$	$7.7^{+6.4}_{-2.1}$	$9.1^{+7.6}_{-2.5}$	$10^{+8.7}_{-2.9}$	$12^{+8.7}_{-3.2}$	$14^{+12}_{-3.9}$	$17^{+14}_{-4.6}$	$19^{+16}_{-5.2}$
Frio	a	$5.9^{+5.2}_{-1.9}$	$9.2^{+8.1}_{-3}$	12^{+11}_{-4}	$15^{+11}_{-5.3}$	$18^{+8.2}_{-8.1}$	$18^{+8.2}_{-8.1}$	$18^{+8.2}_{-8.1}$	$18^{+8.2}_{-8.1}$	$18^{+8.2}_{-8.1}$	$18^{+8.2}_{-8.1}$	$18^{+8.2}_{-8.1}$
Frio	b	$3.7^{+3.3}_{-1.1}$	$5.9^{+5.3}_{-2.2}$	$8^{+4.3}_{-4.3}$	$8.6^{+3.7}_{-4.9}$	$8.6^{+3.7}_{-4.9}$	$8.6^{+3.7}_{-4.9}$	$8.6^{+3.7}_{-4.9}$	$8.6^{+3.7}_{-4.9}$	$8.6^{+3.7}_{-4.9}$	$8.6^{+3.7}_{-4.9}$	$8.6^{+3.7}_{-4.9}$
Frio	c	$3.6^{+3.2}_{-1}$	$5.5^{+5}_{-1.6}$	$7.3^{+6.6}_{-2}$	$8.9^{+8}_{-2.5}$	$12^{+5.7}_{-5}$	$12^{+5.4}_{-5.4}$	$12^{+5.4}_{-5.4}$	$12^{+5.4}_{-5.4}$	$12^{+5.4}_{-5.4}$	$12^{+5.4}_{-5.4}$	$12^{+5.4}_{-5.4}$
Madison	a	$5.3^{+2.2}_{-2}$	$5.3^{+2.2}_{-2}$	$5.3^{+2.2}_{-2}$	$5.3^{+2.2}_{-2}$	$5.3^{+2.2}_{-2}$	$5.3^{+2.2}_{-2}$	$5.3^{+2.2}_{-2}$	$5.3^{+2.2}_{-2}$	$5.3^{+2.2}_{-2}$	$5.3^{+2.2}_{-2}$	$5.3^{+2.2}_{-2}$
Madison	b	$6.6^{+2.6}_{-2.8}$	$6.6^{+2.6}_{-2.8}$	$6.6^{+2.6}_{-2.8}$	$6.6^{+2.6}_{-2.8}$	$6.6^{+2.6}_{-2.8}$	$6.6^{+2.6}_{-2.8}$	$6.6^{+2.6}_{-2.8}$	$6.6^{+2.6}_{-2.8}$	$6.6^{+2.6}_{-2.8}$	$6.6^{+2.6}_{-2.8}$	$6.6^{+2.6}_{-2.8}$
Navajo-Nugget	a	$5.1^{+2.4}_{-2.4}$	$5.1^{+2.4}_{-2.4}$	$5.1^{+2.4}_{-2.4}$	$5.1^{+2.4}_{-2.4}$	$5.1^{+2.4}_{-2.4}$	$5.1^{+2.4}_{-2.4}$	$5.1^{+2.4}_{-2.4}$	$5.1^{+2.4}_{-2.4}$	$5.1^{+2.4}_{-2.4}$	$5.1^{+2.4}_{-2.4}$	$5.1^{+2.4}_{-2.4}$
Navajo-Nugget	b	$4.0^{+1.4}_{-1.4}$	$4.0^{+1.4}_{-1.4}$	$4.0^{+1.4}_{-1.4}$	$4.0^{+1.4}_{-1.4}$	$4.0^{+1.4}_{-1.4}$	$4.0^{+1.4}_{-1.4}$	$4.0^{+1.4}_{-1.4}$	$4.0^{+1.4}_{-1.4}$	$4.0^{+1.4}_{-1.4}$	$4.0^{+1.4}_{-1.4}$	$4.0^{+1.4}_{-1.4}$
Morrison		$7.0^{+6.5}_{-1.9}$	$12^{+11}_{-3.3}$	$16^{+6.8}_{-4.4}$	$17^{+5.3}_{-5.3}$	$17^{+5.3}_{-5.3}$	$17^{+5.3}_{-5.3}$	$17^{+5.3}_{-5.3}$	$17^{+5.3}_{-5.3}$	$17^{+5.3}_{-5.3}$	$17^{+5.3}_{-5.3}$	$17^{+5.3}_{-5.3}$
Potomac		$3.6^{+1.5}_{-1.5}$	$3.6^{+1.5}_{-1.5}$	$3.6^{+1.5}_{-1.5}$	$3.6^{+1.5}_{-1.5}$	$3.6^{+1.5}_{-1.5}$	$3.6^{+1.5}_{-1.5}$	$3.6^{+1.5}_{-1.5}$	$3.6^{+1.5}_{-1.5}$	$3.6^{+1.5}_{-1.5}$	$3.6^{+1.5}_{-1.5}$	$3.6^{+1.5}_{-1.5}$
Fox Hills		$3.0^{+3.1}_{-0.98}$	$4.7^{+3.1}_{-1.5}$	$5.5^{+2.3}_{-2.3}$	$5.5^{+2.3}_{-2.3}$	$5.5^{+2.3}_{-2.3}$	$5.5^{+2.3}_{-2.3}$	$5.5^{+2.3}_{-2.3}$	$5.5^{+2.3}_{-2.3}$	$5.5^{+2.3}_{-2.3}$	$5.5^{+2.3}_{-2.3}$	$5.5^{+2.3}_{-2.3}$
Paluxy		$1.5^{+0.5}_{-0.5}$	$1.5^{+0.5}_{-0.5}$	$1.5^{+0.5}_{-0.5}$	$1.5^{+0.5}_{-0.5}$	$1.5^{+0.5}_{-0.5}$	$1.5^{+0.5}_{-0.5}$	$1.5^{+0.5}_{-0.5}$	$1.5^{+0.5}_{-0.5}$	$1.5^{+0.5}_{-0.5}$	$1.5^{+0.5}_{-0.5}$	$1.5^{+0.5}_{-0.5}$
St. Peter		$1.4^{+0.55}_{-0.41}$	$1.6^{+0.38}_{-0.38}$	$1.6^{+0.38}_{-0.38}$	$1.6^{+0.38}_{-0.38}$	$1.6^{+0.38}_{-0.38}$	$1.6^{+0.38}_{-0.38}$	$1.6^{+0.38}_{-0.38}$	$1.6^{+0.38}_{-0.38}$	$1.6^{+0.38}_{-0.38}$	$1.6^{+0.38}_{-0.38}$	$1.6^{+0.38}_{-0.38}$
Cedar Keys		$2.1^{+2}_{-0.58}$	$3.4^{+3.3}_{-0.97}$	$4.7^{+4.5}_{-1.3}$	$5.8^{+5.6}_{-1.6}$	$8^{+7.7}_{-2.3}$	$9.9^{+9.5}_{-2.8}$	$12^{+11}_{-3.3}$	$14^{+13}_{-3.9}$	$17^{+17}_{-4.9}$	$21^{+20}_{-5.8}$	$24^{+23}_{-6.8}$

5 Technology transfer activities

5.1 Peer-reviewed journal publications

1. R. Juanes, C. W. MacMinn, and M. L. Szulczewski. The footprint of the CO₂ plume during carbon dioxide storage in saline aquifers: storage efficiency for capillary trapping at the basin scale. *Transport in Porous Media*, **82**(1):19–30 (2010), doi:10.1007/s11242-009-9420-3.
2. C. W. MacMinn and M. L. Szulczewski and R. Juanes. CO₂ migration in saline aquifers. Part 1: Capillary trapping under slope and groundwater flow. *Journal of Fluid Mechanics*, **662**:329–351 (2010), doi:10.1017/S0022112010003319.
3. C. W. MacMinn and M. L. Szulczewski and R. Juanes. CO₂ migration in saline aquifers. Part 2: Capillary and solubility trapping. *Journal of Fluid Mechanics*, **668**:321–351 (2011), doi:10.1017/jfm.2011.379.
4. M. L. Szulczewski, C. W. MacMinn, H. J. Herzog and R. Juanes. Lifetime of carbon capture and storage as a climate-change mitigation technology. *Proceedings of the National Academy of Sciences of the U.S.A.*, **109**(14):5185–5189 (2012), doi:10.1073/pnas.1115347109 (cover story).
5. B. Zhao, C. W. MacMinn, M. L. Szulczewski, J. A. Neufeld, H. E. Huppert, and R. Juanes. Interface pinning of immiscible gravity-exchange flows in porous media. *Physical Review E*, **87**, 023015 (2013), doi:10.1103/PhysRevE.87.023015.
6. M. L. Szulczewski and R. Juanes. The evolution of miscible gravity currents in horizontal porous layers. *Journal of Fluid Mechanics*, **719**, 82-96 (2013), doi:10.1017/jfm.2012.631.
7. C. W. MacMinn and R. Juanes. Buoyant currents arrested by convective dissolution. *Geophysical Research Letters*, **40**(10), 2017–2022 (2013), doi:10.1002/grl.50473.
8. X. Fu, L. Cueto-Felgueroso, and R. Juanes. Pattern formation and coarsening dynamics in three-dimensional convective mixing in porous media. *Philosophical Transactions of the Royal Society A*, **371**, 20120355 (2013), doi:10.1098/rsta.2012.0355.
9. M. L. Szulczewski, M. A. Hesse, and R. Juanes. Carbon dioxide dissolution in structural and stratigraphic traps. *Journal of Fluid Mechanics*, **736**, 287-315 (2013), doi:10.1017/jfm.2013. (Journal cover; Selected for Focus on Fluids).
10. J. J. Hidalgo, C. W. MacMinn and R. Juanes. Dynamics of convective dissolution from a migrating current of carbon dioxide. *Advances in Water Resources*, **62**, 511-519 (2013), doi:10.1016/j.advwatres.2013.06.013.
11. M. L. Szulczewski, C. W. MacMinn and R. Juanes. How pressure buildup and CO₂ migration both constrain storage capacity in deep saline aquifers. Submitted for publication.

5.2 Conference contributions

1. PI Juanes presented paper on the model of plume migration under capillary trapping at the Computational Methods in Water Resources Conference in Barcelona, June 21-24, 2010 [Szulczewski et al., 2010a]. He also organized and chaired a session dedicated to CO₂ sequestration (<http://congress.cimne.com/CMWR2010/frontal/Topics.asp>).
2. Students Christopher MacMinn and Michael Szulczewski gave one oral presentation and presented one poster at the International Conference on Greenhouse Gas Technologies (GHGT-10), which took place in Amsterdam, September 19-23, 2010.
3. PI Juanes and student Christopher MacMinn each gave oral presentations in the session on “Porous Media I: CO₂ Sequestration” at the 63rd Annual Meeting of the APS Division of Fluid Dynamics (Long Beach, November 21-23, 2010).
4. PI Juanes and student Christopher MacMinn each gave oral presentations in the session on “Geologic CO₂ Sequestration: Capillary and Solubility Trapping of Supercritical CO₂” at the Fall Meeting of the American Geophysical Union (San Francisco, December 13–17, 2010). Graduate student Michael Szulczewski presented a poster.
5. Students Christopher MacMinn and Michael Szulczewski gave one oral presentation and presented one poster at the International Conference on Greenhouse Gas Technologies (GHGT-10), which took place in Amsterdam, September 19-23, 2010.
6. PI Juanes gave an invited presentation at the SPE Advanced Technology Workshop on “Carbon Capture, Utilization and Storage (CCUS): Environment, Energy Security and Opportunities for the Middle East” (Abu Dhabi, March 7-9, 2011).
7. Several presentations were given at the Computational Methods in Water Resources Conference (Urbana-Champaign, Illinois, June 17-21, 2012):
 - (a) Christopher W. MacMinn and Ruben Juanes. Gravity currents arrested by convective mixing.
 - (b) Michael L. Szulczewski and Ruben Juanes. Convective mixing and late times: simulations and experiments.
 - (c) Xiaojing Fu, Luis Cueto-Felgueroso, and Ruben Juanes. Three-dimensional high-resolution simulation of convective mixing.
 - (d) Benzong Zhao, Christopher W. MacMinn, Michael L. Szulczewski, Jerome A. Neufeld, Herbert E. Huppert, and Ruben Juanes. Capillary pinning of CO₂ gravity currents.
 - (e) Juan J. Hidalgo, Luis Cueto-Felgueroso, and Ruben Juanes. Effect of heterogeneity on the miscible displacement of fluids.
8. PI Juanes was the organizer of a minisymposium on CO₂ sequestration at the same conference.

9. Several oral presentations were given at the American Physical Society Division of Fluid Dynamics Meeting (San Diego, November 2012):
 - (a) M. Szulczewski, R. Juanes. Nonlinear Taylor dispersion in gravity currents in porous media.
 - (b) Juan J. Hidalgo, Luis Cueto-Felgueroso, Jaime Fe, Ruben Juanes. Scaling of convective mixing in CO₂ sequestration.
 - (c) Xiaojing Fu, Luis Cueto-Felgueroso, Ruben Juanes. Coarsening dynamics of 3D convective dissolution in porous media.
 - (d) Benzhong Zhao, Christopher MacMinn, Michael Szulczewski, Herbert E. Huppert, Ruben Juanes. Capillary Pinning of Immiscible Gravity Currents in Porous Media.
10. Several oral and poster presentations were given at the American Geophysical Union Fall Meeting (San Francisco, December 2012):
 - (a) Ruben Juanes, Michael Szulczewski, Christopher MacMinn, Howard Herzog. The Lifetime of Carbon Capture and Storage as a Climate-change Mitigation Technology: How both Pressure and Migration Constrain CO₂ Storage Capacity. (Oral presentation).
 - (b) Birendra Jha, Bradford H. Hager, Ruben Juanes. Coupled Modeling of Fault Poromechanics During Geologic CO₂ Storage.
 - (c) Benzhong Zhao, Christopher MacMinn, Michael Szulczewski, Herbert E. Huppert, Ruben Juanes. Capillary Pinning of Immiscible Gravity Currents in Porous Media. (Oral presentation).
 - (d) Juan J. Hidalgo, Luis Cueto-Felgueroso, Jaime Fe, Ruben Juanes. Scaling of Convective Mixing in CO₂ sequestration. (Oral presentation).
 - (e) Michael Szulczewski, Marc A. Hesse, Ruben Juanes. The role of gravity fingering in mitigating CO₂ leakage during storage in anticlines.
 - (f) Xiaojing Fu, Luis Cueto-Felgueroso, Ruben Juanes. Self-organized patterns of 3D convective dissolution in porous media. (Oral presentation).
11. PI Juanes gave an invited lecture titled Lifetime of carbon capture and storage as a climate-change mitigation technology at the SIAM Geosciences Conference (Padova, Italy, June 2013).

5.3 Talks, seminars and presentations

1. PI Juanes was speaker and panelist at the Carbon Capture and Sequestration Research Panel, MIT, December 2009 (<http://events.mit.edu/event.html?id=11598986&date=2009/12/0>)
2. PI Juanes was keynote speaker and panelist in the “Grand Challenges” session of the Institute of Biological Engineering Annual Meeting (Cambridge, MA, 2010).

3. Student presentations by Christopher MacMinn and Michael Szulczewski at the Gordon Research Seminar on Carbon Capture and Storage, and the associated Gordon Research Conference on Flow and Transport in Permeable Media (July 2010).
4. PI Juanes gave an invited talk title “Geologic Capacity Constraints on the Adoption of Carbon Capture and Storage in the United States” at the MIT Carbon Sequestration Forum XI (November 3-4, 2010).
5. PI Juanes gave a lecture titled “Mitigating Climate Change by Putting the Carbon Back in the Ground” for the Civil and Environmental Engineering Student Association at MIT (December 1, 2010).
6. PI Juanes gave an invited presentation at the Computational Sustainability Seminar Series (MIT, October 13, 2011).
7. PI Juanes participated and presented his work in the DOE Geoscience symposium (Gaithersburg, April 2012), where he received the DOE Award for Outstanding Contributions in Geosciences Research.
8. PI Juanes gave a presentation to the president of Iceland during his visit to MIT (May 2012).
9. PI Juanes was invited speaker at the Chevron Climate Energy and Environment Webinar Series, San Ramon, CA (July 2012).
10. PI Juanes was invited speaker at the USGS/DOE Workshop on “Geologic CO₂ Sequestration: Re-evaluating Storage Efficiency Estimates”, Austin, TX (July 2012).
11. PI Juanes was speaker and session co-chair of the “Subsurface Science and Technology” session at the The MIT-Stanford Energy Game Changers Conference II, Cambridge, MA (July 2012).
12. PI Juanes gave a laboratory-wide colloquium at Fermilab, titled “The lifetime of carbon capture and storage as a climate change mitigation technology” (January 2013).
13. PI Juanes participated as chair of a session on CCS and induced seismicity at the MIT Carbon Sequestration Forum (April 2013).
14. PI Juanes attended and gave a presentation at the DOE/NETL Project Review Meeting in Pittsburgh (August 2013).

5.4 Educational activities and outreach

1. Student presentations at the Cambridge Science Festival, by Christopher MacMinn and Michael Szulczewski (November 2009).
2. PI Juanes was the instructor of the semester-long graduate course “Computational Methods for Flow in Porous Media,” which featured solution techniques for several problems in the area of CO₂ sequestration.

- 07/2012 PI Juanes was the director and lead instructor of the 3-day short course “Carbon Capture and Storage: Science, Technology and Policy”, given through the MIT Professional Institute (July of 2010, 2011, 2012)
(http://web.mit.edu/professional/short-programs/courses/geological_carbon_sequestration.htm)
3. Graduate students Christopher MacMinn and Robin Zhao, and undergraduate student Di Jing, presented a poster at the Undergraduate Research Opportunity Program (UROP) Expo, which took place at MIT on January 20, 2011.
 4. Graduate students Christopher MacMinn and Robin Zhao presented a poster titled “Fluid mechanics of geological carbon dioxide storage” at the MIT Energy Night (MIT Museum, Cambridge, Oct 21, 2011): http://energynight.mit.edu/MIT_Engry_Night/Presenters.html.
 5. PI Juanes gave a lecture on Carbon Capture and Storage as a climate-change mitigation technology for MIT freshmen. Graduate students Benzhong Zhao and Michael Szulczewski led a lab on the topic, where they illustrated the effect of convective dissolution on the migration of a buoyant current, using analogue fluids.
 6. PI Juanes taught the short course Carbon Capture and Storage: Science, Technology and Policy for the Alberta Department of Energy (Edmonton, AL, Canada, July 2013).

5.5 Scientific collaborations

1. The Juanes group has now an established collaboration with Prof. Herbert Huppert and Dr. Jerome Neufeld, from Cambridge University (U.K.). Graduate student Christopher MacMinn has received the Crighton Fellowship and is currently spending two months with Prof. Huppert’s group in Cambridge.
2. A PhD student from the Energy, Technology and Environment Research Center in Spain (CIEMAT), Iciar Barrios, is visiting our group for three months, to learn and apply our capacity estimation tools.

5.6 Editor/reviewer tasks

1. PI Juanes was reviewer and panelist for the LDRD Program of the Los Alamos National Laboratory, occasion in which he also visited the experimental facilities of Robert Ecke and Scott Backhaus at LANL.
2. R. Juanes and H. Class. Editorial: Special issue on computational methods in geologic CO₂ sequestration. *Advances in Water Resources*, **62**, 353-355 (2013), doi:10.1016/j.advwatres.2013.1

References

- Salinity of the Mt. Simon Sandstone in the Illinois Basin. Technical report, Midwest Geological Sequestration Consortium, 2005.
- Mean daily average temperature map of the United States. <http://cdo.ncdc.noaa.gov/cgi-bin/climaps/climaps.pl>, 2010.
- P. L. Applin and E. R. Appin. Regional subsurface stratigraphy and structure of Florida and southern Georgia. *A.A.P.G. Bulletin*, 28(12):1673–1753, 1944.
- P. L. Applin and E. R. Applin. The Gulf Series in northern Florida and southern Georgia. Professional Paper 524-G, U.S.G.S., 1967.
- W. R. Aucott. Hydrology of the southeastern Coastal Plain aquifer system in South Carolina and parts of Georgia and North Carolina. Professional Paper 1410-E, U.S.G.S., 1996.
- S. Bachu. Screening and ranking of sedimentary basins for sequestration of CO₂ in geological media in response to climate change. *Environ. Geol.*, 44:277–289, 2003a.
- S. Bachu. Screening and ranking of sedimentary basins for sequestration of CO₂ in geological media in response to climate change. *Environ. Geol.*, 44:277–289, 2003b.
- S. Bachu and J. J. Adams. Sequestration of CO₂ in geological media in response to climate change: capacity of deep saline aquifers to sequester CO₂ in solution. *Energ. Convers. Manage.*, 44:3151 – 3175, 2003.
- S. Bachu, D. Bonijoly, J. Bradshaw, R. Burruss, S. Holloway, N. P. Christensen, and O. M. Mathiassen. CO₂ storage capacity estimation: methodology and gaps. *Int. J. Greenh. Gas Control*, 1:430–443, 2007.
- R. A. Barker and M. Pernik. Regional hydrology and simulation of deep ground-water flow in the Southeastern Coastal Plain aquifer system in Mississippi, Alabama, Georgia, and South Carolina. Professional Paper 1410-C, U.S.G.S., 1994.
- D. A. Barnes, D. H. Bacon, and S. R. Kelley. Geological sequestration of carbon dioxide in the Cambrian Mount Simon Sandstone: regional storage capacity, site characterization, and large-scale injection feasibility, Michigan Basin. *Env. Geosci.*, 16(3):163–183, 2009.
- M. Batzle and Z. Wang. Seismic properties of pore fluids. *Geophysics*, 57:1396–1408, 1992.
- J. Bear. *Dynamics of Fluids in Porous Media*. Elsevier, New York, 1972.
- D. B. Bennion and S. Bachu. Drainage and imbibition relative permeability relationships for supercritical CO₂/brine and H₂S/brine systems in intergranular sandstone, carbonate, shale, and anhydrite rocks. *Soc. Pet. Eng. J.*, 11(3):487–496, 2008.
- K. Bjørlykke. Fluid flow in sedimentary basins. *Sedimentary Geology*, 86:137–158, 1993.

- Carbon Capture and Sequestration Technologies at MIT. CO₂ thermophysical property calculator. <http://sequestration.mit.edu/tools/index.html>.
- H. D. Cheng. *Multilayered aquifer systems: fundamentals and applications*. Marcel Dekker, 2000.
- L. C. Craig et al. Stratigraphy of the Morrison and related formations, Colorado Plateau Region. Bulletin 1009-E, U.S.G.S., 1955.
- J. Croisé, L. Schlickenrieder, P. Marschall, J. Y. Boisson, P. Vogel, and S. Yamamoto. Hydrogeological investigations in a low permeability claystone formation: the Mont Terri Rock Laboratory. *Phys. Chem. Earth*, 29:3–15, 2004.
- W. L. Dam, J. M. Kernodle, G. W. Levings, and S. D. Craigg. Hydrogeology of the Morrison Formation in the San Juan structural basin, New Mexico, Colorado, Arizona, and Utah. Hydrologic Investigations Atlas HA-720-J, U.S.G.S., 1990.
- D. N. Dewhurst, Y. Yang, and A. C. Aplin. Permeability and fluid flow in natural mudstones. In A. C. Aplin, A. J. Fleet, and J. H. S. Macquaker, editors, *Muds and Mudstones: Physical and Fluid-flow Properties*, volume 158, pages 23–43. Geological Society of London, 1999.
- J. S. Downey. Geohydrology of the Madison and associated aquifers in parts of Montana, North Dakota, South Dakota, and Wyoming. Professional Paper 1273-G, U.S.G.S., 1984.
- J. S. Downey and G. A. Dinwiddie. The regional aquifer system underlying the Northern Great Plains in parts of Montana, North Dakota, South Dakota, and Wyoming—summary. Professional Paper 1402-A, U.S.G.S., 1988.
- Z. Duan and R. Sun. An improved model calculating CO₂ solubility in pure water and aqueous NaCl solutions from 273 to 533 K and from 0 to 2000 bar. *Chem. Geol.*, 193: 257–271, 2003.
- C. Ehlig-Economides and M. J. Economides. Sequestering carbon dioxide in a closed underground volume. *J. Pet. Sci. Eng.*, 70:118–125, 2010.
- R. M. Enick and S. M. Scott. CO₂ solubility in water and brine under reservoir conditions. *Chem. Eng. Commun.*, 90(1):23–33, 1990.
- J. Ennis-King and L. Paterson. Role of convective mixing in the long-term storage of carbon dioxide in deep saline formations. *Soc. Pet. Eng. J.*, 10(3):349–356, September 2005.
- S. Escoffier, F. Homand, A. Giraud, N. Hoteit, and K. Su. Under stress permeability determination of the Meuse/Haute-Marne mudstone. *Eng. Geol.*, 81:329–340, 2005.
- R. Q. Foote, L. M. Massingill, and R. H. Wells. Petroleum geology and the distribution of conventional crude oil, natural gas, and natural gas liquids, East Texas Basin. Open-File Report 88-450-K, U.S.G.S., 1988.

- G. W. Freethey and G. E. Cordy. Geohydrology of Mesozoic rocks in the Upper Colorado River Basin in Arizona, Colorado, New Mexico, Utah, and Wyoming, excluding the San Juan Basin. Professional Paper 1411-C, U.S.G.S., 1991.
- G. W. Freethey, B. A. Kimball, D. E. Wilberg, and J. W. Hood. General hydrogeology of the aquifers of Mesozoic age, Upper Colorado River Basin – excluding the San Juan Basin – Colorado, Utah, Wyoming, and Arizona. Hydrologic Atlas 698, U.S.G.S., 1988.
- R. A. Freeze and J. A. Cherry. *Groundwater*. Prentice Hall, 1979.
- S. E. Frezon, T. M. Finn, and J. H. Lister. Total thickness of sedimentary rocks in the conterminous United States, 1983.
- S. E. Frezon, T. M. Finn, and K. L. Lister. Map of sedimentary basins in the conterminous United States. <http://pubs.er.usgs.gov/usgspubs/om/om223>, 1988.
- W. E. Galloway, D. K. Hobday, and K. Magara. Frio Formation of Texas Gulf Coastal Plain: depositional systems, structural framework, and hydrocarbon distribution. *A.A.P.G. Bulletin*, 66(6):649–648, 1982.
- J. E. Garcia. Density of aqueous solutions of CO₂. Technical Report 49023, Lawrence Berkeley National Laboratory, 2001.
- G. Garven. Continental scale groundwater flow and geologic processes. *Annu. Rev. Earth Planet. Sci.*, 89:89–117, 1995.
- N. Gupta. *Geologic and fluid-density controls on the hydrodynamics of the Mt. Simon Sandstone and overlying geologic units in Ohio and surrounding states*. PhD thesis, The Ohio State University, 1993.
- Jr. H. Trapp. Hydrogeologic framework of the Northern Atlantic Coastal Plain in parts of North Carolina, Virginia, Maryland, Delaware, New Jersey, and New York. Professional Paper 1404-G, U.S.G.S., 1992.
- M. A. Hesse, H. A. Tchelepi, and F. M. Orr, Jr. Scaling analysis of the migration of CO₂ in saline aquifers. In *SPE Annual Technical Conference and Exhibition*, San Antonio, TX, September 24–27 2006. (SPE 102796).
- M. A. Hesse, F. M. Orr, Jr., and H. A. Tchelepi. Gravity currents with residual trapping. *J. Fluid Mech.*, 611:35–60, 2008.
- J. D. Hoholick, T. Metarko, and P. E. Potter. Regional variations of porosity and cement: St. Peter and Mt. Simon sandstones in Illinois Basin. *A.A.P.G. Bulletin*, 68(6):753–764, 1984.
- S. D. Hovorka. Optimal geological environments for carbon dioxide disposal in saline aquifers in the United States. Contract Report DE-AC26-98FT40417, Bureau of Economic Geology, The University of Texas at Austin, 1999.

- S. D. Hovorka, C. Doughty, P. R. Knox, C. T. Green, K. Pruess, and S. M. Benson. Evaluation of brine-bearing sands of the Frio Formation, Upper Texas Gulf Coast for geologic sequestration of CO₂. Technical report, Bureau of Economic Geology, 2001.
- S. D. Hovorka, M. L. Romero, A. G. Warne, W. A. Ambrose, T. A. Tremblay, R. H. Trevino, and D. Sasson. Brine-formation database. <http://www.beg.utexas.edu/environqlty/co2seq/dispalsalnt01.htm>, November 2003a.
- S. D. Hovorka, M. L. Romero, A. G. Warne, W. A. Ambrose, T. A. Tremblay, R. H. Trevino, and D. Sasson. Brine-formation database. <http://www.beg.utexas.edu/environqlty/co2seq/>, November 2003b.
- S. D. Hovorka, M. L. Romero, A. G. Warne, W. A. Ambrose, T. A. Tremblay, R. H. Trevino, and D. Sasson. Sequestration of greenhouse gases in brine formations. <http://www.beg.utexas.edu/environqlty/co2seq/dispalsalnt01.htm>, November 2003c.
- H. E. Huppert and A. W. Woods. Gravity-driven flows in porous media. *J. Fluid Mech.*, 292:55–69, 1995.
- IPCC. *Special Report on Carbon Dioxide Capture and Storage*, B. Metz et al. (eds.). Cambridge University Press, 2005.
- R. Juanes and C. W. MacMinn. Upscaling of capillary trapping under gravity override: Application to CO₂ sequestration in aquifers. In *SPE/DOE Symposium on Improved Oil Recovery*, Tulsa, OK, April 19–23, 2008. (SPE 113496).
- R. Juanes, E. J. Spiteri, F. M. Orr, Jr., and M. J. Blunt. Impact of relative permeability hysteresis on geological CO₂ storage. *Water Resour. Res.*, 42:W12418, 2006.
- R. Juanes, C. W. MacMinn, and M. L. Szulczewski. The footprint of the CO₂ plume during carbon dioxide storage in saline aquifers: storage efficiency for capillary trapping at the basin scale. *Transp. Porous Media*, 82:19–30, 2010.
- J. M. Kernodle. Hydrogeology and steady-state simulation of ground-water flow in the San Juan Basin New Mexico, Colorado, Arizona, and Utah. Water-Resources Investigation Report 95-4187, U.S.G.S., 1996.
- Y. K. Kharaka and J. S. Hanor. Deep fluids in the continents: I. Sedimentary basins. In J. I. Drever, editor, *Treatise on Geochemistry*, volume 5. Elsevier, 2007.
- P. B. King and H. M. Beikman. Geologic map of the United States. US Geological Survey, 1974.
- T. J. Kneafsey and K. Pruess. Laboratory flow experiments for visualizing carbon dioxide-induced, density-driven brine convection. *Transp. Porous Med.*, 82:123–139, 2010a.
- T. J. Kneafsey and K. Pruess. Laboratory flow experiments for visualizing carbon dioxide-induced, density-driven brine convection. *Transp. Porous Media*, 82:123–139, 2010b.

- D. R. Kolata. *Interior Cratonic Basins*, chapter 2, pages 59–73. A.A.P.G, 1990.
- L. F. Konikow and C. E. Neuzil. A method to estimate groundwater depletion from confining layers. *Water Resour. Res.*, 43:W07417, 2007.
- C. W. Kreitler, M. S. Akhter, and A. C. Donnelly. Hydrologic hydrochemical characterization of Texas Frio Formation used for deep-well injection of chemical wastes. *Environ. Geol. Water Sci.*, 16(2):107–120, 1990.
- A. Kron and G. Heiken. Geothermal gradient map of the United States. Technical report, Los Alamos National Lab, 1980.
- D. C. Lampe. Hydrogeologic framework of bedrock units and initial salinity distribution for a simulation of groundwater flow for the Lake Michigan Basin. Scientific Investigations Report 2009-5060, USGS, 2009.
- R. W. Lee. Water-quality maps for selected Upper Cretaceous water-bearing zones in the southeastern coastal plain. Water-Resources Investigations Report 85-4193, U.S.G.S., 1985.
- R. W. Lee. Geochemistry of ground water in the Southeastern Coastal Plain Aquifer System in Mississippi, Alabama, Georgia, and South Carolina. Professional Paper 1410-D, U.S.G.S., 1994.
- H. E. Leetaru and J. H. McBride. Reservoir uncertainty, Precambrian topography, and carbon sequestration in the Mt. Simon Sandstone, Illinois Basin. *Env. Geosci.*, 16(4): 235–243, 2009.
- R. J. LeVeque. *Numerical Methods for Conservation Laws*. Birkhäuser Verlag, Berlin, second edition, 1992.
- E. Lindeberg and D. Wessel-Berg. Vertical convection in an aquifer column under a gas cap of CO₂. *Energy Conv. Manag.*, 38:S229–S234, 1997.
- R. G. Loucks, M. M. Dodge, and W. E. Galloway. Regional controls on diagenesis and reservoir quality in lower Tertiary sandstones along the lower Texas Gulf Coast. In D. A. McDonald and R. C. Surdam, editors, *Clastic diagenesis*. A. A. P. G., 1984.
- C. W. MacMinn and R. Juanes. Post-injection spreading and trapping of CO₂ in saline aquifers: Impact of the plume shape at the end of injection. *Comput. Geosci.*, 13:483–491, 2009.
- C. W. MacMinn, M. L. Szulczewski, and R. Juanes. CO₂ migration in saline aquifers. Part 1: Capillary trapping under slope and groundwater flow. *J. Fluid Mech.*, 662:329–351, 2010.
- C. W. MacMinn, M. L. Szulczewski, and R. Juanes. CO₂ migration in saline aquifers. Part 2: Combined capillary and solubility trapping. *J. Fluid Mech.*, 688:321–351, 2011.

- R. J. Mandle and A. L. Kontis. Simulation of regional ground-water flow in the Cambrian-Ordovician aquifer system in the northern Midwest, United States. Professional Paper 1405-C, U.S.G.S., 1992.
- B. J. O. L. McPherson and B. S. Cole. Multiphase CO₂ flow, transport and sequestration in the Powder River Basin, Wyoming, USA. *Journal of Geochemical Exploration*, 69–70: 65–69, 2000.
- W. F. Meents, A. H. Bell, O. W. Rees, and W. G. Tilbury. Illinois oilfield brines: their geologic occurrence and chemical composition. Illinois Petroleum 66, Illinois Geological Survey, 1952.
- E. A. Merewether. Stratigraphy and tectonic implications of Upper Cretaceous rocks in the Powder River Basin, northeastern Wyoming and southeastern Montana. Bulletin 1917-T, U.S.G.S., 1996.
- J. A. Miller. The ground water atlas of the United States: Alabama, Florida, Georgia, South Carolina. Hydrologic Atlas 730-G, U.S.G.S., 1990.
- S. Mishra, J. F. Pickens, and J. Delay. New approaches for transient testing and long-term pressure monitoring of low-permeability caprocks. In *Proceedings of the International Symposium on Site Characterization for CO₂ Geological Storage*, 2006.
- R. A. Morton and L. S. Land. Regional variations in formation water chemistry, Frio Formation (Oligocene), Texas Gulf Coast. *A.A.P.G. Bulletin*, 71(2):191–206, 1987.
- M. Nathenson and M. Guffanti. Geothermal gradients in the conterminous united states. *J. Geophys. Res.*, 93:6437–6450, 1988.
- National Imagery and Mapping Agency. Digital terrain elevation data (DTED Level 0). <http://www.geocomm.com>.
- S. Neglia. Migration of fluids in sedimentary basins. *A.A.P.G. Bulletin*, 63(4):573–597, 1979.
- C. E. Neuzil. How permeable are clays and shales? *Water Resour. Res.*, 30(2):145–150, 1994.
- J.-P. Nicot. Evaluation of large-scale CO₂ storage on fresh-water sections of aquifers: An example from the Texas Gulf Coast Basin. *Int. J. Greenh. Gas Control*, 2(4):582–593, 2008.
- J. M. Nordbotten, M. A. Celia, and S. Bachu. Similarity solutions for fluid injection into confined aquifers. *J. Fluid Mech.*, 561:307–327, 2006.
- Jr. O. B. Lloyd and W. L. Lyke. The ground water atlas of the United States: Illinois, Indiana, Kentucky, Ohio, Tennessee. Hydrologic Atlas 730-K, U.S.G.S., 1995.
- M. J. Oak, L. E. Baker, and D. C. Thomas. Three-phase relative permeability of Berea sandstone. *J. Pet. Technol.*, 42(8):1054–1061, August 1990.

- P. Ortoleva, editor. *Basin Compartments and Seals*. A.A.P.G. Memoir 61. A.A.P.G., 1994.
- G. S. H. Pau, J. B. Bell, K. Pruess, A. S. Almgren, M. J. Lijewski, and K. Zhang. High-resolution simulation and characterization of density-driven flow in CO₂ storage in saline aquifers. *Adv. Water Resour.*, 33(4):443–455, 2010.
- R. A. Renken. Hydrology of the southeastern Coastal Plain aquifer system in Mississippi, Alabama, Georgia, and South Carolina. Professional Paper 1410-B, U.S.G.S., 1996.
- A. Riaz, M. Hesse, H. A. Tchelepi, and F. M. Orr, Jr. Onset of convection in a gravitationally unstable, diffusive boundary layer in porous media. *J. Fluid Mech.*, 548:87–111, 2006a.
- A. Riaz, M. Hesse, H. A. Tchelepi, and F. M. Orr, Jr. Onset of convection in a gravitationally unstable, diffusive boundary layer in porous media. *J. Fluid Mech.*, 548:87–111, 2006b.
- P. D. Ryder and A. F. Ardis. Hydrology of the Texas Gulf Coast aquifer systems. Open-File Report 91-64, U.S.G.S., 1991.
- L. Y. Sadler, M. B. Rahnama, and G. P. Whittle. Laboratory measurement of the permeability of Selma Chalk using an improved experimental technique. *Hazard. Waste Hazard. Mater.*, 9(4):331–343, 1992.
- E. W. Strom and M. J. Mallory. Hydrogeology and simulation of ground-water flow in the Eutaw-McShan Aquifer and in the Tuscaloosa Aquifer system in northeastern Mississippi. Water-Resources Investigation Report 94-4223, U.S.G.S., 1995.
- M. L. Szulczewski. Storage capacity and injection rate estimates for CO₂ sequestration in deep saline aquifers in the conterminous United States. Master’s thesis, Massachusetts Institute of Technology, 2009.
- M. L. Szulczewski and R. Juanes. A simple but rigorous model for calculating CO₂ storage capacity in deep saline aquifers at the basin scale. *Energy Procedia* (Proc. GHGT-9), 1(1):3307–3314, doi:10.1016/j.egyproc.2009.02.117, 2009.
- M. L. Szulczewski, C. W. MacMinn, and R. Juanes. Basin-scale CO₂ storage capacity estimates from fluid dynamics. In J. Carrera, editor, *XVIII International Conference on Water Resources, CMWR 2010*, Barcelona, 2010a. CIMNE.
- M. L. Szulczewski, C. W. MacMinn, and R. Juanes. How pressure buildup and CO₂ migration can both constrain storage capacity in deep saline aquifers. In *10th Intl. Conf. Greenhouse Gas Control Technol., GHGT-10*, Amsterdam, The Netherlands, September 19–23, 2010b.
- T. Tokunaga, S. Hosoya, H. Tosaka, and K. Kojima. An estimation of the intrinsic permeability of argillaceous rocks and the effects of long-term fluid migration. In S. J. Düppenbecker and J. E. Iliffe, editors, *Basin Modelling: Practice and Progress*, volume 141, pages 83–94. Geological Society of London, 1998.
- H. Trapp, Jr. and M. A. Horn. The ground water atlas of the United States: Delaware, Maryland, New Jersey, North Carolina, Pennsylvania, Virginia, West Virginia. Hydrologic Atlas 730-L, U.S.G.S., 1997.

- L. G. H. van der Meer and P. J. P. Egberts. A general method for calculating subsurface CO₂ storage capacity. In *Offshore Technology Conference*, Houston, TX, May 5–8, 2008. (OTC 19309).
- H. F. Wang. *Theory of Linear Poroelasticity*. Princeton University Press, 2000.
- R. L. Whitehead. The ground water atlas of the United States: Montana, North Dakota, South Dakota, Wyoming. Hydrologic Atlas 730-I, U.S.G.S., 1996.
- L.H. Wickstrom, E. R. Venteris, J. A. Harper, J. McDonald, E. R. Slucher, K. M. Carter, S. F. Greb, J. G. Wells, W. B. Harrison III B. C. Nuttall, R. A. Riley, J. A. Drahovzal, J. A. Rupp, K. L. Avary, S. Lanham, D. A. Barnes, N. Gupta, M. A. Baranoski, P. Radhakrishnan, M. P. Solis, G. R. Baum, D. Powers, M. E. Hohn, M. P. Parris, K. McCoy, G. M. Grammer, S. Pool, C. Luckhardt, and P Kish. Characterization of geologic sequestration opportunities in the MRCSP Region: final report under DOE cooperative agreement DE-PS26-05NT42255, 2005.
- H. B. Willman, E. Atherton, T. C. Buschbach, C. Collinson, J. C. Frye, M. E. Hopkins, J. A. Lineback, and J. A. Simon. *Handbook of Illinois stratigraphy*. Number Bulletin 95. Illinois State Geological Survey, 1975.
- Y. C. Yortsos. A theoretical analysis of vertical flow equilibrium. *Transp. Porous Media*, 18: 107–129, 1995.
- H. L. Young and D. I. Siegel. Hydrogeology of the Cambrian-Ordovician aquifer system in the northern Midwest, United States, with a section on ground-water quality. Professional Paper 1405-B, U.S.G.S., 1992.
- Q. Zhou, J. T. Birkholzer, C. Tsang, and J. Rutqvist. A method for quick assessment of CO₂ storage capacity in closed and semi-closed saline formations. *Int. J. Greenh. Gas Con.*, 2: 626–639, 2008a.
- Q. Zhou, J. T. Birkholzer, C. Tsang, and J. Rutqvist. A method for quick assessment of CO₂ storage capacity in closed and semi-closed saline formations. *Int. J. Greenh. Gas Control*, 2:626–639, 2008b.
- M. D. Zoback. *Reservoir Geomechanics*. Cambridge University Press, 2007.
- M. L. Zoback and M. Zoback. State of stress in the conterminous United States. *J. Geophys. Res.*, 85(B11):6113–6156, 1980a.
- M. L. Zoback and M. Zoback. State of stress in the conterminous United States. *J. Geophys. Res.*, 85(B11):6113–6156, 1980b.

MILESTONE STATUS REPORT

Task/ Subtask/Description	Year 1				Year 2				Year 3				Planned Start date	Planned End date	Actual Start date	Actual End date	Comments (notes, explanation of deviation from plan)
	Q1	Q2	Q3	Q4	Q1	Q2	Q3	Q4	Q1	Q2	Q3	Q4					
	1-Jan-10	1-Apr-10	1-Jul-10	1-Oct-10	1-Jan-11	1-Apr-11	1-Jul-11	1-Oct-11	1-Jan-12	1-Apr-12	1-Jul-12	1-Oct-12					
1.0 Revise PMP	X												1-Jan-10	31-Mar-10	1-Jan-10	17-Jan-10	17-Jan-10 Revised PMP sent by email on Jan 17, 2010
1.0 Kick-off meeting	X												1-Jan-10	31-Mar-10	1-Jan-10	16-Mar-10	Virtual meeting via WebEx
2.0 Technol. Status Assessment	X												1-Jan-10	31-Mar-10	1-Jan-10	31-Mar-10	
7.0 Educational program instituted		X											1-Jan-10	30-Jun-10	1-Jan-10	30-Jun-10	MIT course 1.723: Computational methods ...
7.0 CCS Short course			X										1-Apr-10	30-Sep-10	1-Apr-10	28-Jul-10	CCS short course delivered, July 26-28, 2010
3.1/3.2 Pressure and capil. Trapping				X									1-Jan-10	31-Dec-10	1-Jan-10	31-Dec-10	Described in progress reports and JFM papers
3.3/3.4 Dissolution and leakage													1-Jul-10	31-Dec-11	1-Apr-10	31-Dec-11	Described in progress reports and PNAS papers
3.3/3.4 Storage capacity tool													1-Jan-11	31-Dec-11	1-Jan-11	31-Dec-11	Described in progress reports and PNAS paper deemed not necessary -- not on the critical path
3.3/3.4 Visualization in Google Earth													1-Jan-11	31-Dec-11	1-Jan-11	31-Dec-11	Described in progress reports and PNAS paper
4.1 Geologic data													1-Jul-11	31-Dec-11	1-Jul-11	30-Jun-12	Described in progress reports and PNAS paper
4.1 Application of migration models													1-Jul-11	30-Jun-12	1-Jul-11	30-Jun-12	Described in progress reports and PNAS paper
4.2 Application of leakage models													1-Jan-12	31-Dec-12	1-Jan-12	30-Jun-13	Described in progress report
5.1/5.2 Capacity and injectivity estimates													1-Jul-11	31-Dec-12	1-Jul-11	31-Dec-12	Described in progress reports and PNAS paper
6.0 Risk assessment methodologies													1-Jan-11	31-Dec-12	1-Jan-11	31-Dec-12	Described in progress report
All Final project report													1-Oct-12	31-Dec-12	1-Jul-13	1-Jul-13	This document

National Energy Technology Laboratory

626 Cochrans Mill Road
P.O. Box 10940
Pittsburgh, PA 15236-0940

3610 Collins Ferry Road
P.O. Box 880
Morgantown, WV 26507-0880

One West Third Street, Suite 1400
Tulsa, OK 74103-3519

1450 Queen Avenue SW
Albany, OR 97321-2198

2175 University Ave. South
Suite 201
Fairbanks, AK 99709

Visit the NETL website at:
www.netl.doe.gov

Customer Service:
1-800-553-7681

